

Determine the impact on the workability affected by dynamic interaction of an Ampelmann system connected to a CALM buoy

M. van Beurden



Determine the impact on the workability affected by dynamic interaction of an Ampelmann system connected to a CALM buoy

By

M. van Beurden

4023188

To obtain the degree of Master of Science in Offshore and Dredging Engineering
At the Delft University of Technology
to be defended publicly on Tuesday June 11th 2019 at 15:30

Supervisor:	Prof. dr. ir. K.A. Riska	TU Delft
Thesis committee:	Dr. ir. A. Jarquin Laguna	TU Delft
	Dr. F. Pisanó	TU Delft
	Ir. R. D. Schipperen	Ampelmann Operations



Abstract

Ampelmann provides a service transferring people and cargo from a host vessel to offshore structures. Due to the increase in the diversity of offshore structures, a study is started to investigate how Ampelmann can join the market of working with floating structures. An Ampelmann system compensates vessel motions of the host vessel and connects via a gangway to a target structure, which currently are fixed structures or a barely moving, large vessels. The gangway is exerting a constant force on the target structure to stay connected. Connecting to relatively small floating bodies, using this operational method, creates a dynamic interaction between the forces exerted by the gangway and the response of the floating body. To study whether this dynamic interaction should be implemented in the workability analyses of Ampelmann, the workability including and excluding the dynamic interaction is studied and the result is compared.

Potential new projects for Ampelmann are transferring maintenance personal onto CALM buoys. CALM buoys are on- and offloading buoys for tankers to mainly transport crude oil to an onshore facility. The current method of calculating the workability, which shows how well an Ampelmann system can operate for a certain project, is based on a kinematic approach. In a numerical, time-domain model (aNySIM), the dynamic interaction of the gangway forces and the response of the CALM buoy is implemented.

Full-scale Ampelmann tests show that the gangway forces can be modeled as damping forces in the 3 degrees of freedom of the gangway. A sensitivity study shows that the ratio between the hydrodynamic damping of the buoy and the gangway damping is governing in the effect of the gangway forces affecting the response of the buoy. According to diffraction calculations of the buoy, the hydrodynamical damping can vary significantly in the frequency spectrum. For low- and high-frequency waves the hydrodynamical damping of the buoy is significantly lower than in the mid-frequency spectrum.

The numerical model in aNySIM and a python model, based on the analytical approach, are used to study the result of the dynamic interaction using low-frequency wave conditions for in-plane motion. Both models show that for low-frequency wave conditions the gangway forces decreases the amplitude of the response of the buoy up to 10%.

To reach the goal of this thesis the numerical model in aNySIM is extended to 3d, implementing all degrees of freedom for the buoy and the gangway. Using this model, a workability study is performed to study the effect of the dynamic interaction. For every sea state the response of the buoy is simulated, monitoring the operational limits of the Ampelmann system. Comparing the workability results of a model including the dynamic interaction and of a model based on a kinematic approach, show an improvement in workability of 1% due to the gangway damping forces.

Preface

Before you lies the master thesis dedicated to the Master of Science of Mike van Beurden. It has been written to complete the graduation requirements of the master specialization Bottom Founded Structures, Arctic and Wind at the department Offshore and Dredging Engineering at the University of Technology of Delft, during the period of July 2018 until June 2019.

The research topic has been chosen in collaboration with Ampelmann Operations. I would like to thank Ampelmann for giving me the opportunity to use their experience and expertise to conduct this research.

I would like to thank my supervisors, Kaj Riska and Antonio Jarquin Laguna from the TU Delft, and Remco Schipperen from Ampelmann, for their guidance and critical feedback during my thesis to keep me on track and to focus on the final goal.

Last but definitely not least, I would like to thank my friends, family and colleagues for helping me to put all the challenges into perspective and for helping me to relax during this time when needed. A special thanks goes to Fleur for supporting me unconditionally.

Table of Contents

1.	Introduction	1
1.1	Background	1
1.2	Problem description.....	2
1.3	Constraints	3
1.4	Method	4
1.5	Reading guide.....	5
2.	Ampelmann system and CALM buoy	7
2.1	Ampelmann system	7
2.1.1	Hexapod	7
2.1.2	Gangway and transferdeck	8
2.2	CALM buoy	9
2.2.1	Catenary mooring	10
2.3	Host vessel	11
2.4	Location.....	11
3.	Hydrodynamic model.....	13
3.1	Introduction	13
3.2	EOM	13
3.3	Potential theory	14
3.4	Panel distribution.....	16
3.5	Configuration vessel and buoy.....	17
3.6	Added damping.....	18
3.7	Mooring stiffness	19
3.8	Results.....	20
3.8.1	Mooring lines	20
3.8.2	Added mooring stiffness	21
3.8.3	Diffraction	22
4.	Numerical dynamic model	23
4.1	Introduction	23
4.2	aNySIM.....	23
4.2.1	Structure model	23
4.3	Buoy	24
4.4	Mooring lines	25
4.4.1	Verification mooring lines.....	26
4.4.2	Effect simplifications modeled buoy.....	28

4.5	Ampelmann system	29
4.5.1	Implementing external forces.....	29
4.5.2	In-plane model constraints	30
4.5.3	Telescoping force	31
4.5.4	Luffing force	33
5.	Analytical approach.....	35
5.1	Introduction	35
5.2	Mass-spring-damper system.....	35
5.3	Equations of motion.....	36
5.4	Small angle approximation	37
5.4.1	Global velocity.....	37
5.4.2	Luffing velocity	38
5.4.3	Telescoping velocity	40
5.5	Telescoping damping matrix.....	42
5.6	Luffing damping matrix.....	45
5.7	Sensitivity study telescoping force	47
5.7.1	Luffing angle.....	48
5.7.2	Telescoping damping coefficient	49
5.7.3	Hydrodynamic damping coefficient.....	50
5.8	Sensitivity study luffing force.....	51
5.8.1	Luffing angle.....	51
5.8.2	Luffing damping coefficient	51
5.8.3	Hydrodynamic damping coefficient.....	52
5.8.4	Gangway length	53
5.9	Solving equations of motion	54
5.9.1	Case study	54
5.9.2	ODE solver.....	55
5.9.3	Comparing aNySIM and Python model.....	56
5.10	Dynamic vs kinematic approach	60
5.11	Conclusion.....	62
6.	Workability study.....	63
6.1	Introduction	63
6.2	3D configuration	63
6.2.1	Global velocities	64
6.2.2	Telescoping force	65
6.2.3	Luffing force	65

6.2.4	Slewing force.....	65
6.2.5	Global gangway forces.....	66
6.3	Operational limits.....	67
6.4	Sea states.....	68
6.5	Workability approach and results.....	69
6.6	Workability per operational limit.....	72
6.7	Conclusion.....	73
7.	Conclusion and recommendations.....	75
7.1	Conclusion.....	75
7.2	Recommendations.....	77
8.	Bibliography.....	79
9.	Appendices.....	81
9.1	Buoy configuration.....	81
9.2	AMOG Data.....	83
9.3	Diffraction results.....	86
9.4	Offset tests aNySIM.....	87
9.5	Roll response case study.....	88
9.6	EOM analyses.....	89
9.7	ODE Solver.....	91
9.8	Workability study.....	95

List of figures

Figure 1-1 Basket transfer.....	1
Figure 1-2 An Ampelmann system connected to a fixed offshore platform.	1
Figure 1-3 Visual representation of a connected Ampelmann system to a CALM buoy.....	2
Figure 1-4 Configuration coupled system.....	3
Figure 1-5 Schematic overview approach.....	4
Figure 2-1 A-type Ampelmann system.....	7
Figure 2-2 Degrees of freedom for the gangway including transferdeck.	8
Figure 2-3 Connected CALM buoy configuration.....	9
Figure 2-4 SOFEC CALM buoy.	10
Figure 2-5 Top view mooring configuration.	10
Figure 2-6 Svitzer Vision.....	11
Figure 2-7 Global location of CALM buoy.	11
Figure 2-8 Zoomed location of CALM buoy.	11
Figure 3-1 Panel size convergence study.	17
Figure 3-2 Configuration host vessel and buoy.	17
Figure 3-3 Horizontal restoring force vs offset.	19
Figure 3-4 Surge RAO moored and unmoored buoy	20
Figure 3-5 Pitch RAO moored and unmoored buoy.....	20
Figure 3-6 Heave RAO comparing stiffness matrix.	21
Figure 3-7 Pitch RAO comparing stiffness matrix.	21
Figure 3-8 Heave RAO with and without diffraction.....	22
Figure 3-9 Roll RAO with and without diffraction.....	22
Figure 4-1 Overview structure aNySIM model.....	24
Figure 4-2 Step force in x-direction	26
Figure 4-3 Offset buoy in x-direction	26
Figure 4-4 CALM buoy with skirt.....	28
Figure 4-5 Schematic overview of implementing forces.	29
Figure 4-6 Schematic overview boundaries model.....	30
Figure 4-7 Schematic representation telescoping gangway.....	31
Figure 4-8 Projection telescoping force.	32
Figure 4-9 Schematic overview luffing force.	33
Figure 4-10 Projection luffing force.	33
Figure 5-1 Schematic representation of a CALM buoy in the y-z-plane.	35
Figure 5-2 Projected velocities caused by roll.	37
Figure 5-3 Luffing velocity caused by roll motion.....	38
Figure 5-4 Luffing velocity factor (alpha=0.12 rad).....	39
Figure 5-5 Luffing velocity factor (alpha=0.27 rad).....	39
Figure 5-6 Telescoping velocity caused by roll motion.....	40
Figure 5-7 Telescoping velocity factor (alpha = 0.12 rad).....	41
Figure 5-8 Telescoping velocity factor (alpha = 0.27 rad).....	41
Figure 5-9 Schematic representation of fixed luffing angle (alpha = 0 rad and $\pi/2$ rad).	43
Figure 5-10 Damping force varying luffing angle.....	48
Figure 5-11 Damping moment varying luffing angle.	48
Figure 5-12 Damping force varying telescoping damping coefficient.	49
Figure 5-13 Damping force varying telescoping damping coefficient.	49

Figure 5-14 Damping force with varying hydrodynamic damping in sway.....	50
Figure 5-15 Damping force with varying hydrodynamic damping in heave.	50
Figure 5-16 Damping moment with varying hydrodynamic damping in roll.....	50
Figure 5-17 Damping force varying luffing angle.....	51
Figure 5-18 Damping moment varying luffing angle.	51
Figure 5-19 Damping forces luffing damping coefficient.....	51
Figure 5-20 Damping moment luffing damping coefficient.....	51
Figure 5-21 Damping force varying hydrodynamic damping coefficient for sway.	52
Figure 5-22 Damping force varying hydrodynamic damping coefficient for heave.	52
Figure 5-23 Damping moment varying hydrodynamic damping coefficient for roll.	52
Figure 5-24 Damping force varying gangway length.	53
Figure 5-25 Damping moment varying gangway length.	53
Figure 5-26 Frequency dependent damping coefficients for sway, heave and roll.	54
Figure 5-27 Mooring configuration at maximum sway position of the buoy.....	56
Figure 5-28 Total mooring forces acting on the buoy.....	57
Figure 5-29 Spectrum Analyses Incoming waves.....	57
Figure 5-30 Sway response without gangway included by aNySIM and Python.	58
Figure 5-31 Undamped sway response by aNySIM and Python.	59
Figure 5-32 Sway response computed by aNySIM.	60
Figure 5-33 Sway response computed by Python.....	60
Figure 5-34 Heave response computed by aNySIM.....	61
Figure 5-35 Heave response computed by Python.....	61
Figure 6-1 Schematic representation of positioning host vessel.....	63
Figure 6-2 Slewing force.....	65
Figure 6-3 3D representation gangway forces.....	66
Figure 9-1 Buoy configuration.	81
Figure 9-2 Mooring configuration.....	82
Figure 9-3 Restoring force in direction mooring line 1.	83
Figure 9-4 Restoring force in direction mooring line 2.	83
Figure 9-5 Restoring force in direction mooring line 3.	84
Figure 9-6 Restoring force in direction mooring line 4.	84
Figure 9-7 Restoring force in direction mooring line 5.	85
Figure 9-8 Restoring force in direction mooring line 6.	85
Figure 9-9 Decay test heave (+1m).	87
Figure 9-10 Decay test roll (+0.15rad).	87
Figure 9-11 Roll response case study without dynamic interaction.	88
Figure 9-12 Roll response case study without dynamic interaction.....	88
Figure 9-13 FBD telescoping force with Y-displacement.	89
Figure 9-14 FBD telescoping force with Z-displacement.	89
Figure 9-15 FBD telescoping moment with Roll-displacement.....	89
Figure 9-16 FBD luffing force with Y-displacement.	90
Figure 9-17 FBD luffing force with Z-displacement.	90
Figure 9-18 FBD luffing moment with Roll-displacement.....	90

List of Tables

Table 2-1 Properties CALM buoy.	10
Table 2-2 Mooring lines properties.....	10
Table 2-3 Properties of the Svitzer vision and the host vessel used.....	11
Table 4-1 Parameters buoy in aNySIM.	24
Table 4-2 Parameters mooring lines in aNySIM.....	25
Table 4-3 Results of static offset tests.	26
Table 4-4 Comparison pretension and vertical force mooring line.	27
Table 5-1 Minimum and maximum angles case study.....	39
Table 5-2. Parameters case study.	47
Table 6-1 Operational limits gangway.	67
Table 6-2 Wave scatter diagram Papua New Guinea (01-03-1997 – 28-02-2007).....	68
Table 6-3 Operability results with dynamic interaction.	69
Table 6-4 Operability results by kinematic approach.	70
Table 6-5 Workability result with dynamic interaction.	71
Table 6-6 Workability result with kinematic approach.....	72
Table 6-7 Workability study per operational limit.....	72
Table 9-1 Diffrac data (at $\omega = 0.4$ rad/s, incoming angle = 90 deg).....	86
Table 9-2 Numbering sea states.	95
Table 9-3 Results operability per parameter with dynamic interaction.....	95
Table 9-4 Results operability per parameter without dynamic interaction.	97

Nomenclature

A	Added mass matrix
A_{wl}	Wetted area waterline
C	Damping matrix
C_{eq}	Equivalent damping matrix
c_{tel}	Telescoping damping coefficient
c_{luf}	Luffing damping coefficient
F_d	Diffraction force
F_{fk}	Froude-Krylov force
$F_{gangway}$	Gangway forces
$F_{mooring}$	Mooring line forces
F_r	Radiation force
F_s	Hydrostatic force
F_w	Wave exciting forces
g	Gravitational acceleration
G	Green's function
GM	Metacentric height
H_s	Significant wave height
h_0	Distance from the origin of the earth-fixed coordinate system to the seabed
K	Stiffness matrix
K_{eq}	Equivalent stiffness matrix
k	Wave number
k_{luf}	Luffing velocity factor
k_{tel}	Telescoping velocity factor
L	Gangway length
M	Mass matrix
M_{eq}	Equivalent mass matrix
n	Normal vector
p	First-order pressure
R_x	Elementary rotation matrix roll
R_y	Elementary rotation matrix pitch
R_z	Elementary rotation matrix yaw
S_0	Wetted surface body
T_z	Zero crossing period
v	Fluid velocity
v_b	Velocity in body-fixed coordinate system
v_g	Velocity in global coordinate system
v_{luf}	Luffing velocity
v_{tel}	Telescoping velocity
x	Surge coordinate
y	Sway coordinate
z	Heave coordinate
x_{tip}	Surge coordinate connection point tip gangway
y_{tip}	Sway coordinate connection point tip gangway
z_{tip}	Heave coordinate connection point tip gangway
x_{td}	Surge coordinate transferdeck
y_{td}	Sway coordinate transferdeck
z_{td}	Heave coordinate transferdeck
α	Luffing angle

β	Slewing angle
∇	Displacement
ζ_a	Wave amplitude
ζ_0	Amplitude of the undisturbed wave
θ	Roll angle
λ	Wave length
μ	Wave direction measured from x-direction
ρ	Water density
ϕ	Pitch angle
ϕ_d	Potential due to diffraction
ϕ_j	Potential due to 6DOF motions
ϕ_w	Potential due to undisturbed incoming wave force
ϕ_y	Phase angle wave force in sway
ϕ_z	Phase angle wave force in heave
ϕ_θ	Phase angle wave moment in roll
ψ	Yaw angle
σ_j	Complex source strength
ω	Wave frequency

1. Introduction

1.1 Background

Ampelmann is a Dutch, Delft-based offshore company, which provides services in safe people and cargo offshore transfer. The head office is located in Delft and to reach the international offshore market Ampelmann has 13 offices across the globe. Its vision is to make offshore access as easy as crossing the street. Before motion-compensated people transfer, people transfer was mainly done by “basket transfer”, in which a crane lifts a basket of people from a vessel to an offshore platform (Figure 1-1)



Figure 1-1 Basket transfer.

There are significant risks attached to this method of people transfer and the operability is highly dependent on the weather conditions. To make people and cargo transfer safer and more efficient, Ampelmann found a new method to do this by compensating vessel motions and form a bridge between the vessel and platform.

By continuously monitoring the motions of the vessel, these motions can be compensated with respect to the fixed world. This compensation is done by a Stewart platform, which is an important component of the Ampelmann system. With six hydraulic cylinders the vessel motions are compensated continuously, creating a deck that is not or barely moving with respect to the fixed world. From this deck a gangway is connected to the target platform that forms a bridge between the host vessel and the target structure. With this technique Ampelmann provides safe and efficient people and cargo transfer to make it possible to keep on working in a safe manner up to 3m significant wave height (Ampelmann, 2019).

The offshore market is changing, 10-20 years ago the offshore market was mainly focused on oil and gas but now the market for renewables, maintenance and decommissioning is growing. Due to this change, the walk-to-work vision of Ampelmann extends their current market. Not only should oil and gas platforms be easily accessible, but other structures come to mind, such as wind turbines, (small) floating vessels, CALM buoys, etc.



Figure 1-2 An Ampelmann system connected to a fixed offshore platform.

When the Ampelmann system is connected to a fixed offshore structure (Figure 1-2), the gangway exerts a constant force to the structure. For a fixed structure this force is not any significance, but for floating bodies it might be. The station keeping mechanisms for these floating structures may not be designed for high external

forces. This makes it an interesting research topic for Ampelmann to look into the influence of an Ampelmann system on floating bodies.

1.2 Problem description

Currently the biggest markets for Ampelmann are oil and gas platforms, wind turbines or very large vessels like FPSO's. When an Ampelmann system connects to these large fixed or floating structures, the gangway applies a constant force to maintain the connection between the vessel and the target structure. Ampelmann likes to expand its market share. Vessel-to-vessel transfer is considered as a promising market for Ampelmann, where people or cargo will be transferred to relatively small floating structures. This will introduce a dynamic aspect into the combined system of a coupled Ampelmann system and a floating vessel. Large vessels or fixed platforms will slowly or not move with respect to the connected gangway resulting in very little motion at the end of the gangway. When the gangway is connected to a smaller vessel, the motions of the target vessel will cause the gangway to move. This will lead to internal forces of the gangway, which will act on the target structure, which has not been accounted for in research by Ampelmann so far.

A workability study of the Ampelmann system tells a customer how well the Ampelmann system performs for a certain operation. This tells the customer how much the operational time of the operation improves by including an Ampelmann system in a project. With the current approach of calculating the workability, it is assumed that the force that is applied by the gangway on the target structure does not influence the motions of the target structure. For fixed platforms and large floating structures this assumption is easily explained by the size of the target structures compared to the Ampelmann system and host vessel.

With vessel-to-vessel connection, the size of the target vessel is considerably smaller and the motions of the target vessel might be influenced by the forces caused by the Ampelmann system. The dynamic interaction of a floating body and the Ampelmann system may influence the workability of the coupled system, which will be studied in this thesis.



Figure 1-3 Visual representation of a connected Ampelmann system to a CALM buoy.

The central case in this thesis is based on an innovative project of Ampelmann Operations where an Ampelmann system will be connected to a Catenary Anchored Leg Moored buoy (CALM buoy) that is used for on- and offloading oil tankers offshore (Figure 1-3). This case and the new coupling mechanism of a target vessel and a connected gangway serves as the foundation of the research objective.

'Determine the impact on the workability affected by dynamic interaction of an Ampelmann system connected to a CALM buoy'

1.3 Constraints

The operational configuration consists of 3 bodies; (1) the host vessel, (2) an A-type Ampelmann system and (3) the CALM buoy, which can be seen in Figure 1-4. The Ampelmann system is dynamically coupled with the host vessel and the CALM buoy. The dynamic interaction between the host vessel and Ampelmann system has been studied by Wiegerink (Wiegerink, Modelling of Coupled Vessel-Ampelmann systems for Workability Studies, 2015), so this will not be the focus of this thesis. The primary focus of this thesis is the dynamic interaction between the Ampelmann system and the CALM buoy.

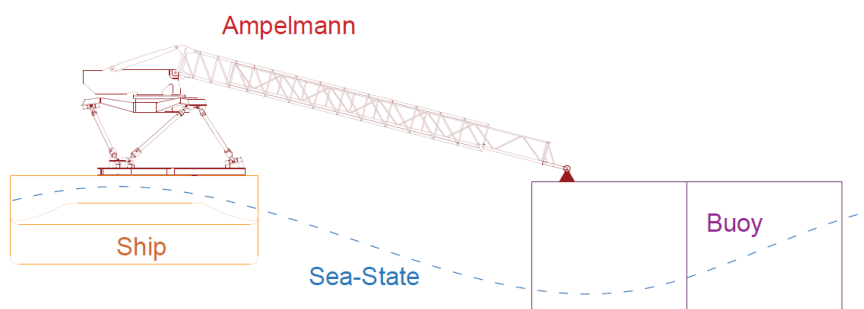


Figure 1-4 Configuration coupled system.

To be able to focus on the interaction between the Ampelmann system and the CALM buoy, constraints will apply to the configuration of the 3 bodies. The host vessel is being kept in place by a dynamic positioning (DP) system and it is assumed that the DP system is working perfectly. Furthermore the assumption is made that the residual motions of the host vessel are fully compensated by the hexapod of the Ampelmann system. Moreover, external effects such as wind and current are not included in the scope of this study and only waves are implemented in the environmental conditions of the model.

To connect the Ampelmann system to a CALM buoy requires a new connection method (Sreedharan, 2016). The Ampelmann system will be connected to the buoy using a magnet, which can freely rotate. It is assumed that the magnet will never disconnect.

To study the coupling effects of the Ampelmann system and the CALM buoy, the numerical model is linearized as much as possible. The main linearization is the linearization of the mooring lines within a certain working range.

1.4 Method

To reach the goal of this study, the thesis is divided into sub-objectives. The main objective is to study the coupling effect between an Ampelmann system and a CALM buoy. The first sub-objective is to create a hydrodynamic model of the CALM buoy. The frequency dependent hydrodynamic properties of the CALM buoy are calculated in a diffraction software called Diffrac. These hydrodynamic properties are used in a hydrodynamic, numeric, time-domain simulation software (aNySIM) to simulate the response of the CALM buoy to certain wave conditions. The numerical model of the CALM buoy consists of two parts; the floating buoy and the mooring lines. The properties of these components are based on the CALM buoy from a current Ampelmann project in Papua New Guinea.

aNySIM provides tools to easily change the environmental conditions and insert simple external forces but to implement the more complex coupling mechanism between the Ampelmann system and the CALM buoy an external script is used to implement the coupling mechanism. Simulations of the numerical model results in time-series of the response of the buoy and the gangway. These responses are analyzed in a workability study which compares the workability study including and excluding the dynamic interaction. The schematic overview of the method of this thesis is shown in Figure 1-5.

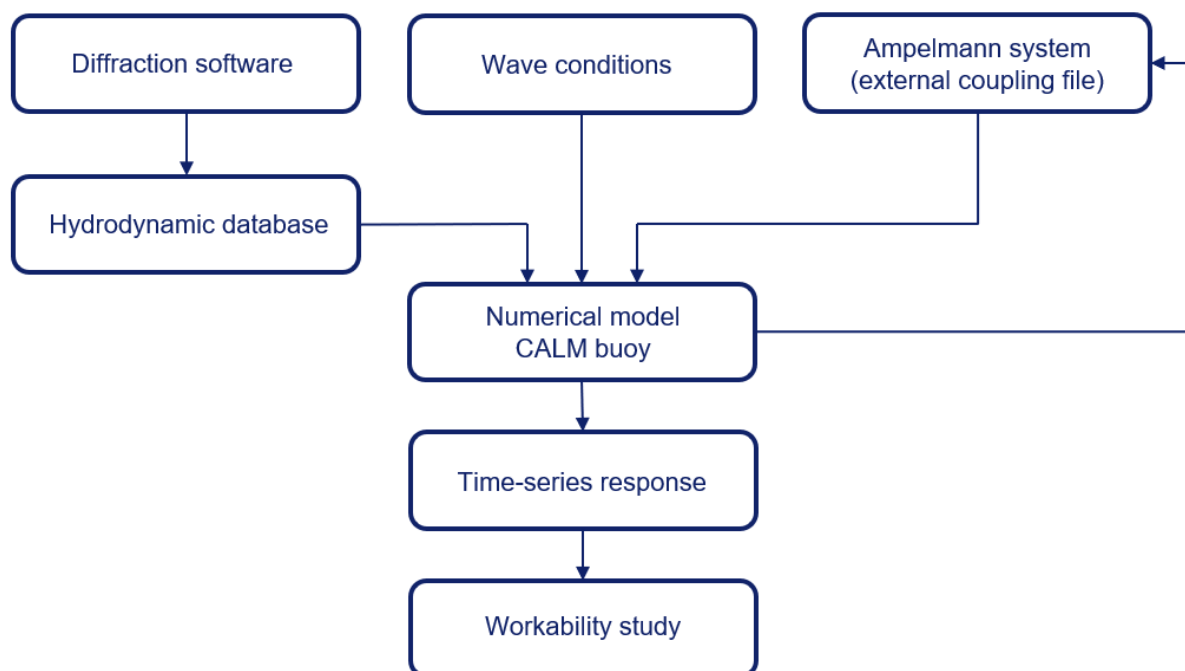


Figure 1-5 Schematic overview approach.

The coupling effect of the Ampelmann system and CALM buoy will at first be studied in plane-motion to study the effect of the important parameters of the coupled system. The Ampelmann forces are implemented in the numerical model and the effect on the response of the buoy will be studied. An analytical approach for the in-plane motion is used to set up the equations of motion of the buoy including the external Ampelmann forces. From this approach the parameters of the damping forces are found and the effect of the parameters is studied.

To perform a workability study all the degrees of freedom of the buoy and gangway are implemented. This results in a fully 3 dimensional model. The operational limits of the gangway are used to set up the criteria for the workability study. With the known wave scatter diagram as wave input, the time-series for each sea state are computed by the numerical model, which is used for the workability study. The results of the workability study are used to determine whether the dynamic interaction of the Ampelmann system and a CALM buoy affects the workability and if it should be included for further projects.

1.5 Reading guide

In chapter 2 more detailed information about the components of the coupled system is given. Chapter 3 elaborates how the hydrodynamic properties of the moored buoy are calculated and why this is done. In chapter 4 the hydrodynamic properties of the CALM buoy are used, creating a numerical time-domain model and the structure of the model is explained, including the external script, which is written to study the coupling mechanism for in-plane motion. An analytical approach is used in chapter 5 to study the coupling of the gangway forces and the in-plane motion of the CALM buoy. This study shows the effect of the buoy and gangway parameters which can vary the effect on the dynamic coupling. In chapter 6 the workability study is performed with time-series from the numerical model. To perform a realistic workability study the model is extended to a 3d model. With these results the thesis is concluded in chapter 7 including recommendations for Ampelmann and further studies.

2. Ampelmann system and CALM buoy

2.1 Ampelmann system

The idea of the Ampelmann system was founded during an offshore wind conference in Berlin. Would it be possible to compensate vessel motions with an upside-down flight simulator? This idea has been worked out and was found to be a success. This resulted in the Ampelmann system containing 6 hydraulic cylinders that can compensate vessel motions in 6 degrees of freedom (J. van der Tempel, 2007). This makes it possible to connect a gangway to a platform that is not or barely moving with respect to the target structure. The Ampelmann system consists of 2 major components; the hexapod and the gangway. All major components of an A-type Ampelmann system, that is used in this thesis, are shown in Figure 2-1.

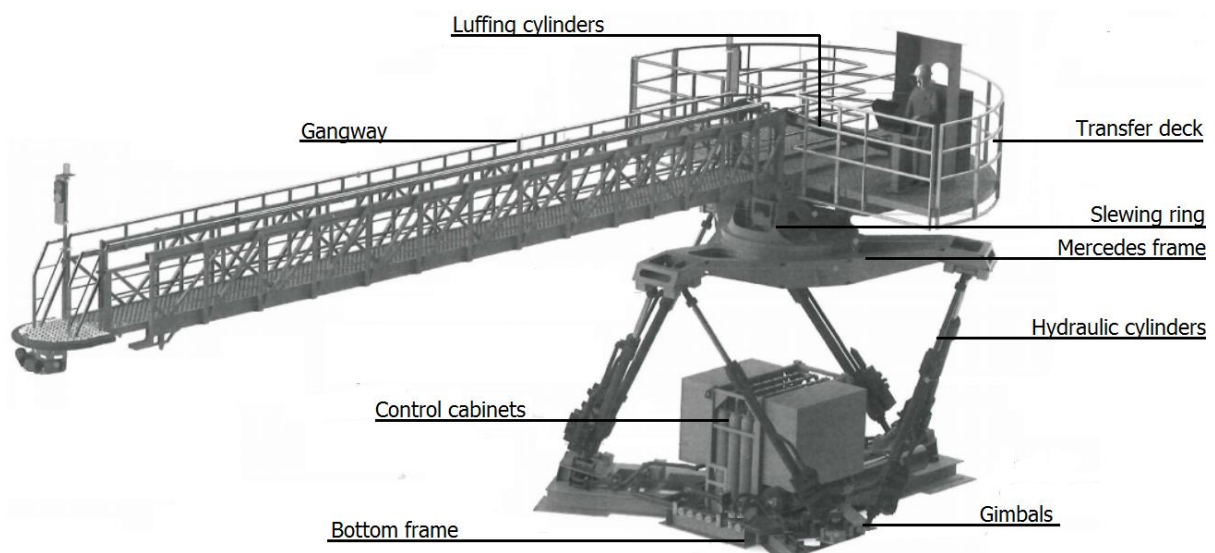


Figure 2-1 A-type Ampelmann system.

2.1.1 Hexapod

The technique of compensating the vessel motion is based on a flight simulator that has been turned upside-down. Instead of creating motions to simulating airplane motions, the motions are being compensated. This is done by a Stewart platform including 6 hydraulic cylinders which makes it possible to compensate in 6 degrees of freedom. The OCTANS motion sensor in the Ampelmann system measures the motions in 6 degrees of freedom and this information is converted into cylinder motions to counter the measured vessel motions at the location of the gangway. The 6 cylinders are connector via gimbals to the bottom frame at the bottom of the hexapod, and to the Mercedes frame on the topside of the hexapod.

2.1.2 Gangway and transferdeck

The gangway including the transferdeck makes it possible to transfer people from the host vessel to the target structure. The transferdeck is the access point for people to access the gangway. Prior to operation, people walk on the transferdeck via the gangway which is located on deck of the vessel. When the people are located on the transferdeck the hexapod engage and the gangway will connect to the target structure. The gangway and transferdeck have 3 degrees of freedom; slewing, luffing and telescoping, which are shown in Figure 2-2.

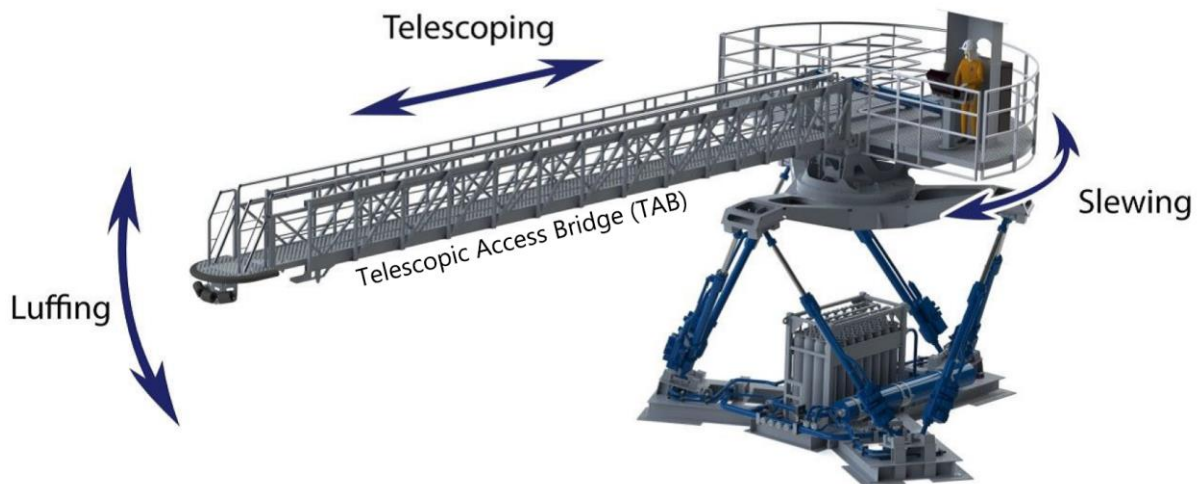


Figure 2-2 Degrees of freedom for the gangway including transferdeck.

The slewing ring between the transferdeck and the Mercedes frame makes it possible to rotate the gangway and transferdeck. The luffing cylinders at the transferdeck are connected to the gangway which creates a luffing motion of the gangway. Extending and retracting the gangway is called telescoping. This is done by a telescoping cable inside the gangway, which is driven by hydraulic pumps.

2.2 CALM buoy

A CALM buoy is a widely used on- and offloading terminal which often is located relatively close to shore. They have been deployed in varying locations, water depths and environmental conditions. A CALM buoy system consists of a floating buoy that is moored to the seabed via catenary anchored mooring lines. A turntable is mounted on top of the buoy, which weathervanes in the orientation of the least resistance, making it possible for the on- or offloading vessel (tanker) to orientate in an optimal manner. Floating connection hoses makes it possible for the tankers to connect to the CALM buoy and start the on- or offloading process. The CALM buoy is connected via subsea hoses to a Pipeline End Termination (PLET) which is the end of the subsea pipeline to transport the fluids to the onshore storage facility. The complete configuration of a connected CALM buoy to a tanker is shown in Figure 2-3.

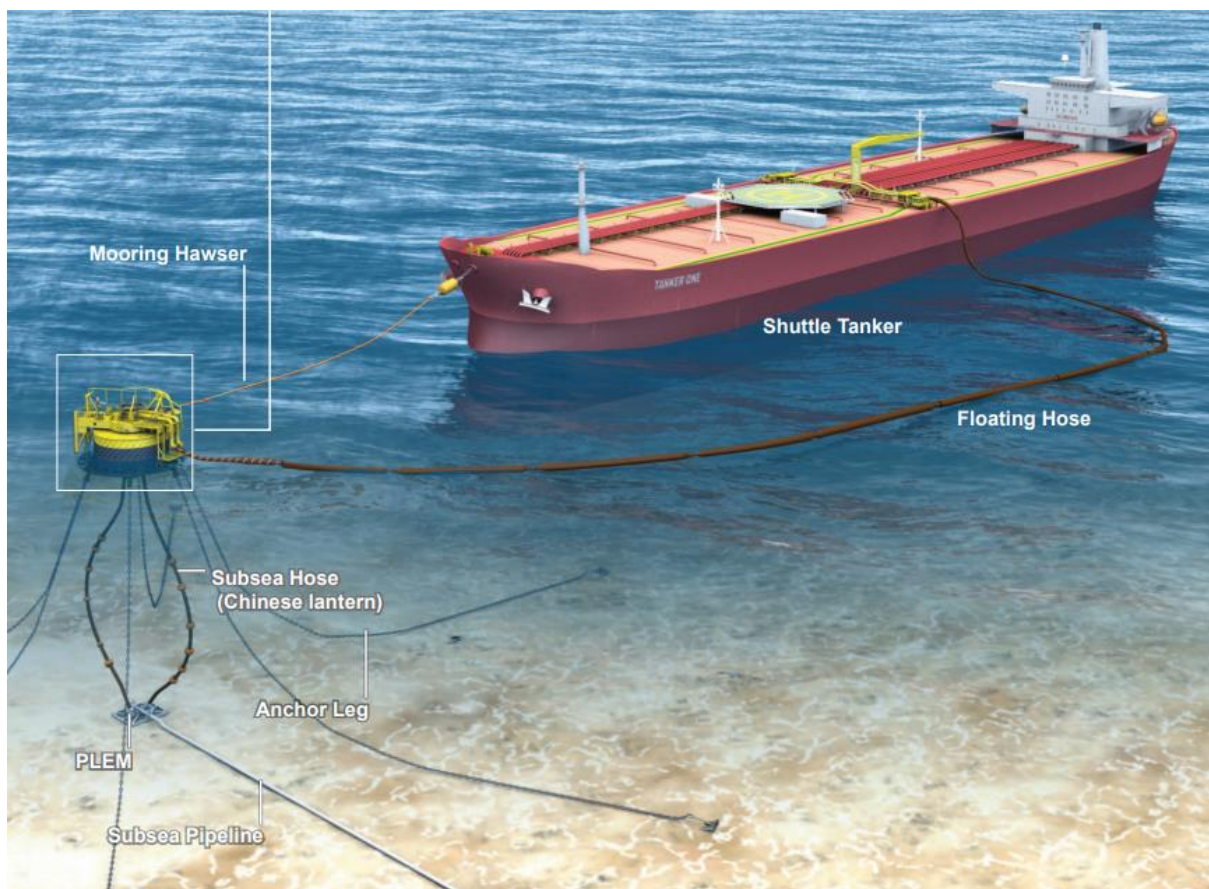


Figure 2-3 Connected CALM buoy configuration.

The CALM buoy used in this thesis is the PNG–Kumul Marine CALM for Oil Search Limited. The most important properties of this buoy are given in Table 2-1 (sofec, 2018).

Table 2-1 Properties CALM buoy.

Property	Value
Diameter [m]	12,5
Draft (operational) [m]	3,08
Freeboard [m]	2,22
COG w.r.t. keel [m, m, m]	[6,25 0 2,65]
Mass [tonnes]	281,6
Radii of gyration, roll [m]	4
Radii of gyration, pitch [m]	4
Radii of gyration, yaw [m]	5



Figure 2-4 SOFEC CALM buoy.

2.2.1 Catenary mooring

Catenary anchored mooring lines are often used in shallow water. The mooring lines hang freely from the floating body and are connected to anchors on the seabed with relatively large distances from the floating body. This generates very long mooring lines compared to the water depth. The motions of a floating body disturb the equilibrium configuration of the mooring system in such a way that a restoring force is generated due to the weight of the mooring system. The length of the mooring lines increases excessively with increasing water depth, resulting in an increase in weight of the mooring lines that reduces the working payload of the floating body. To reduce this reduction in working payload it is a possibility to have a composite mooring line with different components along the mooring line. In the case of the thesis the mooring line only consists of one component.

The used CALM buoy is catenary moored with a 6x1 mooring configuration with an angle of 60 degrees between the lines in the horizontal plane (AMOG, 2017), which can be seen in Figure 2-5. Each mooring line consists of 95mm studless chain with an ABS grade R4 with an straight length of 420m. The anchor points are located with a radius of approximately 400m in the x-y-plane. The properties of the mooring line segment (Ramnäs Bruk, 2009) are shown in Table 2-2 and the detailed CALM buoy configuration can be found in Appendix 9.1.

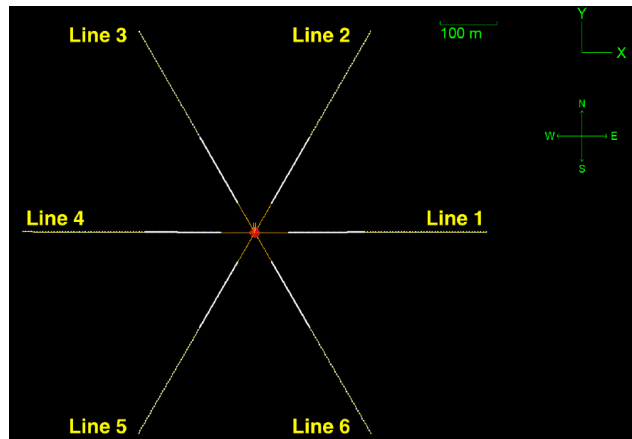


Figure 2-5 Top view mooring configuration.

Table 2-2 Mooring lines properties.

Property	Value
Length [m]	420
Anchor points radius [m]	400
Anchor depth [m]	37
Diameter mooring line [m]	0,095
Axial stiffness [kN]	812e3
Break load [kN]	9001e3
Submerged weight per meter [kg/m]	172

2.3 Host vessel

The vessel on which the Ampelmann system will be installed during actual operation is a tugboat, the Svitzer Vision. To include the host vessel in the model later on, very specific properties of the vessel are required which are not all available for this vessel. Since the host vessel is not a prior part of the model, it is sufficient to use a host vessel with similar governing properties and dimensions. In collaboration with MARIN a comparable vessel has been found with all specific details required for the model. Table 2-3 shows the main particulars of the Svitzer Vision (Svitzer, 2018) and the model vessel provided by MARIN.



Figure 2-6 Svitzer Vision.

Table 2-3 Properties of the Svitzer vision and the host vessel used.

Property	Svitzer Vision	MARIN model
Length between perpendiculars (LPP) [m]	50	50
Breadth [m]	16	13,5
Draft [m]	5,5	4,25
Mass [ton]	Unknown	2153
COG wrt keel [m,m,m]	Unknown	[24,5 0 5,75]
Radii of gyration, roll [m]	Unknown	4,72
Radii of gyration, pitch [m]	Unknown	12,5
Radii of gyration, yaw [m]	Unknown	12,5

2.4 Location

The buoy used in this thesis is located in the Gulf of Papua, Papua New Guinea. It lies at the Kumul site in the Northwestern Gulf of Papua near the Omati river delta with global coordinates Lat. 08° 07' 54" S, Long. 144° 34' 24" E.



Figure 2-7 Global location of CALM buoy.

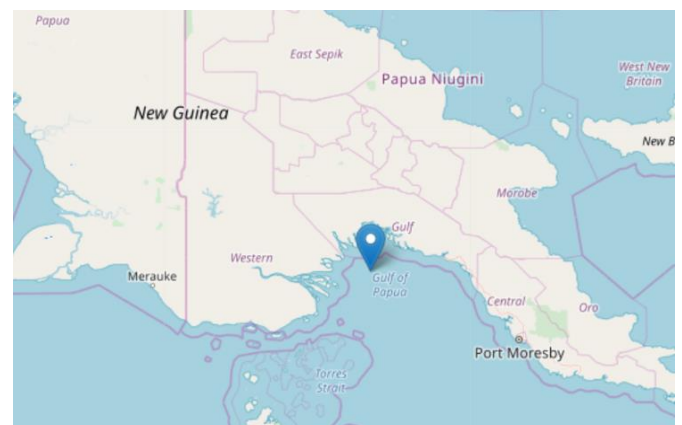


Figure 2-8 Zoomed location of CALM buoy.

3. Hydrodynamic model

3.1 Introduction

In this thesis Difffrac is used to calculate the hydrodynamic properties of the floating bodies. Difffrac is an in-house software package constructed by MARIN, which calculates the wave loads and motion responses of floating bodies including their hydrodynamic interaction. Difffrac generates a hydrodynamic database for the frequency dependent properties as; added mass, potential damping, force response amplitude operators (RAO's), quadratic transfer functions (QTF's). This chapter explains how the software works and how the diffraction model of the CALM buoy is built up and executed.

3.2 EOM

The dynamic response of the buoy is a key element. To find the hydrodynamic response, the equations of motion of the buoy will be solved. The equations of motion for the buoy follow from Newton's second law, which states that the rate of change of momentum of a body is directly proportional to the force applied in the direction of the force.

$$\frac{d(mv)}{dt} = F \quad (3.1)$$

This can be written in matrix form for all degrees of freedom.

$$M\ddot{X} = \sum F \quad (3.2)$$

Where

M = The 6x6 mass matrix of the buoy

\ddot{X} = The 6x1 acceleration vector of the buoy

$\sum F$ = The 6x1 force and moment vector (1..3 = forces, 4...6 = moments)

Without external forces acting on the buoy, the force and moment vector can be split into the wave-exciting force from the incoming wave, F_w , which consists of the Froude-Krylov force, F_{fk} , and the diffraction force, F_d , the radiation force from the 6 degrees of freedom of the body, F_r , and the hydrostatic reaction force F_s .

Where according to Journée (J.M.J. Journée, 2008) these forces can be written as

$$F_w = F_{fk} + F_d \quad (3.3)$$

$$F_r = -A\ddot{X} - C\dot{X} \quad (3.4)$$

$$F_s = -KX \quad (3.5)$$

Where it is assumed that these forces are calculated for a constant frequency.

This shows that the radiation force has a part that is in phase with the acceleration and a part that is in phase of the velocity. Substituting equations 3.3-3.5 into 3.2 results in the equation of motion (equation 3.6).

$$(M + A)\ddot{X} + C\dot{X} + KX = F_w \quad (3.6)$$

In Difffrac the equation of motion is calculated for a chosen frequency range with a selected frequency step. This results in a hydrodynamic database including frequency dependent added mass matrix A ,

frequency dependent damping matrix C and the wave exciting force vector F_w . The mass matrix M and stiffness matrix K are calculated from the geometry of the buoy.

Calculating the frequency dependent hydrodynamic properties, equation 3.6 will be written in the frequency domain.

The wave exciting forces are proportional to the incoming waves which are a superposition of harmonic waves of different frequencies. When a harmonic wave is written as $\zeta = \zeta_a e^{i\omega t}$, with ζ_a as the wave amplitude, and the body excitation is written as $x = \tilde{X} e^{i\omega t}$, with a as the motion amplitude, the equation of motion in frequency domain can be written as

$$-(M + A(\omega))\omega^2 \tilde{X} e^{i\omega t} + C(\omega)i\omega \tilde{X} e^{i\omega t} + K \tilde{X} e^{i\omega t} = F_w \zeta_a e^{i\omega t} \quad (3.7)$$

From equation 3.7 the response amplitude operator (RAO) is computed. The RAO determines the response of a floating body to the incoming wavefield.

$$RAO = \frac{\tilde{X}}{\zeta_a} = \frac{F_w}{-\omega^2(M+A(\omega))+i\omega C(\omega)+K} \quad (3.8)$$

3.3 Potential theory

The hydrodynamic properties are calculated with 3D potential theory. The main assumptions that are made during this approach is that the wetted area stays constant, the fluid is incompressible, inviscid, irrotational and the fluid has no effect of surface tension. The potential function is derived such that the spatial derivatives are equal to the velocities of the water particles in that direction.

$$\phi(x, y, z, t) \text{ for which } u_x = \frac{\partial \phi}{\partial x}, u_y = \frac{\partial \phi}{\partial y}, u_z = \frac{\partial \phi}{\partial z} \quad (3.9)$$

The total potential of a floating body is a superposition of 3 potentials; the radiation potential due to the 6 DOF motions of the body (Φ_j), the potential due to the undisturbed incoming wave (Φ_w), and the potential due to the diffraction (Φ_d) as can be seen in equation 3.10.

$$\Phi = \sum_{j=1}^6 \Phi_j + \Phi_w + \Phi_d \quad (3.10)$$

For simplicity, equation 3.10 will be defined as

$$\Phi = \Phi_0 + \Phi_1 + \Phi_2 + \Phi_3 + \Phi_4 + \Phi_5 + \Phi_6 + \Phi_7 \quad (3.11)$$

Where

Φ_0 = Potential due to the undisturbed incoming wave

$\Phi_{1...6}$ = Radiation potential due to the 6 DOF motions

Φ_7 = Potential due to diffraction of the undisturbed incoming wave

To solve equation 3.11 a set of boundary of boundary conditions (Holthuijsen, 2007) has to be set. During the calculations the assumption is made that the body experiences small motions and small velocities such that only linear terms should be taken into account.

The first boundary condition used is based on the mass balance equation 3.12. By substituting the spatial derivatives from the velocity potential function, the continuity equation can be found (equation 3.13).

$$\frac{\partial u_x}{\partial x} + \frac{\partial u_y}{\partial y} + \frac{\partial u_z}{\partial z} = 0 \quad (3.12)$$

$$\frac{\partial^2 \phi}{\partial x^2} + \frac{\partial^2 \phi}{\partial y^2} + \frac{\partial^2 \phi}{\partial z^2} = 0 \quad (3.13)$$

The second boundary condition follows from applying the linearized Bernoulli equation at the free surface.

$$\frac{\partial \phi}{\partial t} + \frac{p}{\rho} + gz = 0 \quad (3.14)$$

$$\frac{\partial \phi}{\partial t} + g\eta = 0, \text{ at } z = 0 \quad (3.15)$$

For the third boundary condition, the kinematic boundary condition at the hull is applied.

$$\frac{\partial \phi}{\partial n} = \vec{v} * \vec{n} \quad (3.16)$$

For the fourth boundary condition it is assumed that the sea bed is watertight.

$$u_z = 0, \text{ at } z = -d \quad (3.17)$$

When the velocity potential is substituted, the following kinematic boundary condition at the sea bed is formulated.

$$\frac{\partial \phi}{\partial z} = 0, \text{ at } z = -d \quad (3.18)$$

To finalize the boundary conditions, the assumption is made that far away from the body there is no disturbance.

$$\lim_{R \rightarrow \infty} \Phi = 0 \quad (3.19)$$

Until now, no wave conditions are included in this approach. To solve equation 3.11 an unidirectional regular wave will be introduced, which can be super positioned to solve equation 3.11 for an irregular wavefield. The unidirectional regular wave is required to find the undisturbed incoming wave potential Φ_0 , which is stated in the following equation

$$\Phi_0 = \frac{\zeta_0 g}{\omega} * \frac{\cosh(k(h_0+z))}{\cosh(kh)} e^{ik(x\cos(\mu)+y\cos(\mu))} \quad (3.20)$$

Where

ζ_0 = amplitude of the undisturbed wave [m]

ω = wave frequency [rad/s]

k = wave number [rad/m]

λ = wavelength [m]

μ = wave direction measured from the x-direction [rad]

h_0 = distance from the origin of the earth-fixed coordinate system to the sea bed [m]

h = water depth [m]

To find the radiation potential for every degree of freedom ($\Phi_{1...6}$) and the diffraction potential (Φ_7) an equation has been computed, represented by a continuous distribution of single sources on the body surface.

$$\varphi_j(x, y, z) = \frac{1}{4\pi} \iint_{S_0} \sigma_j(\hat{x}, \hat{y}, \hat{z}) * G(x, y, z, \hat{x}, \hat{y}, \hat{z}) * dS_0 \text{ for } j = 1 \dots 7 \quad (3.21)$$

Where

$\sigma_j(\hat{x}, \hat{y}, \hat{z})$ = The complex source strength on the mean wetted body surface due to motion of the body in the j-DOF

$G(x, y, z, \hat{x}, \hat{y}, \hat{z})$ = The Green's function of source $\sigma_j(\hat{x}, \hat{y}, \hat{z})$ on point (x, y, z)

S_0 = the mean wetted body surface

The Green's function gives the impulse response of an inhomogeneous linear differential equation defined on a domain (J.M.J. Journée, 2008). It satisfies the Laplace equation and the boundary conditions at the seabed and the free surface. The influence of the radiation potential will die out at a far distance, which leads to the conclusion that the radiation potential satisfies the radiation boundary at infinity. Only the boundary condition at the wetted surface of the body remains. This boundary condition is used to find the unknown source strength σ_j by substituting the source strength in the boundary condition. This means that the source strength at the surface of the body equals to the velocity of the body in that direction.

The solution for all the potentials can be found by a complex operation, which is solved in Diffrac. From the velocity potentials the first-order pressures on the body are calculated.

$$p = -\rho \left(\frac{\partial \Phi_r}{\partial t} + \frac{\partial \Phi_w}{\partial t} + \frac{\partial \Phi_d}{\partial t} \right) \quad (3.22)$$

The hydrodynamic forces and moments can be found by integrating the pressure over the wetted area.

$$\vec{F} = \rho \iint_{S_0} \left(\frac{\partial \Phi_r}{\partial t} + \frac{\partial \Phi_w}{\partial t} + \frac{\partial \Phi_d}{\partial t} \right) \vec{n} * dS \quad (3.23)$$

$$\vec{M} = \rho \iint_{S_0} \left(\frac{\partial \Phi_r}{\partial t} + \frac{\partial \Phi_w}{\partial t} + \frac{\partial \Phi_d}{\partial t} \right) (\vec{r} \times \vec{n}) * dS \quad (3.24)$$

3.4 Panel distribution

The submerged part of the buoy is modeled as a homogeneous cylinder with a draft of 2.76m and a diameter of 12.5m (AMOG, 2017). To use a discretized form of solving the potentials, the continuous body needs to be discretized. This is done by dividing the continuous circumference into discretized panels, which forms a mesh. The size of the panels needs to be chosen such that the frequency range of body motion is sufficiently big and that the discretization of the panels will not influence the results. A rule of thumb for the panel size regarding the frequency range is that the panel size should be 20% of the shortest wave, thus the highest frequency. According to equation 3.25, the panel size for a maximum frequency of 5 rad/s is 0.5m.

$$\lambda = \frac{g}{2\pi} T^2 \quad (3.25)$$

To check whether the panel size influences the result, a convergence study has been done with an increasing panel size from 0.25m until 1.5m. From Figure 3-1 it can be seen that the panel size does not have a significant influence on the result. To keep the computational time as limited as possible it is desired to have the largest panel size possible, which decreases the amount of panels. Based on equation 3.25 and Figure 3-1 an average panel size of 0.5m is chosen which result in 1424 panels.

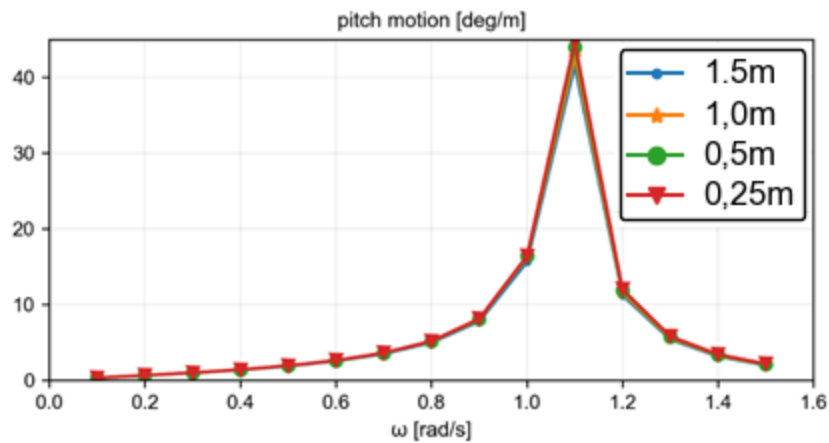


Figure 3-1 Panel size convergence study.

3.5 Configuration vessel and buoy

Due to the constraints of this thesis, the host vessel will not be included in the numerical model, but the influence of diffraction of a host vessel side by side the buoy will be studied. The way the host vessel is positioned next to the vessel is shown in Figure 3-2. Studying the influence of diffraction is done by comparing the RAO's of the buoy in a configuration where only the moored buoy is present, to a configuration where the moored buoy is positioned next to a host vessel.

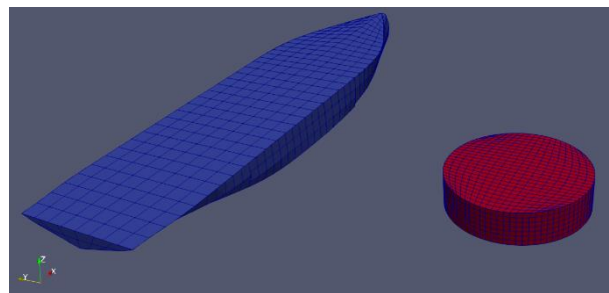


Figure 3-2 Configuration host vessel and buoy.

The mesh file of the host vessel is based on a vessel similar to the Svitzer Vision, and the main particulars can be found in Table 2-3.

3.6 Added damping

The total damping of a floating body consists of 2 parts; potential damping and viscous damping. Potential damping is caused by the motions of the body generating waves that radiate away from the body. These waves transport energy that dissipates from the oscillating body causing the motion to damp. Viscous damping is the result of the viscosity of the fluid causing friction. Potential damping is calculated by potential theory in Diffrac but viscous damping is difficult to calculate theoretically. Nowadays viscous damping is found by decay model testing which is not included in the scope of this thesis. Usually the viscous damping is a small part of the total damping for large floating structures. Since the buoy is a relatively small floating body, viscous damping should be added to have the buoy modeled as accurately as possible. Especially for roll and pitch motions of a buoy the total damping is largely underestimated if only potential damping is included (L.V.S. Sagrilo, 2002). Roll and pitch motions cause very little disturbance to the fluid which result in very little energy dissipated from the motion. But from model decay tests in previously done researches it shows that a forced roll motion decays faster than it should do according to only potential damping. Because of these reasons viscous damping is added manually in Diffrac to reach a higher accuracy of the buoy model. A rule of thumb (MARIN, 2011) is to set the total damping in roll and pitch to 3% of the critical damping. To calculate the critical damping (C_{crit}) first the natural frequency for each degree of freedom is calculated by solving equation 3.26 which follow from equation 3.7.

$$\det[K - \omega^2(M + A(\omega))] = 0 \quad (3.26)$$

The critical damping is calculated by equation 3.27 with the natural frequency known.

$$C_{crit} = 2(M + A_{\omega_n}) \omega_n \quad (3.27)$$

3.7 Mooring stiffness

Mooring lines have a significant impact on the response of the buoy. Even though the mooring lines are not physically present in the Diffrac model, they do impact the result of the diffraction model. The mooring lines add stiffness to the body that influences the response of the buoy. The motions of the body do not have any effect on the added mass, potential damping or the force RAO, but it does affect the QTF's and second order wave forces. Due to this, at first the horizontal mooring stiffness is added in the Diffrac model. With this model, offset tests are done in aNySIM, finding the total stiffness matrix of the moored buoy and this is used for the final diffraction data.

Figure 3-3 shows the horizontal restoring force of the moored buoy in the direction of a mooring line (AMOG, 2017) with a given offset. AMOG researched the effect of trenched mooring lines for this specific CALM buoy configuration, but for this research only the flat (blue) line is used. Figure 3-3 shows the linearity between the offset and horizontal restoring force until approximately 4 meter.

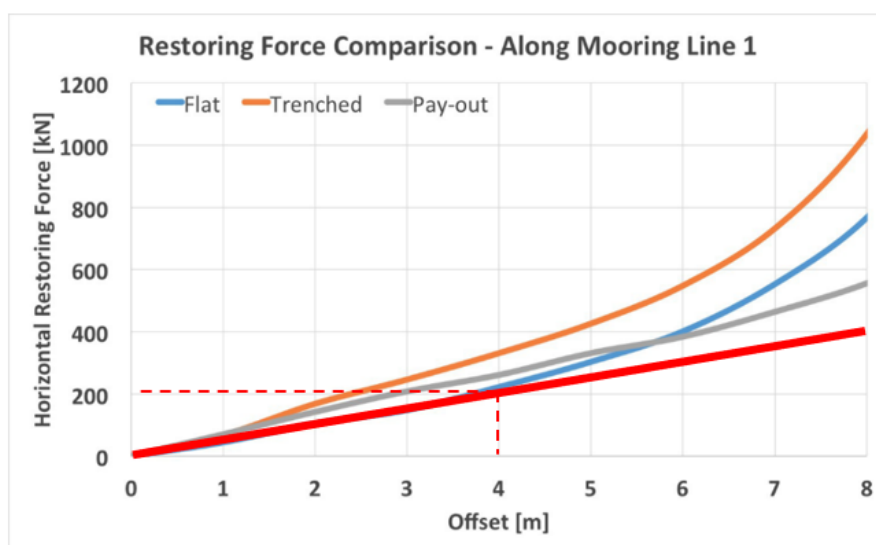


Figure 3-3 Horizontal restoring force vs offset.

The horizontal restoring force in Figure 3-3 represents the total restoring force in the direction of a mooring line. Graphs are available for all mooring lines and they all show similar results (Appendix 9.2). The stiffness of the moored buoy in surge and sway, k_{11}, k_{22} respectively, are set to 50 kN/m according to the linearization of Figure 3-3. For the first run in Diffrac, the stiffness from the mooring lines in heave, roll and pitch are not included but only the hydrostatic stiffness is used in Diffrac. In chapter 4 the mooring lines are added in the numerical model and the total stiffness of the buoy is calculated. This is used to rerun Diffrac to get the hydrodynamical database as accurate as possible. Since unidirectional waves are used, the expected yaw motions are negligible and since there is no hydrostatic stiffness in yaw, this stiffness will remain zero. The hydrostatic spring stiffness for heave, roll and pitch, which follow from the Diffrac calculations, are compared with equations 3.28 and 3.29.

$$k_{33} = \rho g A_{wl} \quad (3.28)$$

$$k_{44} = k_{55} = \rho g \nabla GM \quad (3.29)$$

In the stiffness matrix, coupling stiffness terms can arise due to coupled motion. The main coupling terms of a free-floating body are the coupling effects between heave and roll and vice versa (k_{53}, k_{35} respectively). k_{53} and k_{35} occur if the center of floatation (LCF) does not coincide with the center of gravity (LCG) in the x-y-plane. Since the buoy is assumed to be a homogeneous cylinder, the LCG and

LCF are equal in the horizontal plane and the coupling terms does not exist. This results in the diagonal stiffness matrix for the moored buoy given below.

$$k = \begin{bmatrix} 50 & 0 & 0 & 0 & 0 & 0 \\ 0 & 50 & 0 & 0 & 0 & 0 \\ 0 & 0 & 1270 & 0 & 0 & 0 \\ 0 & 0 & 0 & 7784 & 0 & 0 \\ 0 & 0 & 0 & 0 & 7784 & 0 \\ 0 & 0 & 0 & 0 & 0 & 0 \end{bmatrix}$$

3.8 Results

The results of different Diffrac models are discussed. For all the results, unidirectional head waves are used, which causes surge, heave and pitch responses of the buoy.

3.8.1 Mooring lines

Mooring stiffness in surge and sway are added from the linearization of the mooring line forces from Figure 3-3. Including the mooring stiffness in the diffraction model will influence the RAO of the buoy in surge significantly and very slightly in pitch and roll. In Figure 3-4 and Figure 3-5 the blue line represents the free-floating buoy where the orange line represents the moored buoy.

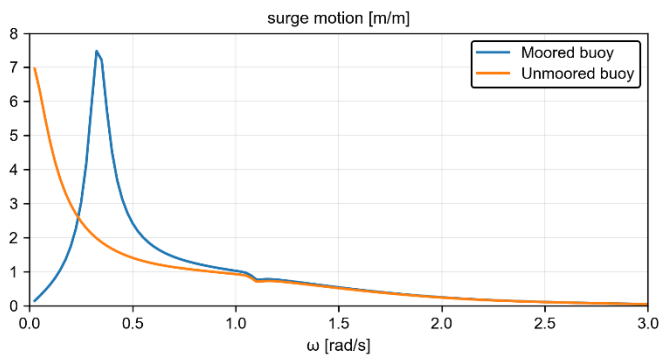


Figure 3-4 Surge RAO moored and unmoored buoy

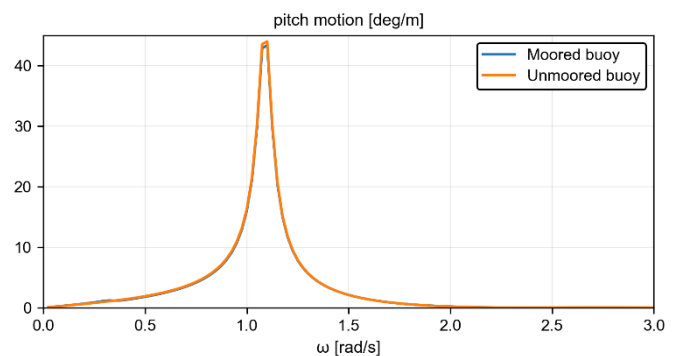


Figure 3-5 Pitch RAO moored and unmoored buoy.

Comparing the surge RAO's with and without mooring shows that the surge response of the buoy at low frequencies is lower than the unmoored buoy. Due to the introduced mooring stiffness, a natural frequency arises. After this peak, the RAO reacts similar to the RAO of the unmoored buoy. Since no additional stiffness is introduced in heave, and the heave motion is an uncoupled motion in the model, the RAO in heave is exactly the same for the moored and unmoored buoy. The pitch motion has a small coupling effect with the surge motion which results in a small decrease of the RAO peak.

3.8.2 Added mooring stiffness

To extend the accuracy of the diffraction model the mooring stiffness in all degrees of freedom is added. The total stiffness is derived from implementing the mooring lines in the numerical model and performing offset tests, done in chapter 4.4. Based on offset tests the stiffness matrix of the moored buoy is given below.

$$k = \begin{pmatrix} 50 & 0 & 0 & 0 & 0 & 0 \\ 0 & 50 & 0 & 0 & 0 & 0 \\ 0 & 0 & 1303 & 0 & 0 & 0 \\ 0 & 0 & 0 & 11017 & 0 & 0 \\ 0 & 0 & 0 & 0 & 11017 & 0 \\ 0 & 0 & 0 & 0 & 0 & 2600 \end{pmatrix}$$

The effect of heave and pitch will be studied since, due to unidirectional waves yaw motions will be negligible, and the surge stiffness has not changed. The blue line in Figure 3-6 shows the heave RAO with the damping matrix given in chapter 3.7 and the orange line shows the heave RAO with the damping matrix given in this chapter.

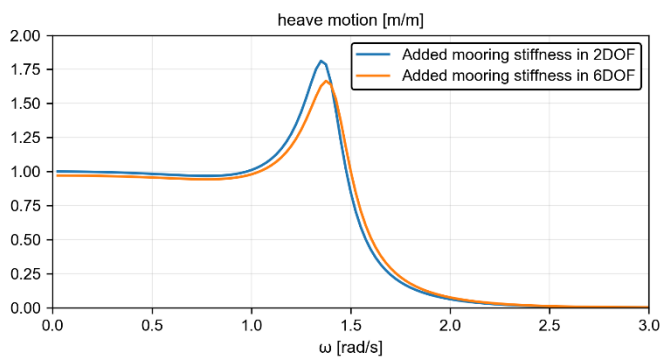


Figure 3-6 Heave RAO comparing stiffness matrix.

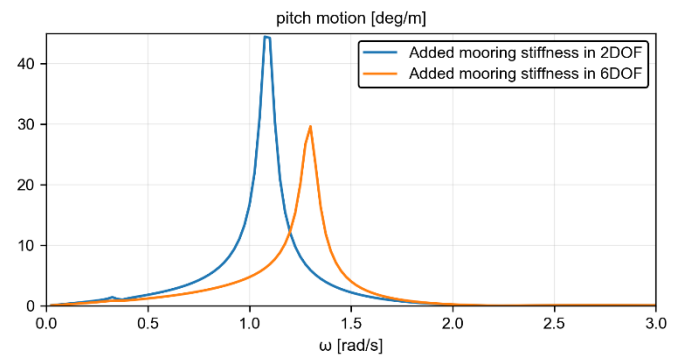


Figure 3-7 Pitch RAO comparing stiffness matrix.

It shows that the natural frequency slightly shifts to a higher frequency but the peak of the RAO is reduced. The pitch RAO (Figure 3-7) shows a larger difference in natural frequency shift and reduced peak. This is caused by the fact that the mooring lines add relatively more stiffness in pitch than in heave.

3.8.3 Diffraction

The influence of the host vessel positioned next to the buoy is visible when comparing the heave RAO (Figure 3-8) and roll RAO (Figure 3-9) of the buoy with and without the host vessel present. The blue line shows RAO's without diffraction included and the orange line shows the RAO's with diffraction included.

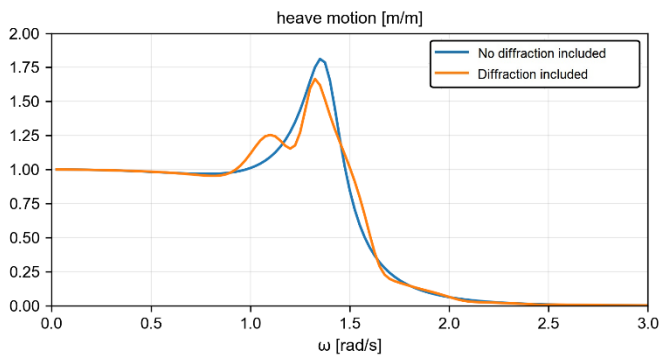


Figure 3-8 Heave RAO with and without diffraction.

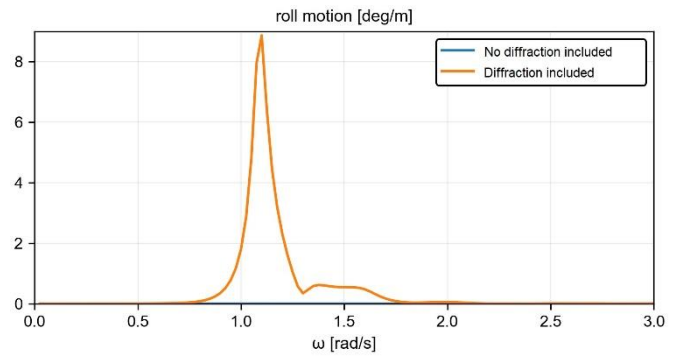


Figure 3-9 Roll RAO with and without diffraction.

The influence of diffraction caused by the host vessel does change the heave RAO. The heave RAO shows 2 peaks, one at the natural frequency of the host vessel and one at the natural frequency of the buoy. Another interesting phenomenon is the introduced roll motion caused by diffraction of the waves which is visible in Figure 3-8.

4. Numerical dynamic model

4.1 Introduction

The dynamic interaction of the CALM buoy and the Ampelmann system is modeled in a numerical dynamic model in aNySIM, which is an in-house developed software package of MARIN. The structure of the numeric model is explained in this chapter including a deliberate explanation for each component.

4.2 aNySIM

aNySIM is a numerical, dynamic, multi-body software package combining various modules of MARIN software. It is a time-domain simulation software which can simulate coupled motion behavior of a N-body system. The program uses the equations of motion, integrating the own inertia, added inertia, wave loads, damping loads and hydrostatic forces for each body. Besides being able implementing a number of floating bodies, additional modules can be coupled to them such as risers, mooring lines, DP-systems, etc. This modularity makes the software applicable for this thesis including the buoy, the mooring lines and external forces of the Ampelmann system. The frequency dependent added mass and hydrodynamic damping coefficients, which are derived from diffraction software, are transformed into inertia coefficients, retardation functions and response function (MARIN, 2018), which are given in equation 4.1.

$$\sum_{j=1}^6 (M_{kj} + A_{\infty}) \ddot{x}_j + \int_0^t R_{kj}(t - \tau) \dot{x}(\tau) d\tau + K_{kj} x_j = F_k(t) \quad (4.1)$$

Where

x_j = motion in j-th mode

$F_k(t)$ = time varying force in the k-th mode

R = matrix of retardation functions

The time varying forces can be first and second order wave forces, but also external forces acting on the body.

4.2.1 Structure model

The model configured in aNySIM consists of several parts directed from the 'Main' file. In this file the duration and the timestep of the simulation are determined. From the main file, 5 underlying files are used; 'Environment', 'Bodies', 'Hydrodynamical database', 'Logging' and 'External forces'. In the 'Environment' file the wind, wave and current conditions are defined. The 'Bodies' file implements all bodies in the simulation, which in this thesis are the buoy and the mooring lines. In the buoy file the geometric properties are defined and hydrostatic or hydrodynamic properties are be added. The mooring lines are defined by its material properties and by the configuration of the mooring lines. The hydrodynamical properties of the buoy are called in by the 'Hydrodynamical database' file. The 'Logging' file determines the outputs of the simulation and these will be saved as time-series. The Ampelmann forces are calculated in the 'External forces' file which is coupled to the buoy. As a summary, the overview of all files and the layer they are in are shown in Figure 4-1.

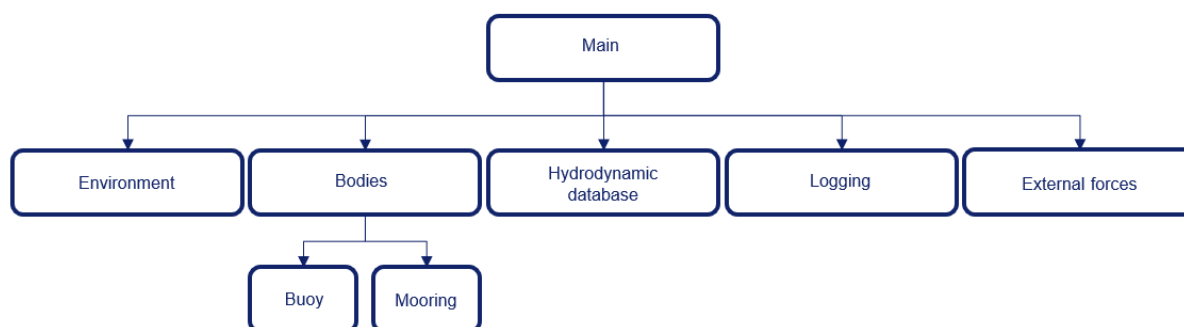


Figure 4-1 Overview structure aNySIM model.

4.3 Buoy

The body of the buoy is modeled as a homogeneous solid cylinder without a skirt (Figure 3-2). The hydrodynamic and hydrostatic properties are derived in the hydrodynamical database. Due to approach of potential theory in Diffrac, viscous damping is not included in the hydrodynamical database. This results in a underestimated damping coefficient especially for roll and pitch motion (T.H.J. Bunnink, 2002). In consultancy with MARIN the added viscous damping used is 3% of the critical damping for roll and pitch. The 3% of the critical damping is based on several model tests performed by MARIN. The critical damping is calculated in Diffrac and verified by equation 3.27. This results in the following input parameters of the body of the buoy.

Table 4-1 Parameters buoy in aNySIM.

Parameter	
Diameter [m]	12,5
Height [m]	6,56
Additional viscous damping roll and pitch [kNms/rad] $b_{44} = b_{55}$	430
Mass [tonnes]	281,6
Radius of gyration roll and pitch [m], $k_{xx} = k_{yy}$	4
Radius of gyration yaw [m]	5

The stability of the floating buoy is tested in aNySIM with offset tests for heave, roll and pitch. The buoy has been given an initial offset and will be released. The restoring response showed that each motion is damped out until the buoy is back to its equilibrium. The results of the offset tests are shown in Appendix 9.4.

4.4 Mooring lines

The configuration of the mooring lines consists of 6 mooring lines with a 60 degree angle between each of them in the horizontal plane. The complete mooring line configuration can be found in Appendix 9.1. The mooring lines used in this thesis consist of studless 95mm steel chains with ABS grade 4 and its properties are shown in Table 4-2.

Table 4-2 Parameters mooring lines in aNySIM.

Parameter	
Anchor depth [m]	37
Diameter chain [mm]	95
Length mooring leg [m]	420
Axial stiffness [kN/m]	742,5e3
Break load [kN]	9,04e3
Mass per meter [kg]	180
Submerged weight per meter [kN]	1,692

For the kinematic approach of the workability study, conducted by Ampelmann, modelling the CALM buoy has been outsourced to AMOG consultancy. AMOG consultancy constructed a fully dynamic, non-linear model of the CALM buoy to create time series of the response of the buoy under specified environmental conditions (SOFEC, PNG CALM Buoy Design Loads Report, 2011). The inputs and results of the AMOG model will be used to build and validate the mooring lines in aNySIM.

The numerical model of the buoy is linearized in this thesis, which results in a linearization of the non-linear catenary anchored mooring lines (A. Umar, 2003). The mooring lines are modeled quasi-statically, meaning that the inertia of the mooring lines is ignored. Figure 3-3 shows that the restoring force in each mooring line in the horizontal plane can be linearized up to an offset of 4m in the horizontal plane.

4.4.1 Verification mooring lines

The mooring lines in aNySIM are compared to the results of the model of AMOG. This is done by comparing the static response of the CALM buoy and the tension in the mooring lines. To verify the horizontal restoring mooring force a step force is exerted on the CALM buoy and the offset in the direction of the force is studied.

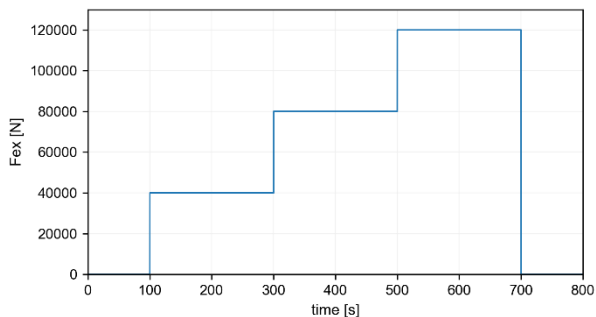


Figure 4-2 Step force in x-direction

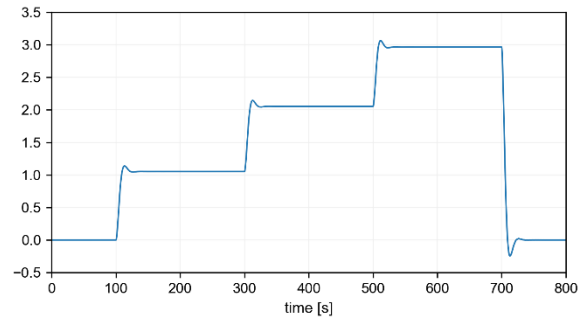


Figure 4-3 Offset buoy in x-direction

Figure 4-3 shows the offset of the CALM buoy over time with the step force from Figure 4-2 implemented. After a small overshoot the buoy responds linearly to the increasing step force which confirms the static linearity of the mooring lines up to an offset of 3m. The difference between the aNySIM model and the AMOG model is the stiffness of the mooring lines. From figure 4.2 it shows that the mooring stiffness in the horizontal plane is 50 kN/m while the aNySIM model shows a stiffness of 40 kN/m. The difference in stiffness will result in a different response of the buoy compared to the AMOG data, but since the focus of this thesis lies at the coupling between the Ampelmann system and the CALM buoy, it is not required to copy the exact AMOG model.

To test static linearity for the remaining degrees of freedom, the buoy has been given an increasing offset in each degree of freedom and the total force or moment on the buoy has been studied. The results are shown in Table 4-3, showing that within the tested range of static response of the buoy responds linearly. The working range of the static response tests are based on a maximum tilt of the buoy, and a significant heave motion.

Table 4-3 Results of static offset tests.

Degree of freedom	Offset step	Resulting force/moment
Heave	0,5 m	652 kN
	1,0 m	1303 kN
	1,5 m	1955 kN
Roll	0,1 rad	-1424 kNm
	0,2 rad	-2846 kNm
	0,3 rad	-4264 kNm
Pitch	0,1 rad	-1425 kNm
	0,2 rad	-2846 kNm
	0,3 rad	-4264 kNm
Yaw	0,1 rad	-257 kNm
	0,2 rad	-511 kNm
	0,3 rad	-760 kNm

The next step of validating the aNySIM model is to compare the equilibrium properties of the buoy to the AMOG model. The weight of the mooring lines introduces a pretension in the mooring lines, changing the draft of the free-floating buoy. The pretension and vertical force of the mooring lines are derived in the study of AMOG (SOFEC, Weight, Balance, Floatation & Stability Design Report for PNG CALM Buoy, 2011) and they are compared to the pretension and vertical force of the mooring lines modeled in aNySIM. Table 4-4 shows that forces in the mooring lines in equilibrium position of the AMOG model are very similar to those of the aNySIM model.

Table 4-4 Comparison pretension and vertical force mooring line.

	AMOG model	aNySIM model
Pretension per mooring line	13,00 MT	12,97 MT
Vertical force per mooring line	10,67 MT	10,92 MT

The draft of the CALM buoy, including the vertical force of the mooring lines, is calculated with equations 4.2-4.4.

$$M_b g + F_m = F_b \quad (4.2)$$

$$M_b g + F_m = \rho g T A \quad (4.3)$$

$$T = \frac{M_b g + F_m}{\rho g A} \quad (4.4)$$

With

M_b = Mass of the buoy [tonnes]

F_m = Total mooring force [kN]

F_b = Buoyancy force [kN]

T = Draft [m]

This results in a calculated draft of 2.76m, coinciding with draft of the moored buoy in aNySIM. The draft in aNySIM differs from the draft calculated by AMOG (3.08m). This can be explained by the differences of geometry of the buoy in aNySIM and AMOG. In aNySIM the buoy is modeled as a solid homogeneous cylinder without a skirt while AMOG included a skirt and a center well of the buoy. Another difference between both models is that in the AMOG model the operational hoses and chains are included (SOFEC, Weight, Balance, Floatation & Stability Design Report for PNG CALM Buoy, 2011) while in aNySIM these parts are not modeled. This can also change the draft of the CALM buoy.

4.4.2 Effect simplifications modeled buoy

The 2 main assumptions made in the aNySIM model of the CALM buoy are, the simplified geometry of the buoy, and the quasi-static mooring lines. Modeling the buoy as a solid cylinder removes the skirt of the buoy. The skirt (Figure 4-4) is a widening of the buoy at the bottom of the submerged part of the buoy adding damping in heave, roll and pitch (J.L. Cozijn, 2004). This has not been taken into account in the numerical model used in this thesis. Model tests of a buoy with a skirt are compared to a numerical model with a simplified skirt (T.H.J. Bunnink, 2002). The result of this study is that wave-exciting roll and pitch moments on the buoy are significantly affected by the skirt by mainly non-linear viscous damping effects. These effects cannot be derived from potential theory. Due to the fact that a skirt significantly affects the damping in roll and pitch, but can only be estimated by model tests, it has been decided not to implement the skirt in the geometry of the buoy. Additional viscous damping for roll and pitch is added manually as can be seen in Table 4-1.

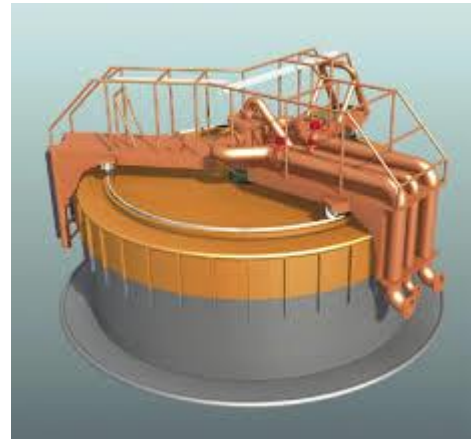


Figure 4-4 CALM buoy with skirt.

Modeling the mooring lines in a quasi-static manner will reduce the accuracy of the response of the modeled CALM buoy (J.L. Cozijn, 2004). In the study of Cozijn, the effect of this simplification is studied by comparing model tests, dynamically modeled simulations and quasi-statically modeled simulations. In quasi-static simulations, only the restoring forces of the mooring lines are included, which means that the drag and inertia loads of the mooring lines are not included. The lack of the dynamic behavior and hydrodynamic forces acting on the mooring lines will affect the response of the buoy. The natural frequencies and damping coefficients of the buoy will be affected by the dynamics of the mooring lines. Roll and pitch motions are overpredicted in irregular waves when the quasi-static approach is used. As mentioned before, the roll and pitch motion are difficult to model without model test verification. The added viscous damping added tries to model this as accurate as possible. The study of Cozijn also shows that the surge, sway and heave motions in irregular waves are overpredicted with the quasi-static approach. This will not be further investigated in this thesis making this study conservative.

4.5 Ampelmann system

The Ampelmann system will be modeled as external forces acting on the buoy. An in-plane configuration is used to study the effect of the gangway forces on the CALM buoy. The degrees of freedom of the gangway and the CALM buoy are reduced to 2 degrees of freedom in the this plane; telescoping and luffing. This chapter explains the method of implementing the external forces in aNySIM. The approach of determining the forces for each degree of freedom of the gangway is explained.

4.5.1 Implementing external forces

The forces acting on the buoy are calculated in an external file communicating with the files in aNySIM. The forces acting on the buoy, caused by the gangway of the Ampelmann system, are dependent on the motions of the buoy. The response of the buoy is both dependent on the incoming wave forces and the forces of the gangway. The motions of the buoy are implemented into the external force calculation file. These forces will be implemented onto the buoy, which affects the total forces acting on the buoy. The structure of this process is schematically shown in Figure 4-5.

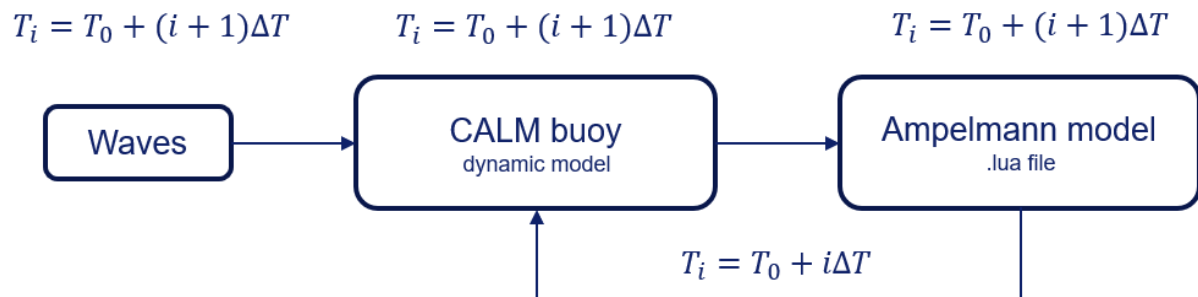


Figure 4-5 Schematic overview of implementing forces.

The Ampelmann forces onto the buoy are calculated based on the response of the buoy, lagging one timestep. The size of the timestep is crucial to make sure that the buoy is responding to the correct Ampelmann forces. The timestep chosen in the simulations is 0.1s. This was first advised by MARIN since they use this timestep size for all of their simulations. A sensitivity check has been performed by replacing the hydrostatics of the buoy in heave by a spring-damper system to compare the response of simulations including only the hydrostatic response and including only the external spring-damper system. They are a perfect match for a timestep of 0.1s.

4.5.2 In-plane model constraints

To study the coupling effect of the gangway forces and the motions of the buoy, the dynamic model will be restricted to in-plane motions. In this in-plane movement, the moored buoy has 3 degrees of freedom; sway (translation in y-direction), heave (translation in z-direction), and roll (rotation around the x-axis). The incoming wave direction is fixed and unidirectional, and will be coming from y-direction. The in-plane configuration of the model is shown in Figure 4-6.

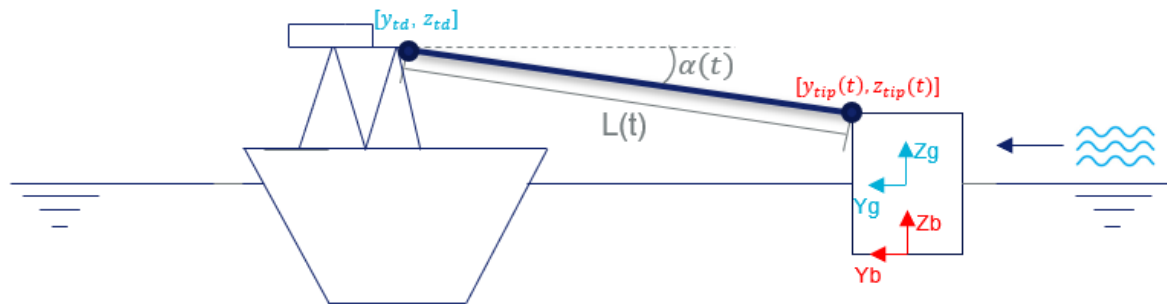


Figure 4-6 Schematic overview boundaries model.

The location of the transferdeck, thus the rotation point of the gangway, is fixed in space according to the constraints set up in chapter 1.3. The coordinates of the transferdeck are indicated by y_{td} , z_{td} in the global coordinate system (given in blue) and will not vary in time. The connection point of the gangway onto the buoy is located at [6.25, 6.56] in the body fixed coordinate system (given in red) (SOFEC, PNG CALM Buoy Report, 2011), which is indicated by $y_{tip}(t)$, $z_{tip}(t)$. The global tip coordinates $y_{tip}(t)$, $z_{tip}(t)$ are dependent on the motion of the buoy and will vary in time.

In this configuration the gangway has two degrees of freedom; luffing and telescoping. The luffing angle is indicated by $\alpha(t)$ and the gangway length is indicated by $L(t)$ which are dependent on the position of the buoy.

4.5.3 Telescoping force

The first degree of freedom that is studied is telescoping. The inertia of the gangway is neglected due to the relatively small mass of the moving parts of the gangway (1.4 tonnes) compared to the mass of the buoy (281 tonnes). Full-scale testing, done by Ampelmann, shows that the telescoping force consists of a damping force which is linearly dependent on the telescoping velocity, and a friction force which is fixed in magnitude but is always in opposite direction of the telescoping velocity. The friction force is caused by telescoping cables that pulls the T-boom of the gangway. From the Ampelmann tests, and the assumption of neglecting the mass of the gangway, the telescoping force is represented as a damper. Figure 4-7 shows the schematic representation of the moored buoy including the telescoping damper. The damper can still rotate around the rotation point at the transferdeck, but it does not introduce a force caused by rotation. The telescoping force is calculated by equation 4.5.

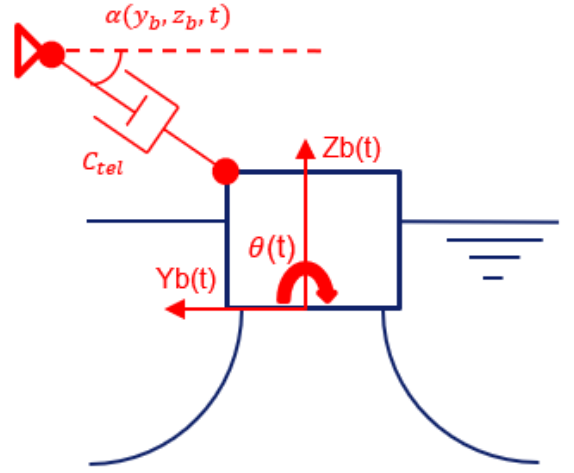


Figure 4-7 Schematic representation telescoping gangway.

$$F_{tel}(t) = -(C_{tel} v_{tel}(t) + F_{friction}(t)) \quad (4.5)$$

With the following parameters from the Ampelmann tests

$$C_{tel} = 9.894 \frac{Ns}{m}$$

$$F_{friction} = 4.500 N$$

The tip velocity of the gangway is equal to the velocity of the buoy at the connection point. This results that the motions of the buoy will determine the telescoping velocity. The approach calculating the telescoping velocity is calculating the length of the gangway and taking the time derivative of the gangway length to find the telescoping velocity. The length of the gangway is calculated by equation 4.6.

$$L(t) = \sqrt{(y_{td} - y_{tip}(t))^2 + (z_{td} - z_{tip}(t))^2} \quad (4.6)$$

Equation 4.6 can be rewritten as

$$L^2(t) = (y_{td} - y_{tip}(t))^2 + (z_{td} - z_{tip}(t))^2 \quad (4.7)$$

And taking the time derivative of equation 4.7 results in the telescoping velocity given in equation 4.8.

$$v_{tel}(t) = \dot{L}(t) = \frac{-y_{tip}(t)(y_{td} - y_{tip}(t)) - z_{tip}(t)(z_{td} - z_{tip}(t))}{L(t)} \quad (4.8)$$

The final step of calculating the telescoping force is implementing friction force. The friction force is only changing direction but maintaining the same magnitude. To ensure a smooth transition between positive and negative values of the friction force it is written according to equation 4.9 including the tangent hyperbolic function. Since the result of the tangent hyperbolic function should be either 1 or -1, also for low telescoping velocities, the telescoping velocity is multiplied by 5 inside the tangent hyperbolic function.

$$F_{friction}(t) = \tanh(5 v_{tel}(t)) F_{friction} \quad (4.9)$$

In aNySIM it is only possible to implement external forces in the global coordinate system. The direction of the telescoping force is always in line with the gangway, which position changes in time. $y_{tip}(t)$ and $z_{tip}(t)$ are known at all time in the simulations, so the telescoping force can be projected into the global coordinate system. This is shown in Figure 4-8.

Projecting the local velocities of the buoy into the direction of the gangway the luffing angle is calculated by equation 4.10.

$$\sin(\alpha) = \frac{z_{td} - z_{tip}(t)}{L(t)} \quad (4.10)$$

This results in the following telescoping forces at the tip location of the buoy in the global coordinate system.

$$F_{y_{tel}}(t) = -F_{tel}(t) \cos(\alpha(t)) \quad (4.11)$$

$$F_{z_{tel}}(t) = -F_{tel}(t) \sin(\alpha(t)) \quad (4.12)$$

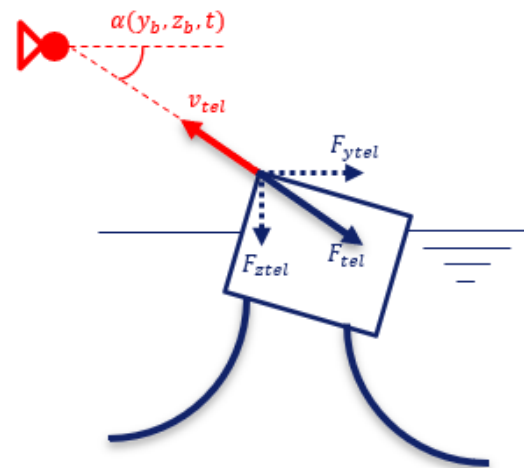


Figure 4-8 Projection telescoping force.

4.5.4 Luffing force

The second degree of freedom for the in-plane motion of the gangway is luffing. During luffing the gangway rotates around the rotation point at the transferdeck. For luffing it is also assumed that the inertia of the gangway is negligible. Again, the gangway can be modeled with only a damper since the result of the full-scale tests conclude that the spring stiffness can be neglected. The major difference between telescoping and luffing is that the damper which is modelling the force, caused by the motion of the gangway, is a rotational damper. Figure 4-9 shows the schematic representation of the CALM buoy including the luffing damper. As a result from the full-scale tests done by Ampelmann it shows that friction can be neglected. The rotational luffing damper applies a moment at the connection point of the gangway on the buoy. The luffing moment is given by equation 4.13.

$$M_{luf}(t) = C_{luf} \dot{\alpha}(t) \quad (4.13)$$

With the damping coefficient following from the Ampelmann tests.

$$C_{luf} = 746.840 \frac{Nms}{rad}$$

Implementing the luffing moment in aNySIM is done by converting the luffing moment to a luffing force, which is always perpendicular to the gangway and is fixed at the tip location of the buoy. This is shown in Figure 4-9 with the luffing force calculated by equation 4.14.

$$F_{luf}(t) = \frac{C_{luf} \dot{\alpha}(t)}{L(t)} \quad (4.14)$$

The angular luffing velocity is the time derivative of the luffing angle $\alpha(t)$. This results in equation 4.15 for the luffing velocity.

$$\dot{\alpha}(t) = \frac{-L(t)z_{tip}(t) - (z_{td} - z_{tip}(t))L(t)}{L^2(t) \cos(\alpha)} \quad (4.15)$$

Implementing the luffing force at the tip location of the buoy in aNySIM it is required to project the luffing force in the global coordinate system. This projection is shown in Figure 4-10. With equations 4.16 and 4.17 for the projected luffing forces.

$$F_{yluf}(t) = -F_{luf}(t) \sin(\alpha(t)) \quad (4.16)$$

$$F_{zlu}(t) = F_{luf}(t) \cos(\alpha(t)) \quad (4.17)$$

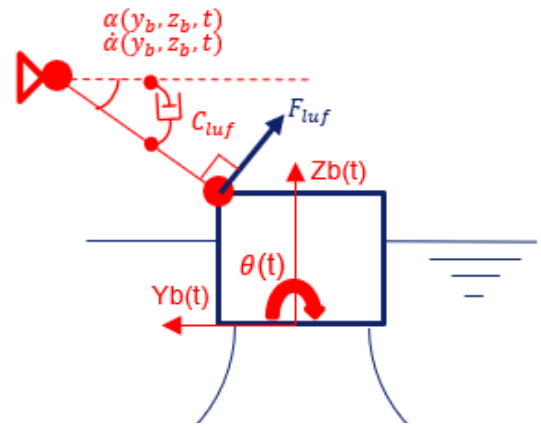


Figure 4-9 Schematic overview luffing force.

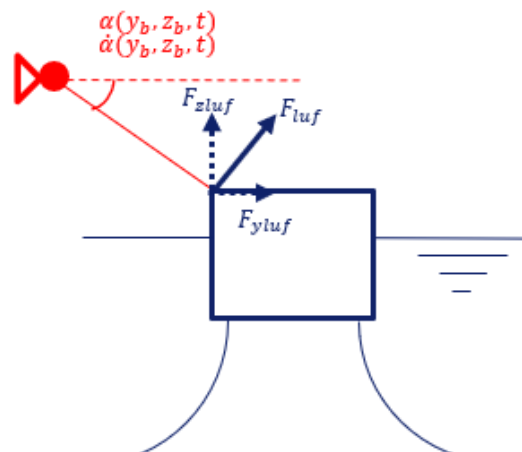


Figure 4-10 Projection luffing force.

5. Analytical approach

5.1 Introduction

To study the effect of the gangway forces on the response of the buoy in the y-z plane, the equations of motions of the buoy including the gangway forces are set up analytically. For the analytical approach the CALM buoy including the hydrostatic and hydrodynamic properties are schematically represented. With this representation of the CALM buoy, a free-body analysis is performed, resulting in the equations of motion of the CALM buoy for sway, heave and roll. The damping forces introduced by the gangway are included in the total damping matrix of the buoy and via a sensitivity study the governing parameters are studied. The equations of motion are solved using an ordinary differential equation solver written in Python. Finally the aNySIM model is compared with the Python model and the effect of the gangway forces on the response of the buoy are determined.

5.2 Mass-spring-damper system

Studying the coupling effect of the gangway on the buoy, the model configuration used in chapter 4 (Figure 4-6) are used to create a schematic representation of the hydrodynamic buoy including the mooring lines and the gangway forces. The schematic representation is shown in Figure 5-1.

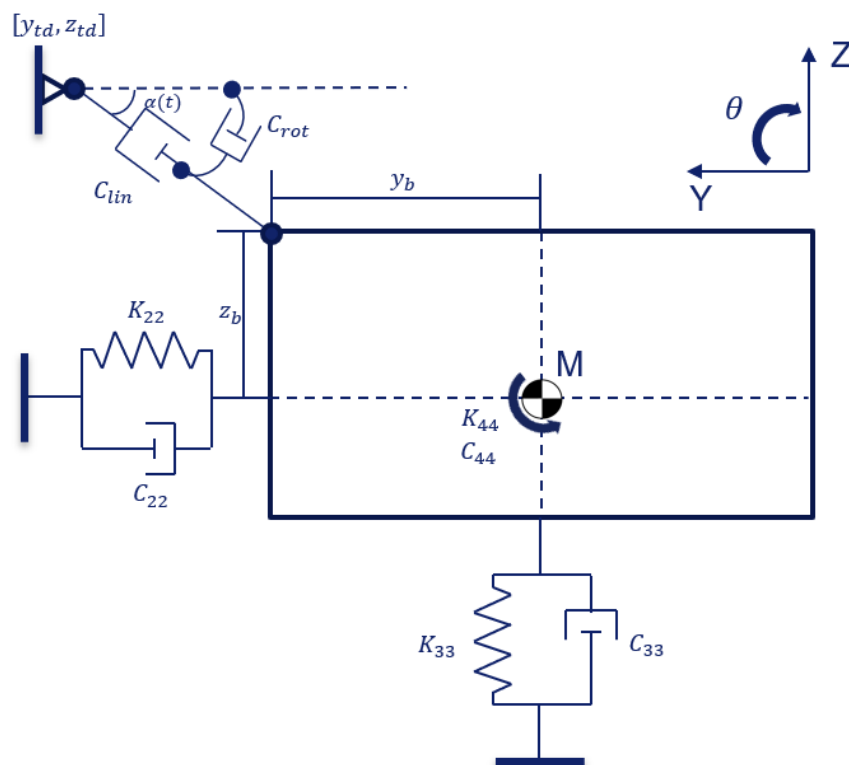


Figure 5-1 Schematic representation of a CALM buoy in the y-z-plane.

The total damping and stiffness of each degree of freedom of the buoy are implemented as an equivalent linear damper, linear spring, rotational damper or rotational spring. K_{22} , K_{33} and K_{44} are the equivalent stiffness in sway, heave and roll respectively. The equivalent stiffness consists of hydrostatic stiffness of the buoy and linearized mooring stiffness. It is assumed that, due to the symmetrical configuration of the mooring lines, the complete mooring system can be replaced by a spring in each degree of freedom. The equivalent damping for sway, heave and roll (C_{22} , C_{33} and C_{44} respectively) consists of hydrodynamic damping calculated in the diffraction software and the added

viscous damping. The damper is implemented as a massless damper for telescoping and luffing which is identical to the gangway forces in the aNySIM model.

5.3 Equations of motion

The equations of motion of the CALM buoy are derived using the displacement method. The buoy had been given a certain displacement and velocity in each degree of freedom, which will result in forces and moments caused by the springs and dampers of the system. All forces will be projected into global y- and z-direction and the equation of motion will be set up. The equation of motion is of the form

$$(M + A)\ddot{X} + C\dot{X} + KX = F_{waves} + F_{mooring} + F_{gangway} \quad (5.1)$$

Where

M = Mass matrix of the buoy

A = Added mass matrix of the buoy

C = Hydrodynamic damping matrix of the buoy

K = Hydrostatic stiffness matrix of the buoy

\ddot{X} = N-dof vector of the acceleration of the buoy

\dot{X} = N-dof vector of the velocity of the buoy

X = N-dof vector of the translation of the buoy

F_{waves} = The force vector of wave forces/moments

$F_{mooring}$ = The force vector of mooring forces/moments

$F_{gangway}$ = The force vector of the gangway forces/moments

To combine the hydrostatic stiffness and hydrodynamic damping with the added stiffness of the mooring lines and the added damping of the gangway, the mooring and gangway forces can be written as

$$F_{mooring}(t) = -K_m X \quad (5.2)$$

$$F_{gangway}(t) = -C_{gw} \dot{X} \quad (5.3)$$

Where

K_m = Linearized stiffness matrix of the mooring system

C_{gw} = Damping matrix of the inclined gangway

Substituting equations 5.2 and 5.3 in equation 5.1 results in equation of motion given in equation 5.4.

$$M_{eq}\ddot{X} + C_{eq}\dot{X} + K_{eq}X = F_{waves} \quad (5.4)$$

Where

M_{eq} = The equivalent mass matrix of the buoy

C_{eq} = The equivalent damping matrix including the hydrodynamic damping and the damping of the gangway

K_{eq} = The equivalent stiffness matrix including the hydrostatic stiffness and the linearized stiffness of the mooring lines

Limiting the response of the buoy to in-plane motions, will create 3X3 matrices and 3X1 vectors in the EOM of the following form

$$Matrix = \begin{bmatrix} \cdot\cdot22 & \cdot\cdot23 & \cdot\cdot24 \\ \cdot\cdot32 & \cdot\cdot33 & \cdot\cdot34 \\ \cdot\cdot42 & \cdot\cdot43 & \cdot\cdot44 \end{bmatrix} \quad Vector = \begin{bmatrix} \cdot\cdot2 \\ \cdot\cdot3 \\ \cdot\cdot4 \end{bmatrix}$$

Where the subscript '2' represents sway, '3' represents heave and '4' represents roll.

5.4 Small angle approximation

The equations of motion of the buoy are set up for sway, heave and roll separately. Sway and heave motions and velocities will result in uncoupled sway and heave responses, but roll motions and velocities will create a velocity of the connection point of the gangway in y- and z-direction. The damping forces of the gangway are linearly dependent to the velocities of the buoy at the connection point. To study the effect of the gangway forces on the response of the buoy it is beneficial to reduce the input parameters and to do so the small angle approximation is used. The velocities in y- and z-direction of the connection point of the gangway are calculated with and without the small angle approximation and the difference between both methods are analyzed. By using the small angle approximation it is assumed that the angle of a certain motion is small enough that the trigonometric function can be linearized around its equilibrium. The velocity of the connection point is projected in the direction of telescoping and luffing to conclude the effect of using the small angle approximation on the telescoping and luffing force separately.

5.4.1 Global velocity

Figure 5-2 shows a positive roll motion of the buoy. The connection point of the gangway on the buoy is located at $[y_{tip}, z_{tip}]$ with respect of the cog of the buoy in the body-fixed coordinate system. The buoy has been given a positive roll deviation, θ , with respect to the equilibrium position to calculate the global velocity of the connection point caused by a positive roll velocity, $\dot{\theta}(t)$. The global velocity will later be used to project the velocity into the direction of the telescoping and luffing gangway.

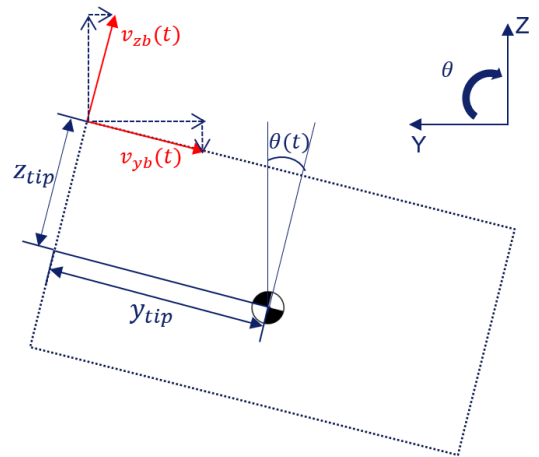


Figure 5-2 Projected velocities caused by roll.

The y- and z-velocity at the tip connection point in the body-fixed coordinate system are found by analyzing the rigid body dynamics (Greenwood, 2012) of the buoy which results in equation 5.5 and 5.6.

$$v_{zb}(t) = y_{tip} * \dot{\theta}(t) \quad (5.5)$$

$$v_{yb}(t) = z_{tip} * \dot{\theta}(t) \quad (5.6)$$

The body-fixed velocities are projected into the global coordinate system. The global velocities are calculated by equation 5.7 and 5.8.

$$v_{zg}(t) = [y_{tip} \cos(\theta(t)) - z_{tip} \sin(\theta(t))] \dot{\theta}(t) \quad (5.7)$$

$$v_{yg}(t) = -[y_{tip} \sin(\theta(t)) + z_{tip} \cos(\theta(t))] \dot{\theta}(t) \quad (5.8)$$

5.4.2 Luffing velocity

The luffing force introduced by the gangway on the buoy depends on the velocity perpendicular to the gangway. The global velocity is projected into the luffing direction (Figure 5-3) which is used to find the luffing force. Determining the effect of the small angle approximation on the luffing force, the luffing velocity will be analyzed with and without the small angle approximation using a case study.

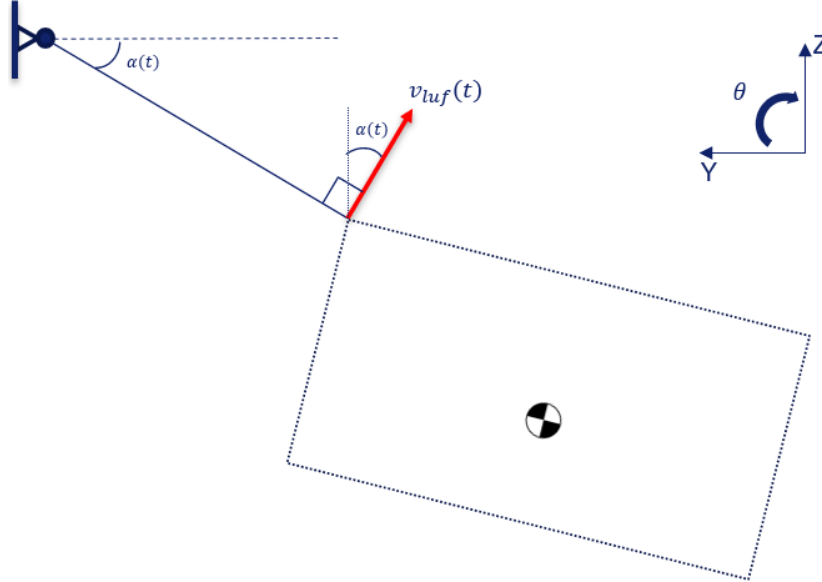


Figure 5-3 Luffing velocity caused by roll motion.

The luffing velocity (equation 5.9) is calculated by projection of the global velocities.

$$v_{luf} = \cos(\alpha(t)) v_{zg} + \sin(\alpha(t)) v_{yg} \quad (5.9)$$

Implementing equations 5.7 and 5.8 into equation 5.9 gives the luffing velocity in equation 5.10.

$$v_{luf} = \left[y_{tip} \left(\cos(\alpha(t)) \cos(\theta(t)) + \sin(\alpha(t)) \sin(\theta(t)) \right) + z_{tip} \left(-\cos(\alpha(t)) \sin(\theta(t)) + \sin(\alpha(t)) \cos(\theta(t)) \right) \right] \dot{\theta}(t) \quad (5.10)$$

Using the small angle approximation for roll motion the trigonometric functions are simplified to

$$\cos(\theta(t)) \approx 1$$

$$\sin(\theta(t)) \approx \theta(t)$$

And the luffing velocity including the small angle approximation becomes

$$v_{luf} = \left[y_{tip} \left(\cos(\alpha(t)) + \sin(\alpha(t)) \theta(t) \right) + z_{tip} \left(-\cos(\alpha(t)) \theta(t) + \sin(\alpha(t)) \right) \right] \dot{\theta}(t) \quad (5.11)$$

The last simplification that is studied in this chapter is the effect of neglecting the roll angle. When this is done the luffing velocity is calculated by equation 5.12.

$$v_{luf} = \left[y_{tip} \cos(\alpha(t)) + z_{tip} \sin(\alpha(t)) \right] \dot{\theta}(t) \quad (5.12)$$

A case study is used, determining the effect of calculating the luffing velocity by 3 different equations. The wave conditions used in the case study are derived from the most common sea state. Regular waves are coming in from y-direction (Figure 4-6) with a period of 4.5s and an amplitude of 0,75m. These environmental conditions are implemented in aNySIM to determine the range of the roll and

luffing angle, which are the variable parameters of the luffing velocity with a given roll velocity. Table 5-1 shows the minimum and maximum angles for the case study.

Table 5-1 Minimum and maximum angles case study.

	Minimum	Maximum
Roll angle (θ) [rad]	-0,17	0,14
Luffing angle (α) [rad]	0,12	0,27

The effect of the small angle approximation is studied using a luffing velocity factor, k_{luf} , which is independent of the roll velocity. The luffing velocity factor is defined according to equation 5.13.

$$k_{luf} = \frac{v_{luf}}{\dot{\theta}} \quad (5.13)$$

The luffing velocity factor is calculated for the minimum and maximum luffing angle following from Table 5-1. The only variable parameter for the luffing velocity factor is the roll angle.

The results of the luffing velocity factor, calculated by equation 5.10 (red line), 5.11 (blue line) and 5.12 (green line), are shown in

The results are shown in Figure 5-4 and Figure 5-5.

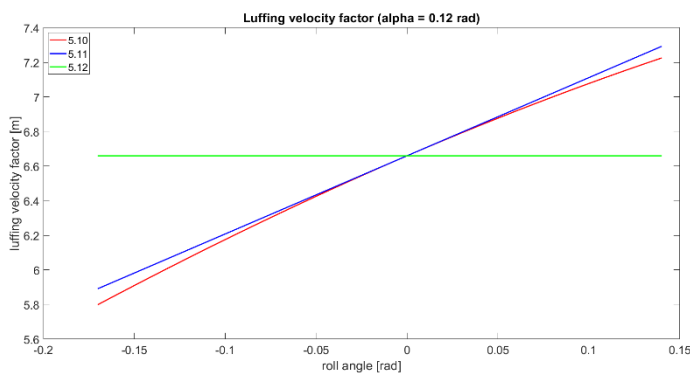


Figure 5-4 Luffing velocity factor (alpha=0.12 rad).

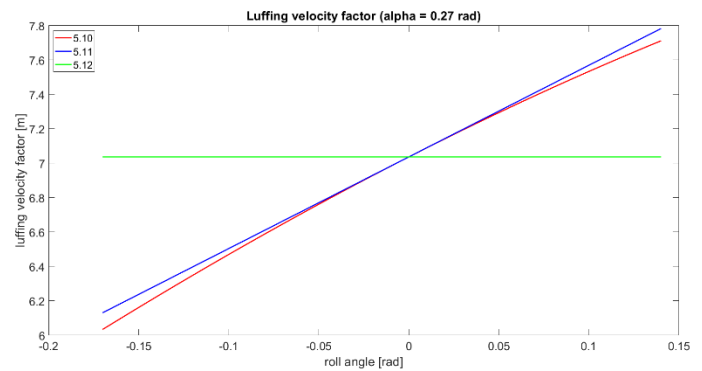


Figure 5-5 Luffing velocity factor (alpha=0.27 rad).

The luffing velocity factor calculated without any simplification (red) does not differ much (up to 1.6%) from the luffing velocity factor calculated with the small angle representation (blue). When roll is not included at all, the luffing velocity factor differs significantly compared to the results without any simplifications (up to 17%).

5.4.3 Telescoping velocity

The telescoping force is introduced by the velocity of the gangway in the direction of the gangway. This is visualized in Figure 5-6. The same approach, as what was used for calculating the luffing velocity, is used for calculating the telescoping velocity.

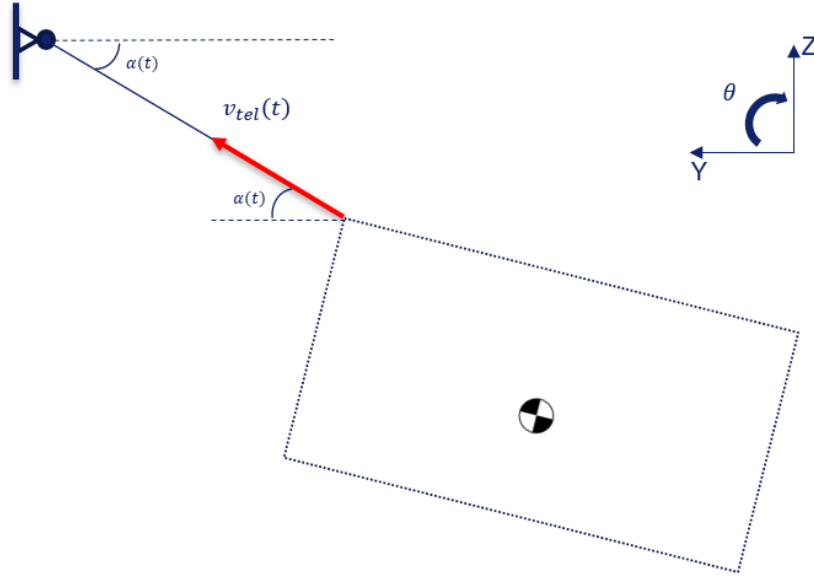


Figure 5-6 Telescoping velocity caused by roll motion.

The telescoping velocity is calculated by equation 5.14.

$$v_{tel} = \sin(\alpha(t)) v_{zg} - \cos(\alpha(t)) v_{yg} \quad (5.14)$$

Implementing equation 5.7 and 5.8 into 5.14 leads to the telescoping velocity.

$$v_{tel} = \left[y_{tip} \left(-\cos(\alpha(t)) \sin(\theta(t)) + \sin(\alpha(t)) \cos(\theta(t)) \right) + z_{tip} \left(-\cos(\alpha(t)) \cos(\theta(t)) - \sin(\alpha(t)) \sin(\theta(t)) \right) \right] \dot{\theta}(t) \quad (5.15)$$

Including the small angle approximation results in equation 5.16.

$$v_{tel} = \left[y_{tip} \left(-\cos(\alpha(t)) \theta + \sin(\alpha(t)) \right) + z_{tip} \left(-\cos(\alpha(t)) - \sin(\alpha(t)) \theta \right) \right] \dot{\theta}(t) \quad (5.16)$$

With neglecting the roll offset the telescoping velocity is given by equation 5.17.

$$v_{tel} = \left[y_{tip} \sin(\alpha(t)) - z_{tip} \cos(\alpha(t)) \right] \dot{\theta}(t) \quad (5.17)$$

In figure 5.7 and 5.8 the telescoping velocity factor is plotted versus the variable roll angle where the telescoping velocity factor, k_{tel} , is defined as

$$k_{tel} = \frac{v_{tel}}{\dot{\theta}} \quad (5.18)$$

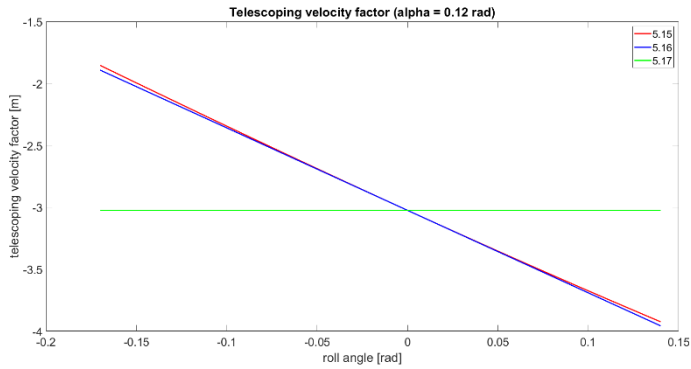


Figure 5-7 Telescoping velocity factor ($\alpha = 0.12$ rad).

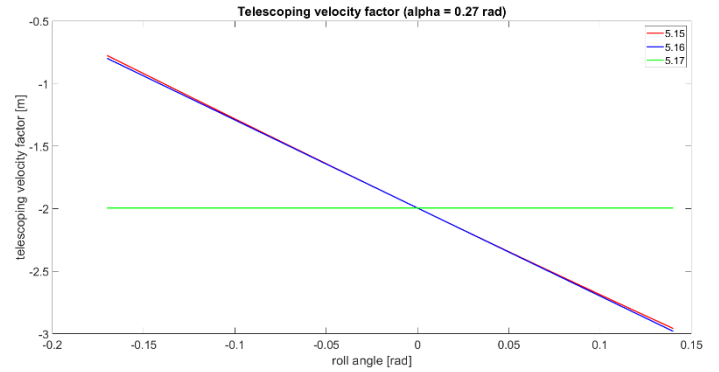


Figure 5-8 Telescoping velocity factor ($\alpha = 0.27$ rad).

The exact telescoping velocity factor (red) only differs 2.5% with respect to the telescoping velocity factor calculated with the small angle approximation (blue). The difference between the exact calculation and the calculation without the roll angle implemented (green) differs up to 156% for a maximum roll angle.

The results of the luffing and telescoping velocity factor calculated by 3 different equations show that the small angle approximation can and will be used in determining the damping forces caused by the gangway in the next chapters.

5.5 Telescoping damping matrix

Using the displacement method the equations of motion for the buoy are derived. The buoy is given an offset and a velocity in each degree of freedom separately and the forces caused by that displacement are set up in a free-body diagram based on Figure 5-1. This chapter includes the telescoping damper, and the luffing damper is studied in the next chapter. According to equation 4.5 the telescoping force is linearly dependent on the telescoping velocity. The displacement method introduces a velocity in each degree of freedom which causes a telescoping velocity. The telescoping velocity by a displacement in Y, and Z are given by equation 5.19 and 5.20

$$v_{tel}(sway) = \cos(\alpha) \dot{Y} \quad (5.19)$$

$$v_{tel}(heave) = \sin(\alpha) \dot{Z} \quad (5.20)$$

According to the small angle approximation, the telescoping velocity introduced by a roll displacement is given by equation 5.16.

For each displacement the projected telescoping forces (equations 4.11 and 4.12) are implemented in the model and the equations of motion are set up. The free body diagram analyses of each degree of freedom is shown in Appendix 9.6. The equations of motion of the buoy including the telescoping damper can be rewritten in the form of equation 5.4. This results in the following equivalent mass matrix and equivalent stiffness matrix, where the hydrostatic stiffness values can be found with equations 3.28 and 3.29.

$$M_{eq} = \begin{bmatrix} M + a_{22} & 0 & 0 \\ 0 & M + a_{33} & 0 \\ 0 & 0 & I_{xx} + a_{44} \end{bmatrix} \quad (5.21)$$

$$K_{eq} = \begin{bmatrix} K_{22} + K_{mooring22} & 0 & 0 \\ 0 & K_{33} + K_{mooring33} & 0 \\ 0 & 0 & K_{44} + K_{mooring44} \end{bmatrix} \quad (5.22)$$

The equivalent damping matrix shows the combined damping coefficients in equation 5.23.

$$C_{eq} =$$

$C_{h22} + c^2(\alpha)C_{tel}$	$s(\alpha)c(\alpha)C_{tel}$	$y_{tip}C_{tel}(-c^2(\alpha)\theta + c(\alpha)s(\alpha)) + z_{tip}C_{tel}(-c^2(\alpha) - c(\alpha)s(\alpha)\theta)$
$s(\alpha)c(\alpha)C_{tel}$	$C_{h33} + s^2(\alpha)C_{tel}$	$y_{tip}C_{tel}(-s(\alpha)c(\alpha)\theta + s^2(\alpha)) + z_{tip}C_{tel}(-s^2(\alpha)\theta - c(\alpha)s(\alpha))$
$y_{tip}C_{tel}(-c^2(\alpha)\theta + c(\alpha)s(\alpha)) + c(\alpha)s(\alpha) + z_{tip}C_{tel}(-c^2(\alpha) - c(\alpha)s(\alpha)\theta)$	$y_{tip}C_{tel}(-s(\alpha)c(\alpha)\theta + s^2(\alpha)) + z_{tip}C_{tel}(-s^2(\alpha)\theta - c(\alpha)s(\alpha))$	$y_{tip}^2C_{tel}(-c(\alpha)s(\alpha)\theta + s^2(\alpha)) + z_{tip}^2C_{tel}(c^2(\alpha) + c(\alpha)s(\alpha)\theta) + z_{tip}y_{tip}C_{tel}(-2c(\alpha)s(\alpha) - s^2(\alpha)\theta + c^2(\alpha)\theta) + C_{h44}$

$$(5.23)$$

Where

$$s(\alpha) = \sin(\alpha(t))$$

$$c(\alpha) = \cos(\alpha(t))$$

The equivalent damping matrix shows that the inclined telescoping damper introduces coupling effect for all degrees of freedom in this model. The impact of the coupling terms are discussed later in this chapter.

To verify the equivalent damping matrix, 2 scenarios are compared with a fixed luffing angle. At first the luffing angle is set to 0 rad (equation 5.24), which means that the telescoping damper is placed horizontally. Secondly the luffing angle is fixed at $\frac{\pi}{2}$ rad (equation 5.25) to model a vertical damper. Both configurations are shown in Figure 5-9.

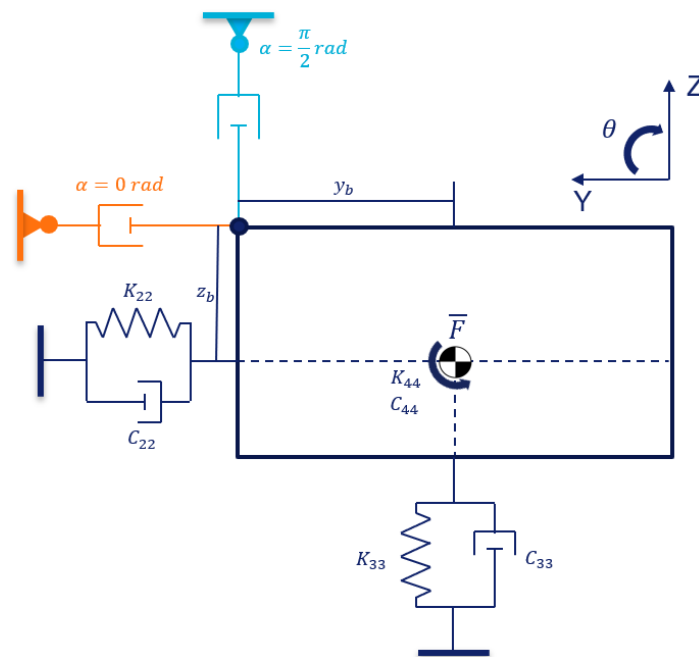


Figure 5-9 Schematic representation of fixed luffing angle ($\alpha = 0$ rad and $\pi/2$ rad).

The damping matrix for a fixed luffing angle of 0 rad shows that the damping in heave of the buoy is uncoupled, but there is coupling between sway and roll introduced by the telescoping damper. This is explained by the fact that the damping force caused by the telescoping damper introduces a force which does not go through the COG of the buoy, and will create a moment with an arm z_{tip} .

$$C_{eq}(\alpha = 0 \text{ rad}) = \begin{bmatrix} C_{h22} + C_{tel} & 0 & -y_{tip}C_{tel}\theta - z_{tip}C_{tel} \\ 0 & C_{h33} & 0 \\ -y_{tip}C_{tel}\theta - z_{tip}C_{tel} & 0 & z_{tip}^2C_{tel} + 2z_{tip}y_{tip}C_{tel}\theta + C_{h44} \end{bmatrix} \quad (5.24)$$

When the damper has a luffing angle of $\frac{\pi}{2}$ rad, the same phenomena occur as mentioned before, but now the coupling is introduced for heave and roll, and sway damping is uncoupled.

$$C_{eq}\left(\alpha = \frac{\pi}{2} \text{ rad}\right) = \begin{bmatrix} C_{h22} & 0 & 0 \\ 0 & C_{h33} + C_{tel} & y_{tip}C_{tel} - z_{tip}C_{tel}\theta \\ 0 & y_{tip}C_{tel} - z_{tip}C_{tel}\theta & y_{tip}^2C_{tel} - 2z_{tip}y_{tip}C_{tel}\theta + C_{h44} \end{bmatrix} \quad (5.25)$$

5.6 Luffing damping matrix

The second degree of freedom for in-plane motion of the gangway is luffing. The same analyses is done for luffing as was done for telescoping. At first the equations of motions are set up from which the damping matrix is derived. With the damping matrix the coupling effects due to luffing are studied. The luffing velocity introduced by a displacement in Y and Z are given by equation 5.26 and 5.27 respectively.

$$v_{luf}(sway) = \sin(\alpha) \dot{Y} \quad (5.26)$$

$$v_{luf}(heave) = \cos(\alpha) \dot{Z} \quad (5.27)$$

The luffing velocity caused by the roll displacement is given by equation 5.11 with the small angle approximation included.

This case results in equations of motion with identical mass and stiffness matrices as was calculated for telescoping, but with a different damping matrix (equation 5.28).

$$C_{eq} =$$

$C_{h22} + s^2(\alpha) \frac{C_{luf}}{L^2}$	$-s(\alpha)c(\alpha) \frac{C_{luf}}{L^2}$	$y_{tip} \frac{C_{luf}}{L^2} (-s(\alpha)c(\alpha) - s^2(\alpha)\theta) + z_{tip} \frac{C_{luf}}{L^2} (s(\alpha)c(\alpha)\theta - s^2(\alpha))$
$-s(\alpha)c(\alpha) \frac{C_{luf}}{L^2}$	$C_{h33} + c^2(\alpha) \frac{C_{luf}}{L^2}$	$y_{tip} \frac{C_{luf}}{L^2} (c(\alpha)s(\alpha)\theta + c^2(\alpha)) + z_{tip} \frac{C_{luf}}{L^2} (c(\alpha)s(\alpha) - c^2(\alpha)\theta)$
$y_{tip} \frac{C_{luf}}{L^2} (-s(\alpha)c(\alpha) - s^2(\alpha)\theta) + z_{tip} \frac{C_{luf}}{L^2} (s(\alpha)c(\alpha)\theta - s^2(\alpha))$	$y_{tip} \frac{C_{luf}}{L^2} (c(\alpha)s(\alpha)\theta + c^2(\alpha)) + z_{tip} \frac{C_{luf}}{L^2} (c(\alpha)s(\alpha) - c^2(\alpha)\theta)$	$y_{tip}^2 \frac{C_{luf}}{L^2} (c^2(\alpha) + c(\alpha)s(\alpha)\theta) + z_{tip}^2 \frac{C_{luf}}{L^2} (s^2(\alpha) - s(\alpha)c(\alpha)\theta) + y_{tip}z_{tip} \frac{C_{luf}}{L^2} (-c^2(\alpha)\theta + 2s(\alpha)c(\alpha) + s^2(\alpha)\theta) + C_{h44}$

$$(5.28)$$

To analyze the matrix, again the luffing angle is set to 0 rad (equation 5.29) and to $\frac{\pi}{2}$ rad (equation 5.30) and the damping matrices are analyzed.

Due to the fact that the rotational luffing damper results in forces perpendicular to the gangway the coupling effects of luffing and telescoping are opposite. For a luffing angle of 0 rad, the coupling between heave and roll are present due to the fact that the luffing damper acts as a vertical force when the luffing angle is 0, which is visible in equation 5.29.

$$C_{eq}(\alpha = 0) \begin{bmatrix} C_{h22} & 0 & 0 \\ 0 & C_{h33} + \frac{C_{luf}}{L^2} & y_{tip} \frac{C_{luf}}{L^2} - z_{tip} \frac{C_{luf}}{L^2} \theta \\ 0 & y_{tip} \frac{C_{luf}}{L^2} - z_{tip} \frac{C_{luf}}{L^2} \theta & y_{tip}^2 \frac{C_{luf}}{L^2} + y_{tip} z_{tip} \frac{C_{luf}}{L^2} \theta + C_{h44} \end{bmatrix} \quad (5.29)$$

The opposite occurs when the luffing angle is set to $\frac{\pi}{2}$ rad, where the force is horizontal and coupling occurs between sway and roll which can be seen from equation 5.30.

$$C_{eq}(\alpha = \frac{\pi}{2}) \begin{bmatrix} C_{h22} + \frac{C_{luf}}{L^2} & 0 & -y_{tip} \frac{C_{luf}}{L^2} \theta - z_{tip} \frac{C_{luf}}{L^2} \\ 0 & C_{h33} & 0 \\ -y_{tip} \frac{C_{luf}}{L^2} \theta - z_{tip} \frac{C_{luf}}{L^2} & 0 & z_{tip}^2 \frac{C_{luf}}{L^2} + y_{tip} z_{tip} \frac{C_{luf}}{L^2} \theta + C_{h44} \end{bmatrix} \quad (5.30)$$

5.7 Sensitivity study telescoping force

The parameters of the damping matrices are studied by varying the parameters and analyzing the effect of the variable parameter on the total damping force, first for luffing and secondly for telescoping.

The damping matrix for luffing consists of 3 variable parameters; $\alpha(t)$, C_{tel} and C_h . The luffing angle and telescoping damping are parameters inherent to the Ampelmann system and the motions of the buoy. The luffing angle can slightly be changed by placing the Ampelmann system elevated. The telescoping damping coefficient of the gangway cannot be changed at will, but the value, determined by the full-scale tests, does fluctuate. The hydrodynamic damping coefficient of the buoy is frequency dependent, so this value differs significantly with different environmental conditions. To see what the effect of these variable parameters are, the damping force in y- and z-direction and the damping moment in roll are calculated with varying one of these parameters at a time.

The other parameters included in the damping force calculations are the velocities in sway, heave and roll. These velocities are kept constant to solely study the effect of the Ampelmann parameters and the varying hydrodynamic damping coefficients on the damping force. The last parameter which is included in the damping matrices is the roll angle, which in this case is also kept constant. The values of the velocities are chosen to be equal for sway and heave. The roll angle and roll velocity are the average values of a simulation in aNySIM with incoming regular waves with the most common sea state ($A= 0.75\text{m}$, $T = 4.5\text{s}$). When one parameter varies, the others are kept constant at the average values calculated in the simulation done for the most common sea state. The values of all parameters for the case study are shown in Table 5-2.

Table 5-2. Parameters case study.

Constant parameters		Varying parameters	
v_y [m/s]	1	α [rad]	0,2
v_z [m/s]	1	$C_{tel} \frac{Ns}{m}$	9854
$\dot{\theta}$ [rad/s]	0,15	$C_{22} \frac{Ns}{m}$	175.000
θ [rad]	0,1	$C_{33} \frac{Ns}{m}$	140.000
		$C_{44} \frac{Nms}{rad}$	430.000

5.7.1 Luffing angle

In the first case, the effect of the luffing angle on the total damping forces and moment are studied. The maximum allowable luffing angle is 0.3 rad for the Ampelmann system to be operational (Ampelmann Operations B.V., 2014). The luffing angle therefor varies between 0 and 0.3 rad.

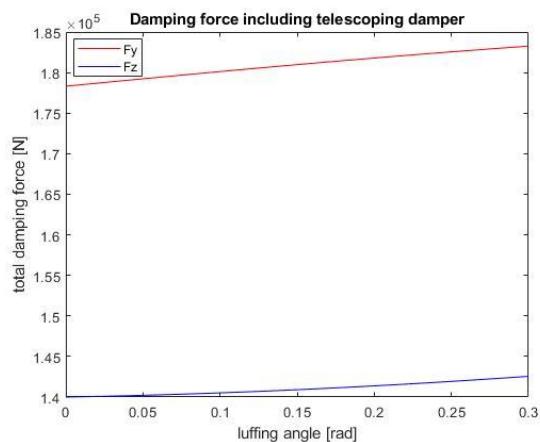


Figure 5-10 Damping force varying luffing angle.

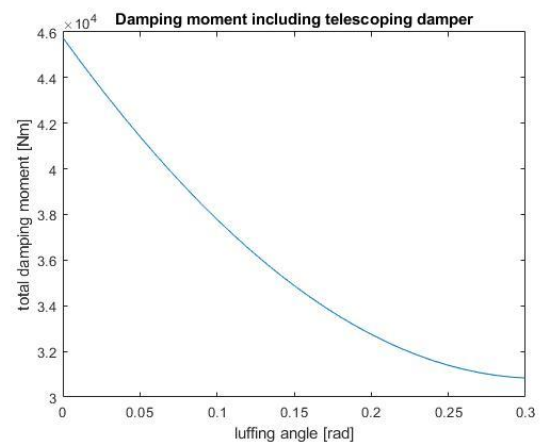


Figure 5-11 Damping moment varying luffing angle.

Due to the trigonometric functions in the damping matrix, Figure 5-10 shows that the damping forces and moments respond non-linearly. The damping forces are less non-linear compared to the damping moment (Figure 5-11) since the trigonometric functions in equation 5.23, for the damping forces are first-order, and in equation 5.23 the damping moment are first- and second-order. The force in y-direction increases faster than the force in z-direction with increasing luffing angle. This can be concluded from matrix 5.24 and 5.25 where the luffing angle is set to 0 rad and $\frac{\pi}{2}$ rad. When the luffing angle is set to 0 rad, there is only coupling between roll and sway. So for small angles the telescoping damper will exert a higher force in y-direction compared to in z-direction. When analyzing the damping moment it can be seen that the damping moment is decreasing. For small angles the coupling between sway and roll creates a moment in opposite direction of the hydrodynamic roll damping moment. When the luffing angle increases the coupling between heave and roll becomes more significant, which creates a positive damping moment that reduces the slope of the damping moment. The effect of the varying luffing angle in this case is not changing the damping forces significantly. The increase of damping force in y-direction, at maximum luffing angle, is 2.8% compared to a luffing angle of 0 rad. The damping moment is changing significantly with a 33% decrease compared the damping moment with a luffing angle of 0 rad. This is for this case study where the velocities in sway and heave are positive and much higher than the roll velocity. This results in a larger influence of the coupling on the changing moment by the forces than the other way around, which will not always be the case.

5.7.2 Telescoping damping coefficient

In this case the luffing angle is set to 0.2 rad and the telescoping damping coefficient varies. The damping coefficient is not manually adjustable but the value may differ in actual operation, compared to the tests. Studying the effect of the damping coefficient on the total damping forces and moment, C_{tel} varies from 0 to 5 times the damping coefficient from the Ampelmann tests.

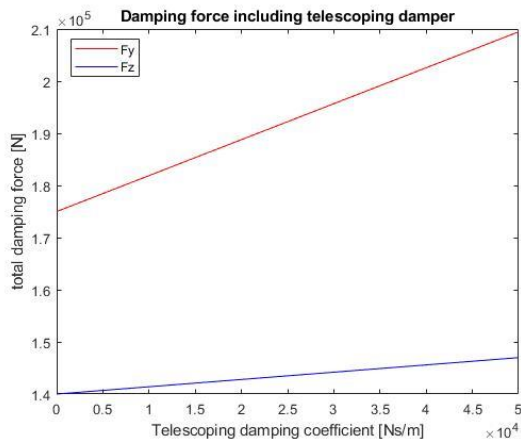


Figure 5-12 Damping force varying telescoping damping coefficient.

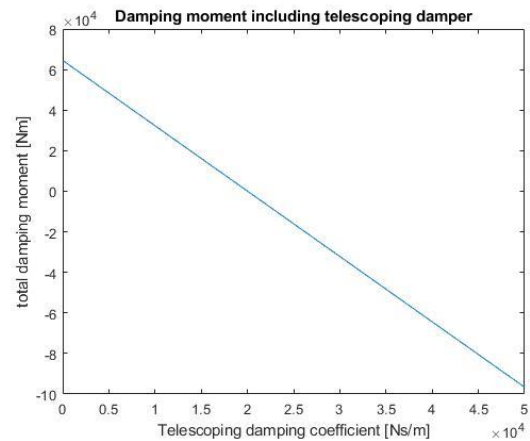


Figure 5-13 Damping moment varying telescoping damping coefficient.

Even though it is unlikely that the telescoping damping coefficient is miscalculated by Ampelmann with a factor of 5, this case is used to study the effect of a varying telescoping damping coefficient. Having a fixed luffing angle takes out all the trigonometric functions in the damping matrix force which will result in a linear damping matrix. Figure 5-12 shows that the damping forces in y- and z-direction increase linearly but with a different slope. Due to the projection of the telescoping force in y- and z-direction with a relatively small angle, it can be said that the damping force in y-direction on the buoy experiences larger effect than the damping force in z-direction. The damping moment decreases with an increasing telescoping damping coefficient (Figure 5-13). This shows that the telescoping forces create an opposite moment compared to the hydrodynamical moment.

5.7.3 Hydrodynamic damping coefficient

The last variable parameter which is studied, is the hydrodynamical damping of the buoy. The hydrodynamic damping is frequency dependent and can differ significantly with different environmental conditions. The hydrodynamic damping for sway, heave and roll are varied from 0 up to the maximum hydrodynamic damping derived from the diffraction software for each degree of freedom. The results are shown Figure 5-14, Figure 5-15 and Figure 5-16. Due to the big difference in hydrodynamic damping coefficients, the total damping forces and moment vary significantly.

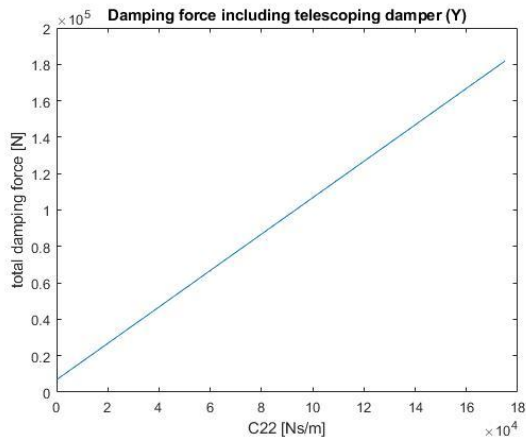


Figure 5-14 Damping force with varying hydrodynamic damping in sway.

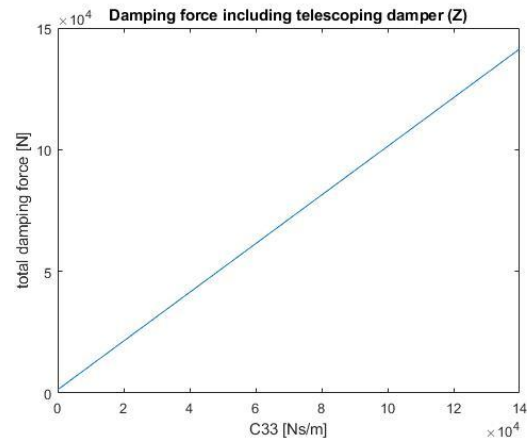


Figure 5-15 Damping force with varying hydrodynamic damping in heave.

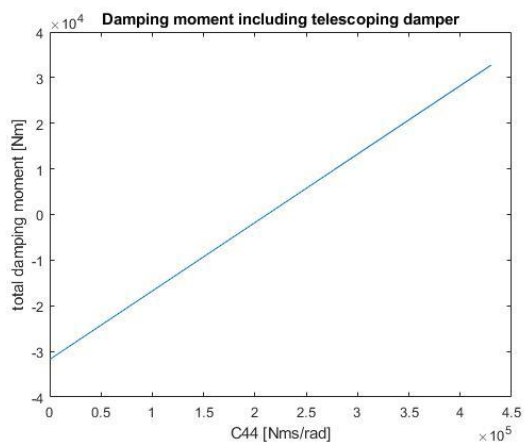


Figure 5-16 Damping moment with varying hydrodynamic damping in roll

5.8 Sensitivity study luffing force

To study the effect of the varying parameters on the damping force and moment, the same approach is used as in chapter 5.7. The luffing force introduces one more variable parameter which is the gangway length.

5.8.1 Luffing angle

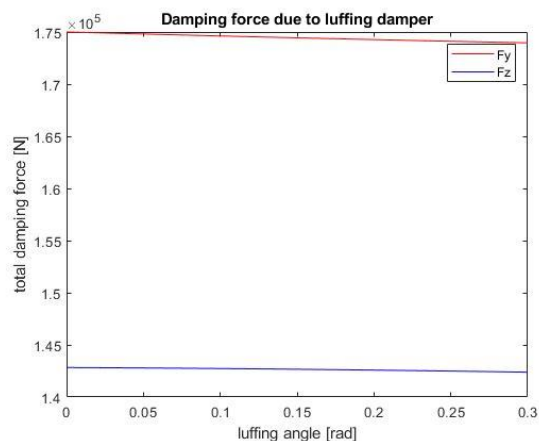


Figure 5-17 Damping force varying luffing angle.

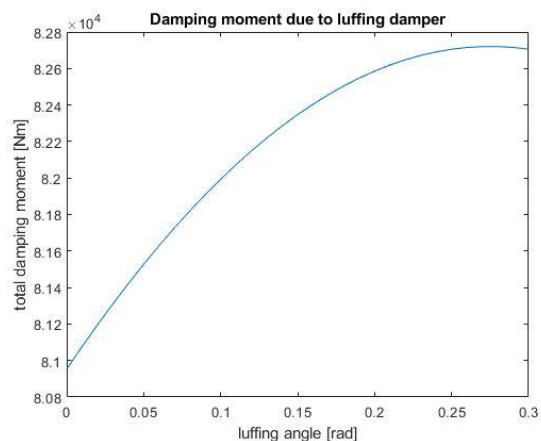


Figure 5-18 Damping moment varying luffing angle.

The damping forces in y- and z-direction are close to linear for the working range of the luffing angles of the gangway. Figure 5-17 and Figure 5-18 show that the luffing angle does not influence the total damping force or damping moment significantly. The maximum deviation for the damping moment is about 2% of the initial value.

5.8.2 Luffing damping coefficient

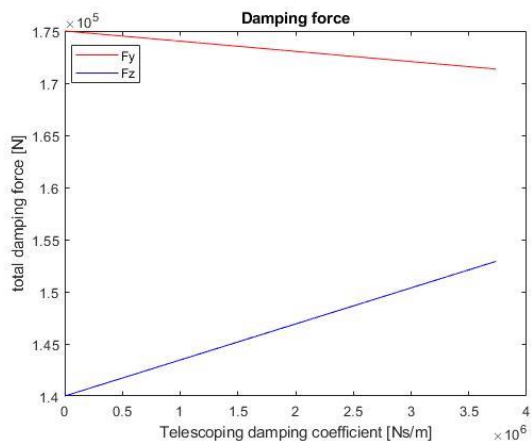


Figure 5-19 Damping forces luffing damping coefficient.

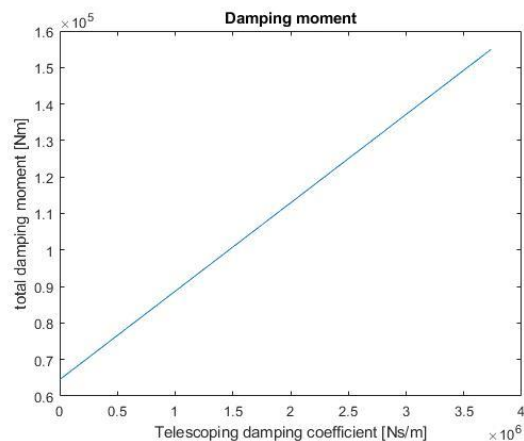


Figure 5-20 Damping moment luffing damping coefficient.

For a fixed luffing angle of 0.2 rad with a varying luffing damping coefficient it can be seen Figure 5-19 that an increasing luffing damping coefficient, creates an increasing damping force in z-direction and a decreasing damping force in y-direction. This results that both forces either work with or against a positive roll motion. In this case they both increase the total damping moment as can be seen from Figure 5-20. The telescoping damping coefficient can be of big influence for the roll moment but realistically the value will not vary that much.

5.8.3 Hydrodynamic damping coefficient

Figure 5-21, Figure 5-22, and Figure 5-23 show the effect of varying hydrodynamical damping coefficients on the total damping forces and moment for each degree of freedom. Also for luffing the hydrodynamic damping coefficient is significant for the total damping forces and moment acting on the buoy.

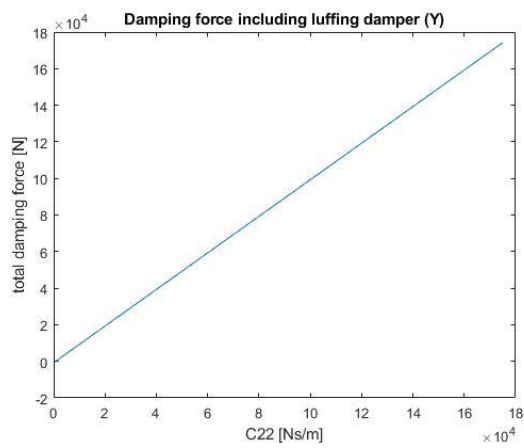


Figure 5-21 Damping force varying hydrodynamic damping coefficient for sway.

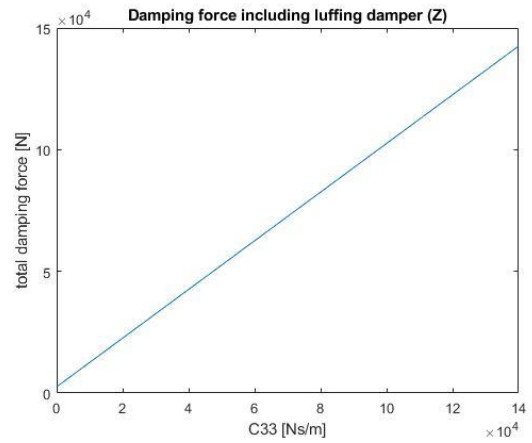


Figure 5-22 Damping force varying hydrodynamic damping coefficient for heave.

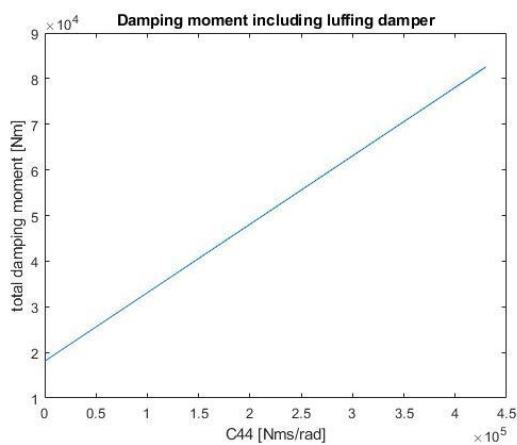


Figure 5-23 Damping moment varying hydrodynamic damping coefficient for roll.

5.8.4 Gangway length

The gangway length is a new parameter in the sensitivity study compared to the telescoping damper. The gangway length can vary within its operational limits (Ampelmann Operations B.V., 2014). The effect of the gangway length in workably range, on the damping forces and moment, is plotted in Figure 5-24 and Figure 5-25.

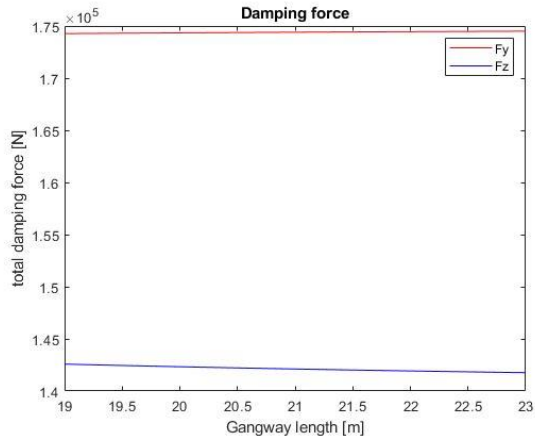


Figure 5-24 Damping force varying gangway length.

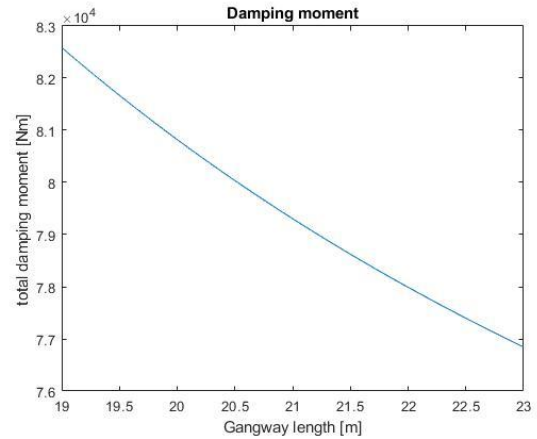


Figure 5-25 Damping moment varying gangway length.

The varying length of the gangway does not affect the damping forces in y- and z-direction significantly. The effect of the varying gangway length does affect the damping moment. With an increasing gangway length it is shown that the gangway moment decreases non-linearly caused by the second order equation of the luffing force (equation 4.14 and 4.15).

5.9 Solving equations of motion

To study the effect of the damping force on the response of the buoy, the equations of motion are solved using an ordinary differential equation (ODE) solver written in Python. The equations of motion are solved for a case study with limited hydrodynamical damping to study the effect of the gangway damping on the response of the buoy. The response of the buoy calculated by the ODE solver is compared with the same case study performed in aNySIM. At first the method of building the ODE solver is explained and after the results are discussed.

5.9.1 Case study

Following from the sensitivity study, the hydrodynamical damping of the buoy is a governing factor regarding the total damping forces and moment acting on the buoy. From the diffraction data of the buoy (Figure 5-26), it shows that for low- and high-frequency waves the hydrodynamic damping coefficient is relatively small, which makes the damping forces, caused by the gangway, more significant.

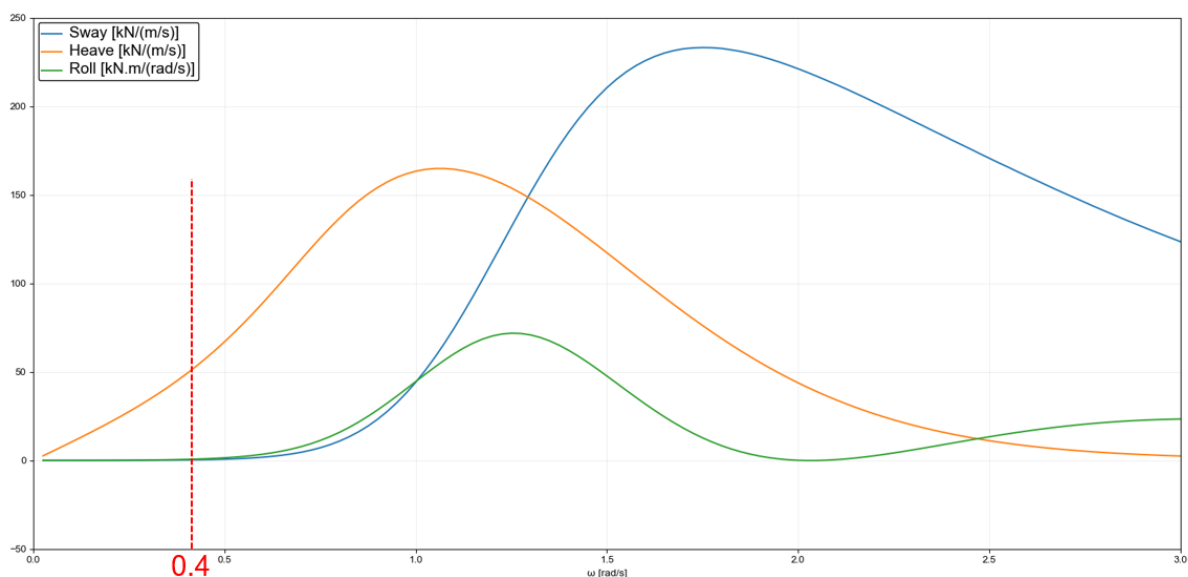


Figure 5-26 Frequency dependent damping coefficients for sway, heave and roll.

To verify this, a case study is used in this chapter with regular, unidirectional, low-frequency waves coming from y-direction (Figure 4-6). The amplitude of the regular waves are chosen to be 1.5m, to exert significant buoy motions. The period of the waves are set to 15s to have sufficiently low hydrodynamical damping. This case is purely set up to study the effect of the gangway damping on the response of the buoy, since it is expected that for these wave conditions the dynamic interaction plays a significant role.

5.9.2 ODE solver

An ODE solver is used to solve equation 5.4. To be able to solve equation 5.4 with the ODE solver, the second order differential equation is reduced to a first order differential equation. At first the equations of motion is in equation 5.31.

$$\ddot{X} = (-C_{eq}\dot{X} - K_{eq}X + F_{waves})M_{eq}^{-1} \quad (5.31)$$

Equation 5.31 is reduced to a first order differential equation by changing the notation of the motions of the body (Chris Keijdener, 2017). Implementing vectors 5.32 and 5.33 in equation 5.31 results in the first order differential equation 5.34.

$$q = \begin{bmatrix} y \\ z \\ \theta \\ \dot{y} \\ \dot{z} \\ \dot{\theta} \end{bmatrix} \quad (5.32) \quad \dot{q} = \begin{bmatrix} \dot{y} \\ \dot{z} \\ \dot{\theta} \\ \ddot{y} \\ \ddot{z} \\ \ddot{\theta} \end{bmatrix} \quad (5.33)$$

$$\dot{q} = (P q + F_{waves})M_{eq}^{-1} \quad (5.34)$$

With

$$P = \begin{bmatrix} 0 & 0 & 0 & 1 & 0 & 0 \\ 0 & 0 & 0 & 0 & 1 & 0 \\ 0 & 0 & 0 & 0 & 0 & 0 \\ -K_{22} & 0 & 0 & -C_{22} & -C_{23} & -C_{24} \\ 0 & -K_{33} & 0 & -C_{32} & -C_{33} & -C_{34} \\ 0 & 0 & -K_{44} & -C_{42} & -C_{43} & -C_{44} \end{bmatrix} \quad (5.35)$$

And

$$F_{waves} = \begin{bmatrix} F_y \sin(\omega t + \phi_y) \\ F_z \sin(\omega t + \phi_z) \\ M_\theta \sin(\omega t + \phi_\theta) \end{bmatrix} \quad (5.36)$$

For solving the first order differential equation, the initial conditions are required. In the case study, the buoy will start at its equilibrium with no initial velocity or displacement, which results in the following initial conditions.

$$q_{t0} = \begin{bmatrix} 0 \\ 0 \\ 0 \\ 0 \\ 0 \\ 0 \end{bmatrix}$$

The values of the hydrostatic stiffness, hydrodynamic damping, added mass, wave forces and phase shifts are found with the results of the diffraction software (Appendix 9.3). The damping coefficients of the gangway are shown in equations 5.23 and 5.28. All the components of the first order differential equation are now known and can be solved using Python. The ODE solver solves equation 5.31 numerically for a given timespan and timestep. To compare the results of this approach with the results from the aNySIM model, a simulation is performed with a duration of 300s and a timestep of 0.1s. In programming, the state vector q is calculated for every timestep by equation 5.37 (Chris Keijndener, 2017).

$$q_{n+1} \approx q_n + \Delta_t \dot{q}_n \quad (5.37)$$

The damping matrices contain time-dependent components such as luffing angle and gangway length. These components are dependent on the y- and z-location, and the roll position of the buoy. In the ODE solver, the damping matrix is recalculated for every timestep, which is also done in aNySIM. The ODE-solver function from Python solves equation 5.31 for every timestep, which computes time-series of the displacement and velocity of all 3 degrees of freedom of the buoy. The complete code of solving the first order differential equation is given in Appendix 9.7.

5.9.3 Comparing aNySIM and Python model

To discuss the results of the aNySIM and Python model, at first the differences of both models are analyzed. Even though the model in aNySIM is linearized as much as possible, some non-linear effects occur. At first the mooring lines are tested on static linearity that is discussed in chapter 4.4.1. Dynamically the mooring lines may not act linearly. Especially in the case with long waves, the sway response has a high amplitude that changes the geometry of the mooring lines. When the buoy is at its maximum sway excitation, it can be seen (Figure 5-27) that the mooring line configuration is non-symmetric. Figure 5-27 shows that at the maximum sway excitation of the buoy, the mooring lines have different angles with respect to the buoy. This results in a non-linear coupling effect of the stiffness of the mooring lines in heave caused by the sway motion of the buoy.

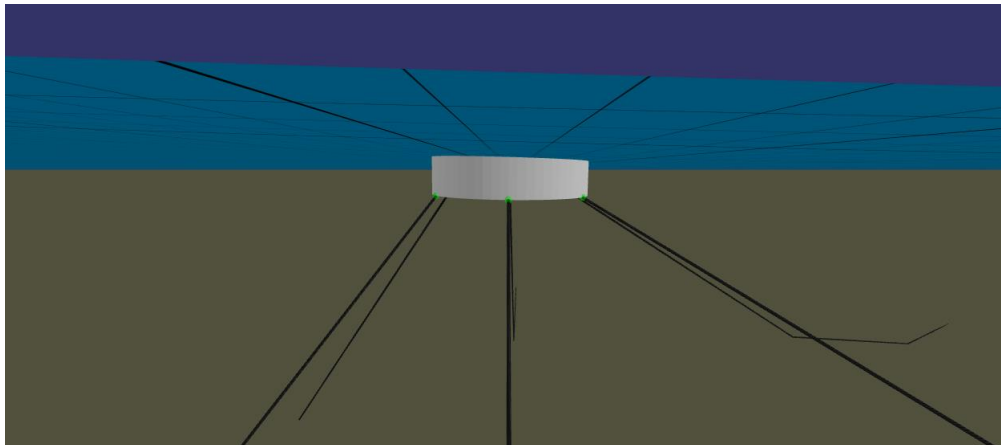


Figure 5-27 Mooring configuration at maximum sway position of the buoy.

This non-linear effect becomes visible plotting the total force of all 6 mooring lines combined in y-direction and in z-direction (Figure 5-28). Figure 5-28 shows the total mooring force acting on the buoy in y-direction (blue line) and z-direction (orange line) for the wave conditions set up in the case study. It shows that the total mooring force acting on the buoy respond non-linearly in aNySIM. This has not been taken into account in the Python model, where the stiffness in all degrees of freedom of the system is assumed to be perfectly linear.

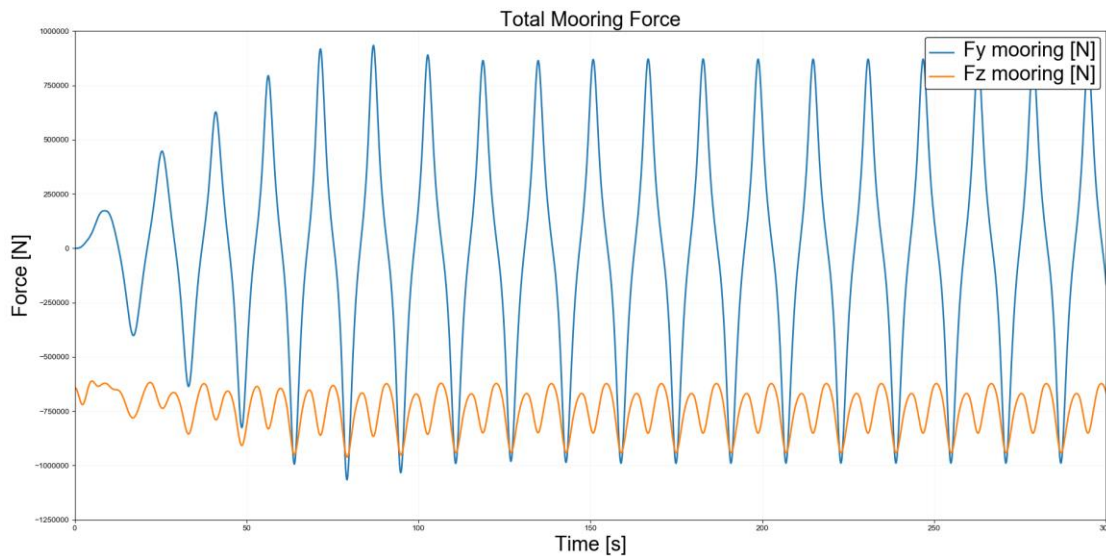


Figure 5-28 Total mooring forces acting on the buoy.

The second difference of the aNySIM model compared to the Python model is the incoming waves. In aNySIM regular incoming waves are modeled with an amplitude of 1.5m and a period of 15s. From a spectrum analysis in aNySIM, which is shown in Figure 5-29, it is concluded that the incoming waves are not a perfectly regular waves with 1 frequency, but the frequency of the incoming waves has a spreading.

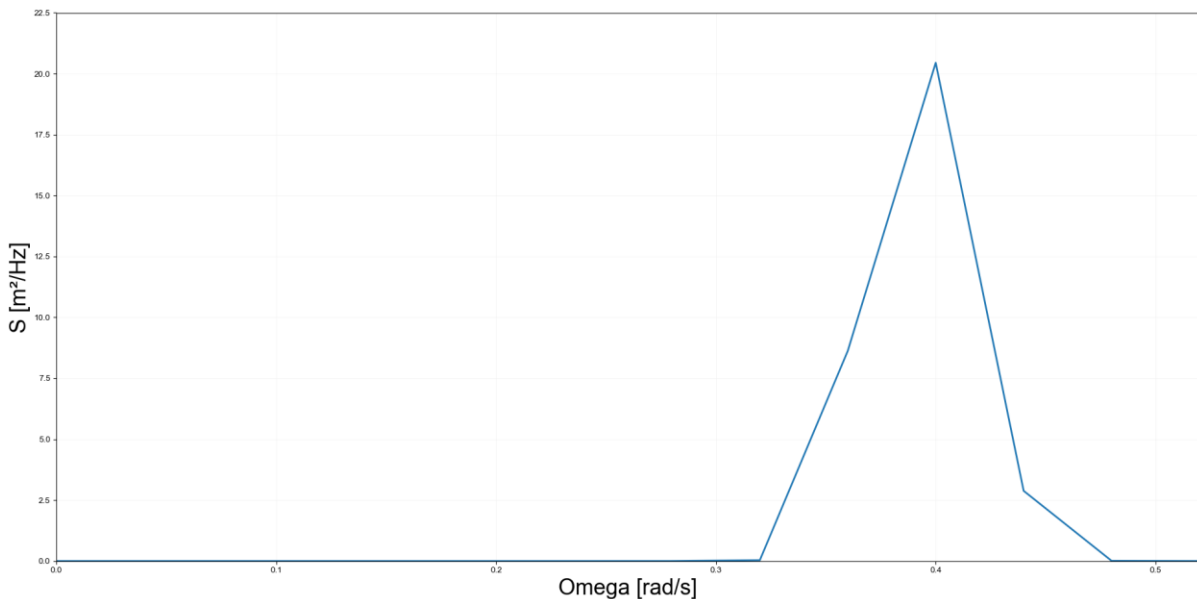


Figure 5-29 Spectrum Analyses Incoming waves.

The variety of the frequency of the incoming wave does influence the added mass and hydrodynamic damping of the buoy, since these values are frequency dependent. Again, in Python it is assumed that the incoming wave force is perfectly sinusoidal with a fixed amplitude, period and phase (equation 5.36).

To compare the numerical aNySIM model with the numerical model from Python, the sway and heave response of the buoy without the Ampelmann system are plotted in Figure 5-30 and Figure 5-31 respectively. According to simulations from both models, the roll response of the buoy, caused by long

waves, is small enough to be neglected. The maximum roll excitation in these simulations is 0.04 rad, which is shown in Appendix 9.5.

At first the sway response is analyzed. The response of the buoy computed by aNySIM and Python (Figure 5-30) shows 2 main differences; The amplitude in the first 100s of the simulation and the phase of both models.

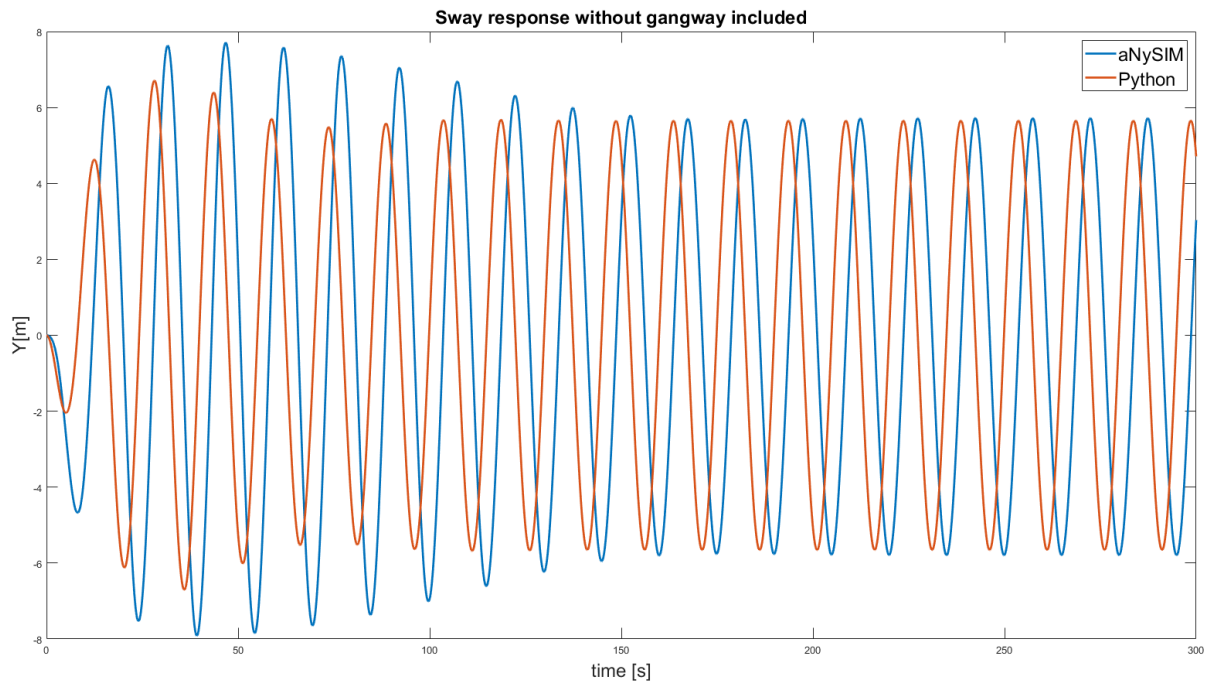


Figure 5-30 Sway response without gangway included by aNySIM and Python.

Since the frequency dependent damping coefficient in aNySIM varies, the damping coefficient implemented in the Python model is not identical to the damping coefficient in aNySIM. The damping coefficient plays a significant role in the phase angle of a system. This can be explained by a varying damping coefficient with respect to the values of the mass, added mass and stiffness. The phase angle of a system is calculated by rewriting the transfer function of the system (Karl Johan Aström, 2003). Equation 5.38 shows the Laplace transformation of equation 5.4, which is used to write the transfer function for one degree of freedom in equation 5.39.

$$(M + A)s^2X(s) + CsX(s) + KX(s) = F_{waves}(s) \quad (5.38)$$

$$H(s) = \frac{X(s)}{F(s)} = \frac{1}{(M+A)s^2 + Cs + K} \quad (5.39)$$

The transfer function is converted to the frequency domain by implementing $s = j\omega$

$$H(j\omega) = \frac{X(j\omega)}{F(j\omega)} = \frac{1}{-(M+A)\omega^2 + Cj\omega + K} \quad (5.40)$$

Using the transfer function, the phase angle is calculated by equation 5.41.

$$\angle H(j\omega) = \arctan\left(\frac{\text{Im } H(j\omega)}{\text{Re } H(j\omega)}\right) \quad (5.41)$$

Implementing equation 5.40 in equation 5.41, leads to equation 5.42 for the phase angle.

$$\angle H(j\omega) = \arctan\left(\frac{-C\omega}{-(M+A)\omega^2 + K}\right) \quad (5.42)$$

Equation 5.42 shows that a varying value for damping and added mass, affects the phase angle. The phase shift and different response in the first 100 seconds of both model can be explained by the non-linearities in damping and/or added mass of the aNySIM model compared to the Python model.

Analyzing the heave response computed by the aNySIM model and the Python model also shows differences between results of the 2 models (Figure 5-31).

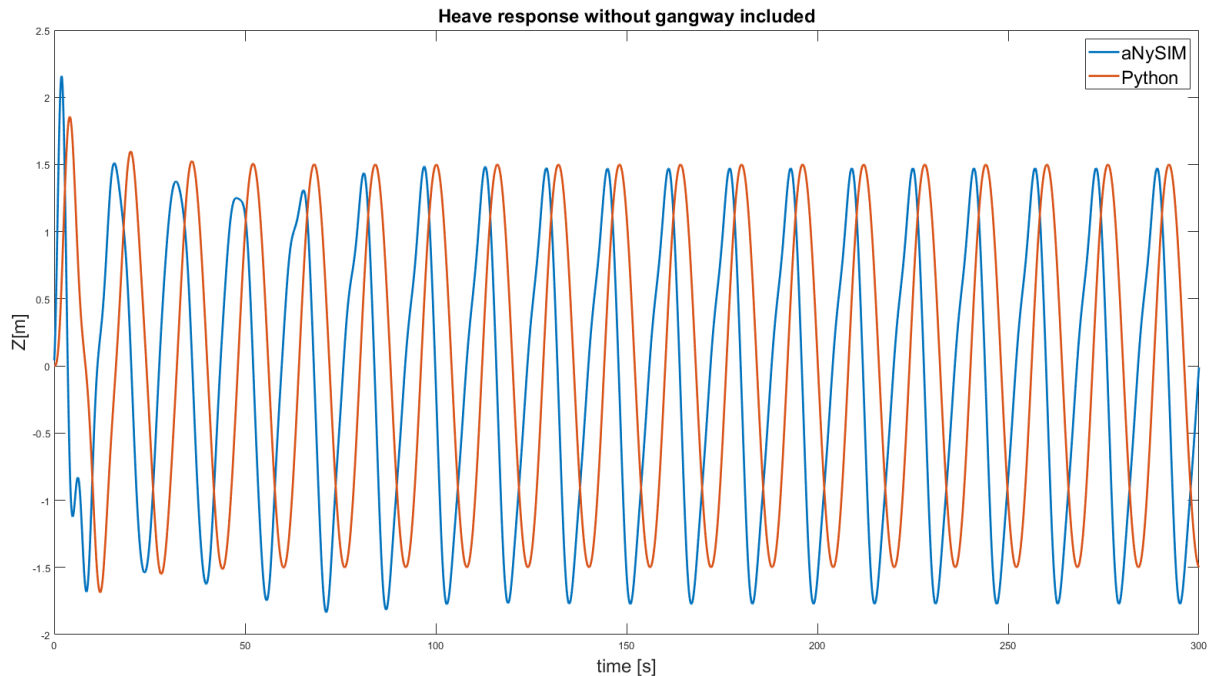


Figure 5-31 Undamped sway response by aNySIM and Python.

The heave response of both models oscillates around a different equilibrium. The average draft of the aNySIM model is lower than the average draft of the Python model. This can be explained by the fact that the pretension of the mooring lines is not included in the Python model but this is included in the aNySIM model. The non-linear effect of the mooring lines is also visible in the heave response of aNySIM. Figure 5-31 shows that the heave motion computed by aNySIM is not a perfect sinusoidal motion while the heave response from the Python model is.

5.10 Dynamic vs kinematic approach

Even though the responses of the aNySIM model and Python model are not identical, it can be determined that the excitations of the sway and heave motion of the buoy in both models are very similar. Using both models, the effect of the damping forces of the gangway on the motions of the buoy are studied. Figure 5-32 and Figure 5-33 show the sway response computed by aNySIM and Python respectively with (blue line) and without (orange line) dynamic interaction included. It shows that the amplitude of the sway excitation is reduced by the gangway damper for both the aNySIM and Python model up to 9,5%. Besides the reduced amplitude for the sway motion, a small phase shift is visible in Figure 5-32 and Figure 5-33. This can be explained by the damping coefficients of the gangway and equation 5.42.

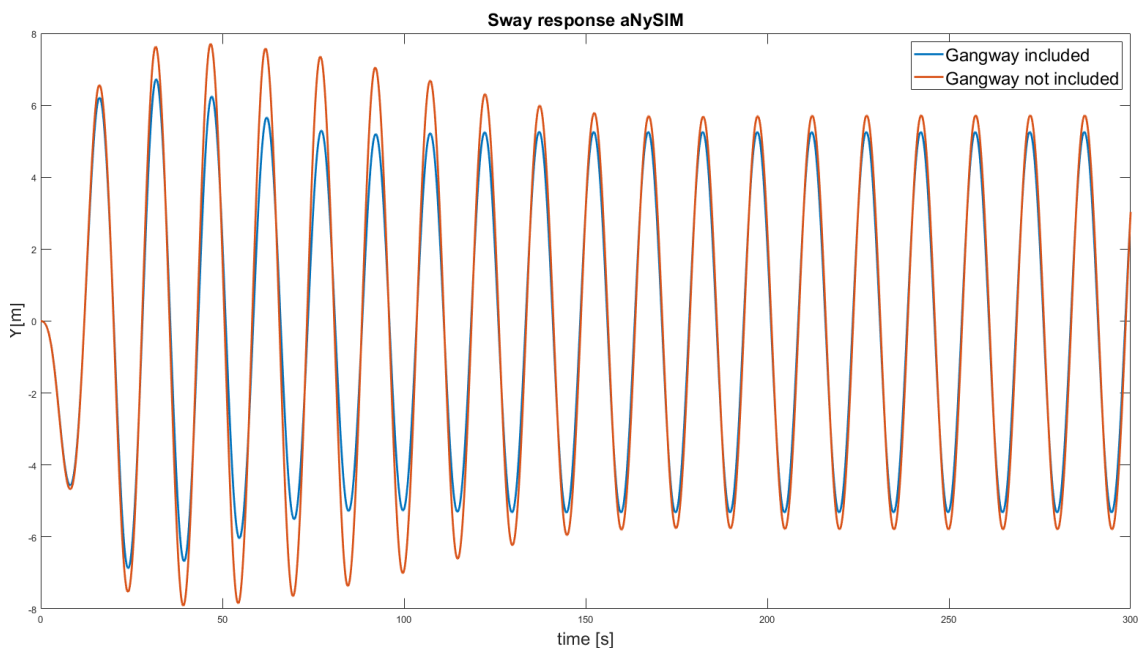


Figure 5-32 Sway response computed by aNySIM.

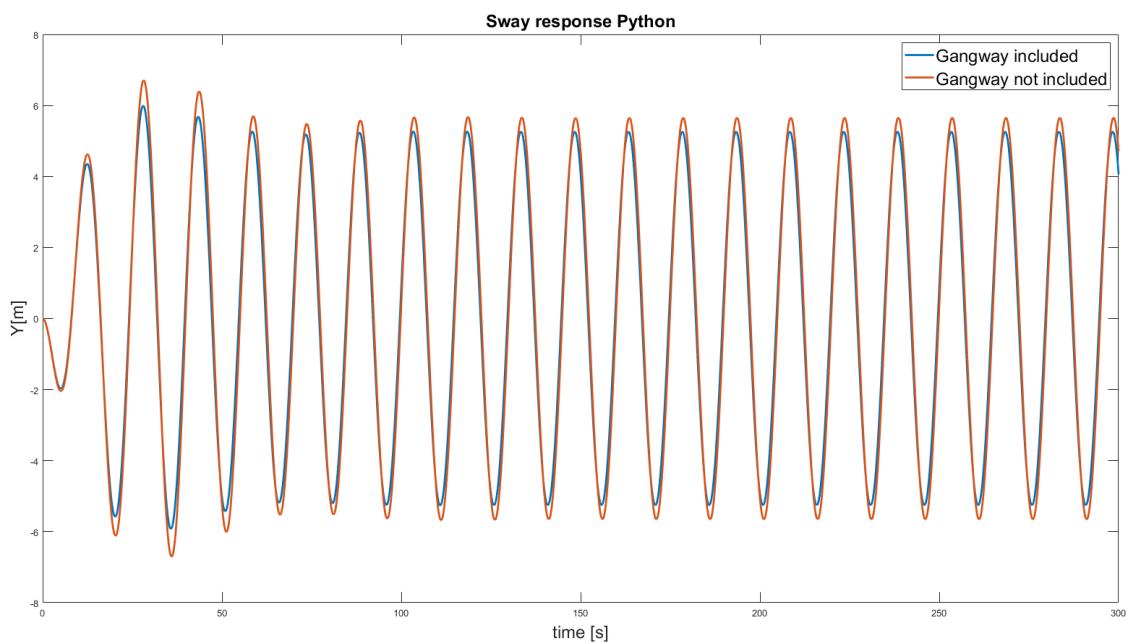


Figure 5-33 Sway response computed by Python.

Figure 5-34 and Figure 5-35 shows that the amplitude of the heave response for both models is reduced, by the added damping of the gangway, up to 10%. The phase shift is less relevant for the heave response due to the fact that the values of the added mass and stiffness coefficients are much higher for the heave motion than for the sway motion. Due to this, the effect of a changing damping coefficient is relatively small. The non-linearities of the mooring lines in aNySIM are visible in Figure 5-34 where the heave response is not perfectly sinusoidal. Due to the linearized mooring stiffness in the Python model the heave response in Figure 5-35 is perfectly sinusoidal.

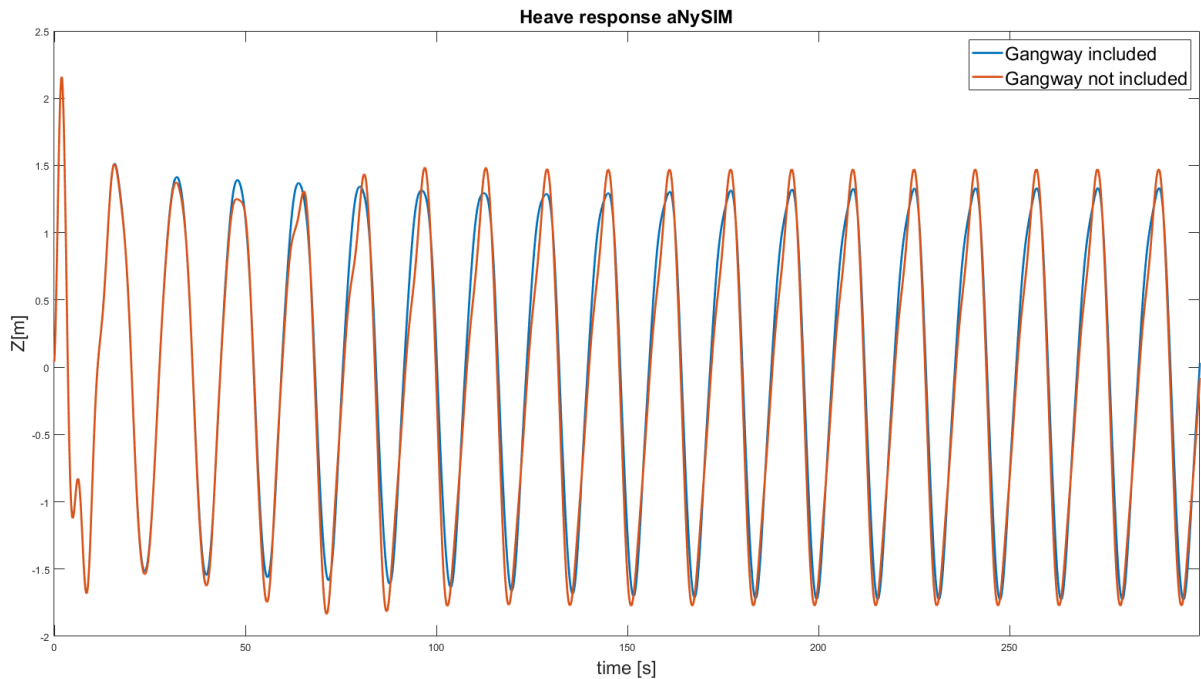


Figure 5-34 Heave response computed by aNySIM.

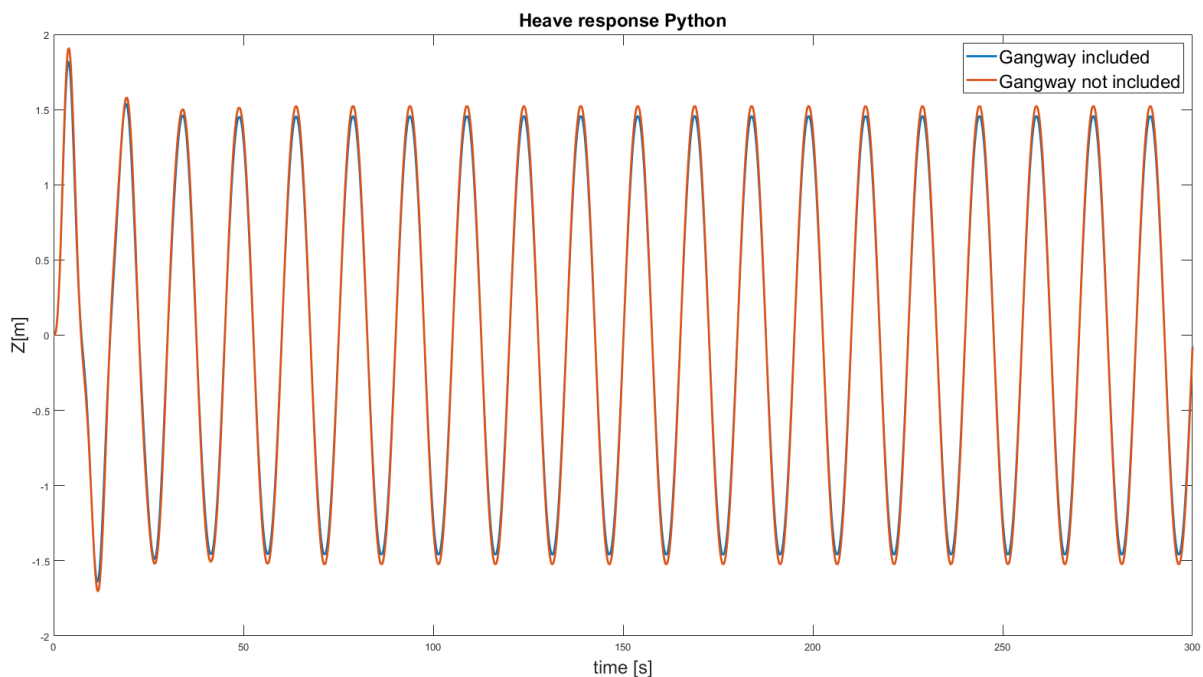


Figure 5-35 Heave response computed by Python.

5.11 Conclusion

An analytical approach is used to set up the equations of motion of the CALM buoy in the y-z plane. The CALM buoy is modeled as a mass-spring-damper system with 3 degrees of freedom, where the hydrodynamic and hydrostatic properties of the buoy have been replaced by equivalent springs and dampers. Via the equations of motion, the equivalent damping matrix shows that the equivalent damping coefficients depend on the hydrodynamic damping coefficients, gangway damping coefficients, luffing angle, gangway length and roll angle. Via a sensitivity study it became clear that the hydrodynamic damping coefficient is the governing factor in the equivalent damping matrix. For low- and high-frequency waves the hydrodynamic damping coefficients of the buoy are minimal and in these frequency regions, the gangway damping coefficients is more relevant. To test this, a case study is used with relatively low hydrodynamical damping. The equations of motion, derived by the analytical approach, are used to verify the results of the aNySIM model by solving them with an ODE solver in python. The amplitude of the sway and heave motion are very similar in both models. The main difference between the aNySIM model and the Python model are the non-linear effects which do occur in aNySIM but not in Python. Large sway excitations of the buoy causes a non-symmetrical mooring configuration that responds differently compared to the linearized mooring stiffness used in Python. The sway and heave responses of both models have a phase difference that may be caused by the difference in damping coefficients in both models. Again in Python these coefficients are linearized to a constant value and in aNySIM the regular incoming wave does have a variance in frequency, which causes a variation in added mass and hydrodynamic coefficients of the buoy. Using the case study the influence of the gangway forces acting on the buoy is studied. Both models show that for low hydrodynamic damping, the gangway forces reduces the amplitude of the buoy motion in sway and heave up to 10% for this case study.

6. Workability study

6.1 Introduction

In this chapter a workability study is performed, comparing the workability of the Ampelmann system with and without dynamic interaction included in the model. The workability study determines what percentage of time the Ampelmann can be operational. To perform a complete workability study the gangway forces and motions of the buoy are analyzed in 3d. Using wave spectrum data, the workability study is performed by running time-domain simulations for all sea states. A MATLAB tool is used to calculate the workability based on the operational limits of the gangway that are defined by Ampelmann. The results of the workability derived by a kinematic approach are compared with the workability derived by a dynamic approach.

6.2 3D configuration

To perform a workability study the in-plane model is extended to a 3d model with incoming head waves with respect to the host vessel which is shown in figure Figure 6-1.

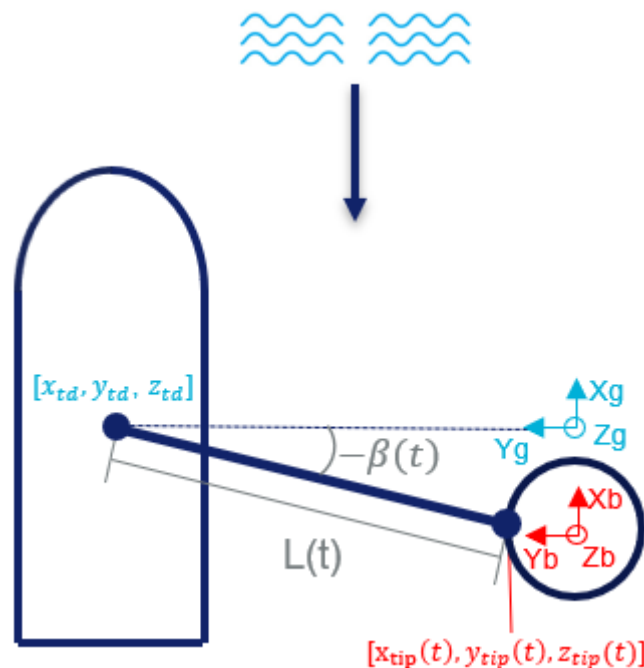


Figure 6-1 Schematic representation of positioning host vessel.

Two important additions are implemented in the aNySIM model to do a 3d analyses. At first the third degree of freedom of the gangway is added; slewing. Slewing means that the gangway rotates around its z-axis at the rotation point of the transferdeck. The second addition for the aNySIM model is that all forces are now dependent of 3 dimensional velocities of the connection point of the buoy, and of the 3 dimensional length of the gangway.

6.2.1 Global velocities

Calculating the damping forces of the gangway in 3d it is required to transform the body-fixed velocities, which are an output of aNySIM, to the global coordinate system. This is done by applying rotation matrices.

Rotating around one specific axis results in an elemental rotation matrix. For the buoy this means that the elemental rotation matrices for roll (rotation around local x-axis), pitch (rotation around local y-axis) and yaw (rotation around local z-axis) are respectively

$$R_x = \begin{bmatrix} 1 & 0 & 0 \\ 0 & \cos(\phi) & -\sin(\phi) \\ 0 & \sin(\phi) & \cos(\phi) \end{bmatrix} \quad (6.1)$$

$$R_y = \begin{bmatrix} \cos(\theta) & 0 & \sin(\theta) \\ 0 & 1 & 0 \\ -\sin(\theta) & 0 & \cos(\theta) \end{bmatrix} \quad (6.2)$$

$$R_z = \begin{bmatrix} \cos(\psi) & -\sin(\psi) & 0 \\ \sin(\psi) & \cos(\psi) & 0 \\ 0 & 0 & 1 \end{bmatrix} \quad (6.3)$$

The combined rotation matrix rotates the body fixed velocity vectors to the global coordinate system. This rotation matrix is formed by multiplying the elemental rotation matrices. A rotational matrix can transform the local coordinate system to the global coordinate system (active transformation), but it can also be used to transform the global coordinate system to the local coordinate system (passive transformation). The difference between the active and passive rotation matrix is the order of multiplying the elementary rotation matrices. Equation 6.4 is used to form the rotation matrix for active transformation.

$$R_{l \rightarrow g} = R_z R_y R_x \quad (6.4)$$

The global velocities of the buoy at the connection point of the buoy are calculated by multiplying the local velocities with the rotation matrix.

$$v_g = R_{l \rightarrow g} v_b \quad (6.5)$$

With

$$v_g = \begin{bmatrix} v_{gx} \\ v_{gy} \\ v_{gz} \end{bmatrix}, v_b = \begin{bmatrix} v_{bx} \\ v_{by} \\ v_{bz} \end{bmatrix}$$

6.2.2 Telescoping force

The length of the gangway in 3d is dependent on the $x_{tip}(t)$, $y_{tip}(t)$, $z_{tip}(t)$ which are shown in Figure 6-1.

Equation 6.6 shows how the length of the gangway is calculated in 3d.

$$L(t) = \sqrt{(x_{td} - x_{tip}(t))^2 + (y_{td} - y_{tip}(t))^2 + (z_{td} - z_{tip}(t))^2} \quad (6.6)$$

The time derivative of equation 6.6 is used to calculate the telescoping velocity.

$$v_{tel}(t) = \dot{L}(t) = \frac{-x_{tip}(t)(x_{td} - x_{tip}(t)) - y_{tip}(t)(y_{td} - y_{tip}(t)) - z_{tip}(t)(z_{td} - z_{tip}(t))}{L(t)} \quad (6.7)$$

The telescoping force in 3d is calculated by implementing equation 6.5 and 6.7 in equation 4.5.

6.2.3 Luffing force

The luffing force in 3d is calculated by implementing equation 6.6 and 6.7 in equation 4.14.

6.2.4 Slewing force

From Ampelmann tests it is derived that the slewing gangway causes a damping moment due to the internal damping of the gangway. The approach of calculating the slewing force is similar to the approach of calculating the luffing force. The slewing velocity is calculated by taking the time derivative of the slewing angle, which is dependent on the position of the buoy. The slewing angle is calculated by equation 6.8 using the righthand rule for positive slewing angles.

$$\sin(\beta(t)) = \frac{x_{tip}(t) - x_{td}}{L(t)} \quad (6.8)$$

By taking the time derivative of equation 6.8, the slewing velocity is calculated by equation 6.9.

$$\dot{\beta}(t) = \frac{L(t)\dot{x}_{tip}(t) - (x_{tip}(t) - x_{td})\dot{L}(t)}{L^2(t) \cos(\beta(t))} \quad (6.9)$$

The rotational slewing damper causes a moment at the connection point of the tip caused by the connected gangway. This moment is projected on the buoy as a force perpendicular to the gangway which is visualized in Figure 6-2.

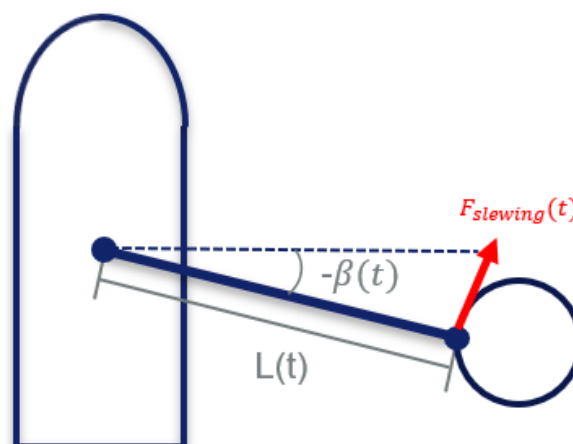


Figure 6-2 Slewing force.

The slewing force is calculated with equation 6.10.

$$F_{slewing}(t) = \frac{C_{slewing} \dot{\beta}(t)}{L(t)} \quad (6.10)$$

With the slewing damping coefficient derived from the Ampelmann tests.

$$C_{slewing} = 453.390 \frac{Nms}{rad}$$

Implementing equation 6.6 and 6.9 into equation 6.10 finds the slewing force in 3d.

6.2.5 Global gangway forces

The forces caused by internal damping of the gangway are all perpendicular to each other in 3D (Figure 6-3), which results in the force vector (equation 6.11) where the slewing force is directed in the x-direction of the local coordinate system, the telescoping force in y-direction and the luffing force in z-direction.

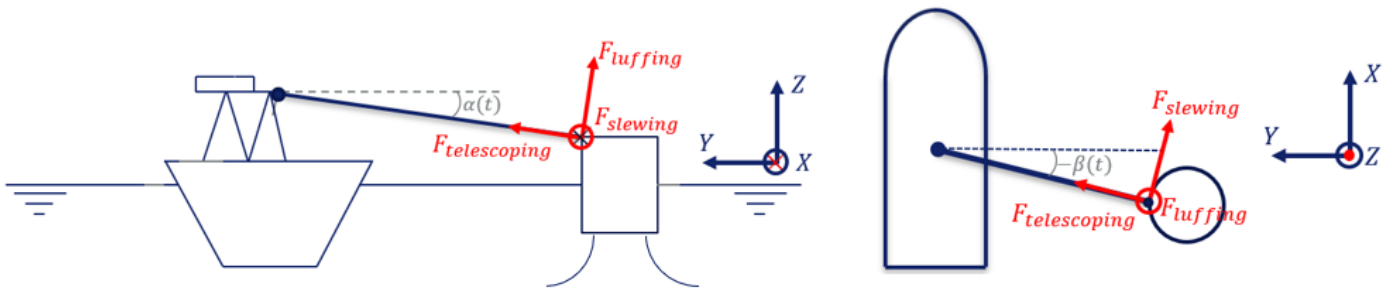


Figure 6-3 3D representation gangway forces

$$F_{gw} = \begin{bmatrix} F_{slewing} \\ F_{telescoping} \\ F_{luffing} \end{bmatrix} \quad (6.11)$$

The force vector changes its orientation caused by luffing and slewing. To implement all gangway forces in aNySIM, they have to be transformed from the local gangway coordinate system to the global coordinate system. This is done by applying the same method as in chapter 6.2, but the rotation matrix is now based on the rotations of the gangway. The elementary rotation matrix for telescoping does not exist since telescoping causes a translation and not a rotation. The elementary rotation matrices for slewing and luffing are shown in equations 6.12 and 6.13.

$$R_z = R_{slewing} = \begin{bmatrix} 1 & 0 & 0 \\ 0 & \cos(\beta) & -\sin(\beta) \\ 0 & \sin(\beta) & \cos(\beta) \end{bmatrix} \quad (6.12)$$

$$R_x = R_{luffing} = \begin{bmatrix} \cos(\alpha) & -\sin(\alpha) & 0 \\ \sin(\alpha) & \cos(\alpha) & 0 \\ 0 & 0 & 1 \end{bmatrix} \quad (6.13)$$

The order of multiplying the elemental rotation matrices follows from the fact that again active transformation is used to transform the force vector from the local coordinate system to the global coordinate system. Implementing equation 6.11-6.13 into equation 6.14, results in the global force vector caused by the Ampelmann system acting on the buoy.

$$F_{global} = R_{slewing} R_{luffing} F_{gw} \quad (6.14)$$

6.3 Operational limits

An Ampelmann system can only operate within its operational limits. If these operational limits are exceeded, the Ampelmann system is not allowed to work. The boundaries of an Ampelmann system are determined by operational limits of the hexapod and gangway (Roethof, 2015). Since in this thesis it is assumed that the residual vessel motions, which are not compensated by the dp-system, are within the compensating limits of the hexapod, the limits of the hexapod are not included. The operational limits of the gangway are based on the mechanical limits of the Ampelmann system and on safety regulations based on seakeeping criteria of Nordforsk (NORDFORSK, 1987). Since the gangway is modeled as a massless damper the acceleration limits of the gangway are not included in the workability study. The mechanical limits of the gangway system result in a minimum and maximal gangway length and luffing velocity. The gangway length limitation is caused by the minimum and maximum telescoping length. According to the luffing cylinders specification, they have a limited working velocity. This is translated to the operational luffing velocity of the gangway (Ampelmann Operations B.V., 2014).

Based on the seakeeping criteria of Nordforsk, Ampelmann has set up safety operational limits. This results that the luffing angle and the telescoping velocity of the gangway have certain limits. The operational limits which are included for the workability study, for an Ampelmann A-type, are shown in Table 6-1.

Table 6-1 Operational limits gangway.

Operational parameter	Lower limit	Upper limit
Luffing angle [rad]	-0,3	0,3
Luffing velocity [rad/s]	-0,05	0,05
Gangway length [m]	19	23
Telescoping velocity [m/s]	-1	1

6.4 Sea states

For the workability study, the responses of the buoy and gangway are different for different sea states. The conditions for long-term statistics are not stationary which makes it not feasible to present the time-series of the wave by its surface elevation (Holthuijsen, 2007). The long term statistics at the location of the CALM buoy is observed and documented for a duration of 3 hours. A method to document the long term wave data is to collect the observations according to its significant wave height (Hs), its zero-crossing period (Tz) and its mean direction. The data is collected in a wave scatter diagram with on the horizontal axis the zero-crossing period and on the vertical axis the significant wave height. The percentage of observations per Hs-Tz combination are noted. Table 6-2 shows the wave scatter diagram of the location of the CALM buoy in Papua New Guinea (Argoss, 2016).

Table 6-2 Wave scatter diagram Papua New Guinea (01-03-1997 – 28-02-2007).

Hs	Tz	lower	2	3	4	5	6	7	8	9	
lower	upper	3	4	5	6	7	8	9	10	Total	
0	0,25	0,04	0,24	0,15	0,09	0,11	0,08	*	-	0,71	
0,25	0,5	0,52	1,29	1,45	1,56	0,87	0,25	0,05	-	5,99	
0,5	0,75	1,25	3,97	4,52	4,45	2,23	0,62	0,08	-	17,12	
0,75	1	0,14	7,23	6,15	3,84	2,22	0,76	0,21	0,05	20,60	
1	1,25	-	3,89	10,57	2,96	1,26	0,50	0,08	0,04	19,30	
1,25	1,5	-	0,72	9,54	4,18	1,31	0,17	0,12	0,01	16,05	
1,5	1,75	-	0,06	5,47	3,81	0,94	0,12	0,02	0,05	10,47	
1,75	2	-	*	3,25	1,58	0,69	0,14	-	0,05	5,71	
2	2,25	-	-	0,67	1,47	0,19	0,03	-	-	2,36	
2,25	2,5	-	-	0,02	0,95	0,04	0,02	-	-	1,03	
2,5	2,75	-	-	-	0,42	0,03	-	-	-	0,45	
2,75	3	-	-	-	0,1	0,03	-	-	-	0,13	
3	3,25	-	-	-	*	0,04	-	-	-	0,04	
3,25	3,5	-	-	-	-	0,01	-	-	-	0,01	
Total		1,95	17,40	41,79	25,41	9,97	2,69	0,56	0,20	100,00	

* denotes values less than 0.01%

6.5 Workability approach and results

With the sea states and operational limits known, all required inputs are present to create time-series of the workability parameters of the Ampelmann system with the numerical model in aNySIM. The significant wave height and zero-crossing period of each sea state are implemented to create a Jonswap spectrum using head waves. The duration of the modeled time-series is equal to the duration of the observations of long-term statistics of the wave scatter diagram, which is typically 3 hours, with a timestep of 0.1s. A study done by Bergmans (Bergmans, 2017) shows that for simulations from a duration of 8000s, the number of time-series with a Jonswap spectrum with a randomized phase does not affect the result of the workability study. As a result of this study, every sea state is modeled once for the workability study in this thesis. This creates a database of 64 time-series in which for every timestep the values of each working limit of the gangway are saved. These time-series are analyzed in a MATLAB tool to calculate the operability per sea state. The operability of a sea state shows the percentage of time the Ampelmann system can be operational. If one of the workability limits exceeds its limit, it is assumed that for the next 300 seconds the operation cannot continue due to the fact that the gangway should clear all people, uncouple from the buoy and retract. The MATLAB tool calculates the percentage of time the Ampelmann system can be operational in a time span of 3 hours in a certain sea state. Table 6-3 shows the result of the operability per sea state with dynamic interaction of the gangway and the buoy included and Table 6-4 shows the result of the operability per sea state by a kinematic approach.

Table 6-3 Operability results with dynamic interaction.

Hs	Tz	lower	2	3	4	5	6	7	8	9
lower	upper	3	4	5	6	7	8	9	10	
0	0,25	1	1	1	1	1	1	1	-	-
0,25	0,5	1	1	1	1	1	1	1	1	-
0,5	0,75	1	1	1	1	1	1	1	1	-
0,75	1	1	1	1	0,89	0,89	0,97	1	1	1
1	1,25	-	1	0,41	0,17	0,29	0,70	0,83	0,91	0,91
1,25	1,5	-	0,97	0,02	0,01	0	0,07	0,28	0,52	0,52
1,5	1,75	-	0,83	0	0	0	0	0,01	0,11	0,11
1,75	2	-	-	0	0	0	0	-	0	0
2	2,25	-	-	0	0	0	0	-	-	-
2,25	2,5	-	-	0	0	0	0	-	-	-
2,5	2,75	-	-	-	0	0	-	-	-	-
2,75	3	-	-	-	0	0	-	-	-	-
3	3,25	-	-	-	-	0	-	-	-	-
3,25	3,5	-	-	-	-	0	-	-	-	-

Table 6-4 Operability results by kinematic approach.

Hs	Tz	lower	2	3	4	5	6	7	8	9
lower	upper	3	4	5	6	7	8	9	10	
0	0,25	1	1	1	1	1	1	1	-	-
0,25	0,5	1	1	1	1	1	1	1	1	-
0,5	0,75	1	1	1	1	1	1	1	1	-
0,75	1	1	1	1	0,86	0,86	0,97	1	1	1
1	1,25	-	1	0,35	0,16	0,27	0,63	0,73	0,91	0,91
1,25	1,5	-	0,97	0,02	0,01	0	0,04	0,24	0,42	0,42
1,5	1,75	-	0,32	0	0	0	0	0	0,02	0,02
1,75	2	-	-	0	0	0	0	-	0	0
2	2,25	-	-	0	0	0	0	-	-	-
2,25	2,5	-	-	0	0	0	0	-	-	-
2,5	2,75	-	-	-	0	0	-	-	-	-
2,75	3	-	-	-	0	0	-	-	-	-
3	3,25	-	-	-	-	0	-	-	-	-
3,25	3,5	-	-	-	-	0	-	-	-	-

The highlighted cells in Table 6-3 and Table 6-4 show the changed values between both tables. In low- and high-frequency sea states it shows that the dynamic interaction of the gangway and the buoy does affect the operability significantly. To study what causes this, the operability of the individual operational limits are studied. In Appendix 9.8 the operability per sea state, per operational limit are given. It shows that the luffing velocity is the governing operational limit. Equation 4.15 shows that the luffing velocity depends on the heave motion of the buoy and telescoping length and telescoping velocity. Due to head waves and the geometry of the gangway with respect to the buoy, the telescoping length and velocity does not vary significantly, which is also the reason why these workability parameters are not governing. The heave motion of the buoy is the most important parameter considering the luffing velocity of the gangway.

In chapter 5 it shows that the hydrodynamic damping of the buoy is the governing factor of the total damping force on the buoy. Analyzing the frequency dependent hydrodynamic damping in heave shows that for high- and for low-frequency sea states the hydrodynamic damping is significantly lower than for mid-frequency waves (Figure 5-26). The relatively low hydrodynamic damping in heave enables the damping forces of the gangway to play a more significant role in the total damping force acting on the buoy. It is clearly visible, when comparing Table 6-3 and Table 6-4, that the operability is improved when the dynamic interaction is included in low- and high-frequency sea states.

Not only the zero-crossing period affects the response of the buoy but also the significant wave height. When looking at a fixed zero-crossing period it can be concluded that the higher the significant wave height, the lower the operability, since higher waves exert larger motions of the buoy. The mooring lines in the numerical model are linearized within a certain range and when the significant wave height increases the buoy moves outside this linear range. The results of the time-series for large buoy motion show that the buoy has unrealistic results when the buoy exits the linear region. This results in very large surge motions, resulting in unrealistically high telescoping velocities and gangway lengths. In Table 6-3 and Table 6-4 it shows that according to the linearized

numerical model the Ampelmann is not operational in sea states with a significant wave height larger than 1.75m.

Using this research it cannot be concluded whether the results for these high sea states are correct since only the linear response of the buoy is validated in this thesis. The effect of the dynamic interaction on the complete workability is not only dependent on the operability of one sea state but also on the probability of that sea state occurring. The workability is calculated by multiplying the operability with the probability of that sea state occurring. For low- and high-frequency sea states, the dynamic interaction affects the workability significantly. The probability of these sea states occurring is small, which can be seen in Table 6-2. The results of the complete workability study are given in Table 6-5 and Table 6-6 with and without dynamic interaction, respectively. The effect of the dynamic interaction of the Ampelmann system results in a higher workability of less than 1% caused by the damping forces of the gangway.

Table 6-5 Workability result with dynamic interaction.

Hs	Tz	lower	2	3	4	5	6	7	8	9		
lower	upper	3	4	5	6	7	8	9	10	Total	Cumul.	
0	0,25	0,04	0,24	0,15	0,09	0,11	0,08	-	-	0,71	0,71	
0,25	0,5	0,52	1,29	1,45	1,56	0,87	0,25	0,05	-	5,99	6,70	
0,5	0,75	1,25	3,97	4,52	4,45	2,23	0,62	0,08	-	17,12	23,80	
0,75	1	0,14	7,23	6,15	3,42	1,98	0,74	0,21	0,05	19,91	43,72	
1	1,25	-	3,89	4,33	0,50	0,36	0,35	0,07	0,04	9,54	53,26	
1,25	1,5	-	0,70	0,20	0,04	0	0,01	0,03	0,01	0,98	54,24	
1,5	1,75	-	0,05	0	0	0	0	0	0,01	0,06	54,29	
1,75	2	-	-	0	0	0	0	-	0	0,00	54,29	
2	2,25	-	-	0	0	0	0	-	-	0,00	54,29	
2,25	2,5	-	-	0	0	0	0	-	-	0,00	54,29	
2,5	2,75	-	-	-	0	0	-	-	-	0,00	54,29	
2,75	3	-	-	-	0	0	-	-	-	0,00	54,29	
3	3,25	-	-	-	-	0	-	-	-	0,00	54,29	
3,25	3,5	-	-	-	-	0	-	-	-	0,00	54,29	
Total		1,95	17,37	16,79	10,06	5,46	2,05	0,44	0,10	-	-	
Cumul.		1,95	19,32	36,11	46,19	51,73	53,78	54,19	54,29	-	-	

Table 6-6 Workability result with kinematic approach.

Hs	Tz	lower	2	3	4	5	6	7	8	9		
lower	upper	3	4	5	6	7	8	9	10	Total	Cumul.	
0	0,25	0,04	0,24	0,15	0,09	0,11	0,08	-	-	0,71	0,71	
0,25	0,5	0,52	1,29	1,45	1,56	0,87	0,25	0,05	-	5,99	6,70	
0,5	0,75	1,25	3,97	4,52	4,45	2,23	0,62	0,08	-	17,12	23,82	
0,75	1	0,14	7,23	6,15	3,30	1,91	0,74	0,21	0,05	19,73	43,55	
1	1,25	-	3,89	3,70	0,47	0,34	0,32	0,06	0,04	8,81	52,36	
1,25	1,5	-	0,70	0,19	0,04	0	0,01	0,03	0	0,97	53,33	
1,5	1,75	-	0,02	0	0	0	0	0	0	0,02	53,35	
1,75	2	-	-	0	0	0	0	-	0	0,00	53,35	
2	2,25	-	-	0	0	0	0	-	-	0,00	53,35	
2,25	2,5	-	-	0	0	0	0	-	-	0,00	53,35	
2,5	2,75	-	-	-	0	0	-	-	-	0,00	53,35	
2,75	3	-	-	-	0	0	-	-	-	0,00	53,35	
3	3,25	-	-	-	-	0	-	-	-	0,00	53,35	
3,25	3,5	-	-	-	-	0	-	-	-	0,00	53,35	
Total		1,95	17,34	16,16	9,92	5,46	2,01	0,43	0,09	-	-	
Cumul.		1,95	19,29	35,45	45,37	50,83	52,83	53,26	53,35	-	-	

6.6 Workability per operational limit

The governing operational limit is the luffing velocity of the gangway. Studying the importance of reducing the luffing velocity during operation, the workability per operational limits is calculated. The workability of each individual operational limit is calculated in the same manner as has been done for the total workability with and without the dynamic interaction. The results of the workability per operational limit are shown in Table 6-7.

Table 6-7 Workability study per operational limit.

Operational limit	Workability with dynamic interaction	Workability without dynamic interaction
Luffing angle	99,88	98,21
Gangway length	99,81	95,82
Telescoping velocity	99,88	95,19

The remaining operational limits besides luffing velocity are only exceeded in extreme sea states, which rarely occurs. The results from Table 6-7 show that with the assumptions made in this thesis the workability will improve significantly when the luffing velocity of the gangway can be reduced.

6.7 Conclusion

For analyzing the influence of dynamic interaction of an Ampelmann system with a CALM buoy, a workability study is performed. To do a representative workability study, the gangway is modeled as massless dampers in 3d connected to the buoy. The results of the workability study with a dynamic approach are compared with the results of a kinematic approach. This shows that the dynamic interaction plays a significant role in improving the operability for high- and low-frequency sea states. The reason is that the governing operational limit, the luffing velocity of the gangway, is mainly influenced by the heave motion of the buoy. The total damping force of the buoy in heave mainly consists of the hydrodynamical damping force and the damping forces of the gangway. The results of the diffraction software show that the frequency dependent hydrodynamic damping coefficient for heave is significantly lower in the low- and high-frequency region compared to the mid-frequency region. This results in a more significant effect of the gangway damping forces in the total damping force of the buoy. Low- and high-frequency sea states are less likely to occur which means that dynamic interaction of the gangway and the buoy will not have significant effect on the total workability compared to the total workability done with a kinematic approach. The importance of the governing operational limit, the luffing velocity, is studied by comparing the workability of each operational limit individually. All other operational limits have a significantly higher workability, which means that in this thesis the complete workability improves if the luffing velocity of the gangway can be reduced.

7. Conclusion and recommendations

During this thesis, it has been proven that the dynamic interaction of the gangway forces and the CALM buoy does affect the workability. Certain steps have been taken to reach the goal of this research, which are presented in this chapter, followed by recommendations for further studies regarding this topic.

7.1 Conclusion

To reach the goal of this thesis a numerical time-domain model is delivered where the coupling effect of a CALM buoy and an Ampelmann system is studied. The Ampelmann system is modeled as massless dampers, which are always connected to the CALM buoy. The gangway forces are dependent on the motions of the buoy. This model is used to study the effect of the damping forces, caused by the Ampelmann system, on the workability of the Ampelmann system.

At first the model is restricted to in-plane motion in the y - z plane, reducing the degrees of freedom and to get a clear idea of the coupling effects of the gangway and the buoy. An analytical approach is used to set up the equations of motion of the buoy including the massless dampers representing the gangway of the Ampelmann system. A sensitivity study of the parameters of the damping forces shows that the ratio of the hydrodynamic damping coefficient and the gangway damping coefficient is governing.

A diffraction model shows that the hydrodynamical damping of the buoy is minimal at low- and high frequency waves. This information is used to build a case study with low-frequency waves, analyzing the influence of the gangway forces on the response of the buoy. The equations of motion are solved in an ODE solver in Python, studying the effect of the dynamic interaction between the gangway and the CALM buoy, and to verify the aNySIM model. Both models show that the amplitude of the responses for sway and heave are very similar. The main differences between both models are the phase shift and linearity of the responses. In the Python model all parameters are fully linearized where in aNySIM non-linear effects of damping and mooring stiffness occurs. This results that especially in heave the CALM buoy responds not completely linear in aNySIM compared to the Python model. The roll response of the buoy, exerted by long waves, is negligible as shown by both models. Including the dynamic interaction in the case study, results in reduced response amplitudes up to 10% for sway and heave.

To perform a workability study, the numerical model in aNySIM is extended to all degrees of freedom for the CALM buoy and the gangway. The sea states from the wave scatter diagram for the location of the buoy in Papua New Guinea are used to run time-domain simulations of the buoy with and without dynamic interaction. Every H_s - T_z combination of the wave scatter diagram is included in the Jonswap spectrum, creating unidirectional head waves for the buoy. The operational limits of the gangway are analyzed for every simulation and when, during the simulation, the operational limits are exceeded, the Ampelmann system cannot operate for a period of time. From these simulations the operability per sea state is calculated with dynamic interaction included and by a kinematic approach. The results show that the dynamic interaction significantly improves the operability in low- and high-frequency sea states. The operability for every operational limit is studied, which shows that the luffing velocity of the gangway is the limiting operational factor.

The workability depends on the operability per sea state and the probability of occurrence of this sea state. Low- and high-frequency sea states have a low probability of occurrence and thus a low impact on the total workability. The total workability is improved with almost 1% by including the dynamic interaction in the workability study.

7.2 Recommendations

The research question has been answered by using different models. These models can be used for further research, and the accuracy of the model can be improved. The following recommendations based on this thesis are made:

- Compare the responses of the aNySIM model and the Python model with the project in Papua New Guinea. The response of the buoy with and without a connected Ampelmann system can be measured and compared to the outcome of the aNySIM model and Python model. If the responses of the actual project and the models are comparable, it is recommended to not include the dynamic interaction in the workability analyses for projects with an A-type Ampelmann system and a CALM buoy. The workability is slightly affected by the dynamic interaction and including dynamic interaction extends the duration of the workability study significantly. When the Python model coincides with the response of the actual project, it can be used to perform quick checks for implementing or changing parameters.
- Include the inertia of the gangway in the study. This will show if the inertia will affect the response of the buoy. A quick check can be done by including the inertia of the gangway in the EOM and implementing it in the ODE-solver in Python. With these results it can be decided to implement the inertia of the gangway in the aNySIM model to perform a workability study.
- Verify the damping of the buoy by doing model tests. An estimation is made to determine the hydrodynamical damping, including viscous damping, and the accuracy can be studied by comparing offset model tests to offset tests in aNySIM.
- Study the impact of different Ampelmann systems in the aNySIM model. This study shows that the ratio of the gangway damping and the hydrodynamical damping is an important aspect in the response of the buoy. Ampelmann has multiple systems with different parameters for each system such as the damping coefficients of the gangway, and the operational limits. These parameters might affect the workability, or introduce other governing operational limits.
- Study the effect of residual motion of the Ampelmann system. In actual operation it might occur that the vessel motions are too big to compensate by the Ampelmann system. This results in residual motions of the transferdeck and gangway (Wiegerink, Modelling of Coupled Vessel-Ampelmann Systems for Workability Studies, 2015). The luffing velocity is one of the limitation factors that can be influenced by the residual motions. Even when residual motions are not present, but the host vessel is moving out of phase compared to the buoy, it can increase the luffing velocity.
- Perform a sensitivity study about the effect of the size of the target vessel. If it can be said that from a certain size of buoy, the dynamic interaction does not play a significant role in the workability study, larger buoys are not required to study.
- Expand the modularity of the model to change the target vessel. For future projects different CALM buoys, or other small vessel might be a target vessel for an Ampelmann project. The model can be adjusted such that the hydrodynamic database of the potential customer can be implemented and creating a diffraction model is not needed anymore.
- Include dynamic mooring lines in the current aNySIM model. The mooring lines affect the response of the buoy. Due to linearization of the mooring lines the working range of the buoy is limited. Implementing dynamic mooring lines extends the working range and introduces non-linear mooring effect, which improves the accuracy of the aNySIM model.

- Build a tool in aNySIM to calculate the operability for every sea state automatically. In this thesis this is done manually. This consumes a lot of time which is not preferable using the model for different projects.

8. Bibliography

- A. Umar, T. D. (2003). Nonlinear Response of a Moored Buoy. *Ocean Engineering*, 22.
- A.L. Schwab, J. M. (2006, 09 10). How to Draw Euler Angles and Utilize Euler Parameters. *International Design Engineering Technical Conferences & Computers and Information in Engineering Conference*, p. 7.
- AMOG. (2017, 11 13). *Trenching Analyses; KMT CALM Buoy Trenching Analysis*.
- Ampelmann. (2019, 04 26). From Ampelmann: <https://www.ampelmann.nl/systems/a-type>
- Ampelmann Operations B.V. (2014). *Technical Information X-type, Technical Report*.
- Argoss, B. (2016, 06). *Metocean Data Papua New Guinea, BMT Argoss*.
- Bergmans, P. (2017). *Workability prediction for the Ampelmann A-type*.
- Chris Keijdener, A. J.-L. (2017). Personal communication.
- DredgingEngineering*. (2019, 02 18). From <http://dredgingengineering.com/moorings/lines/Offshore%20mooring%20lines%20mooring%20system.htm>
- Greenwood, D. (2012). *Advanced Dynamics*.
- Holthuijsen, L. (2007). *Waves in Oceanic and Coastal Waters*.
- J. van der Tempel, D. S. (2007). *Vessel, Motion Platform, Method for Compensation Motions of a Vessel and use of a Stewart Platform*.
- J.L. Cozijn, T. B. (2004, 06 20). Coupled Mooring Analysis for a Deep Water CALM Buoy. *23rd International Conference on Offshore Mechanics and Arctic Engineering*, p. 11.
- J.M.J. Journée, W. M. (2008). *Offshore Hydromechanics Second Edition*.
- Karl Johan Aström, R. M. (2003). *An Introduction for Scientists and Engineers*. Princeton University Press.
- L.V.S. Sagrilo, M. S. (2002). A coupled approach for dynamic analysis of CALM systems. *Applied Ocean Research*.
- MARIN. (2011). *Methods to Determine Damping Coefficients from the Results of Motion Decay Tests*.
- MARIN. (2018). *aNySIM Theory Documentation revision 1.2*.
- MARIN. (2018). *DiffraC Theory and User Guide Version 2.6.3*.
- NORDFORSK. (1987). *Seakeeping Criteria*.
- Ramnäs Bruk. (2009). *Ramnäs Bruik Quality Chains and Accessories*.
- Roethof, T. (2015). *Ship-to-CALM Buoy Transfer Workability Analysis Ampelmann Operations B.V. sbmoffshore*. (2019, 03 16). From https://www.sbmoffshore.com/wp-content/uploads/2013/09/SBMO-CALM_Original_2048.pdf

- SOFEC. (2011). *PNG CALM Buoy Design Loads Report*.
- SOFEC. (2011). *PNG CALM Buoy Report*.
- SOFEC. (2011). *Weight, Balance, Floatation & Stability Design Report for PNG CALM Buoy*.
- sofec. (2018, 07 17). From [http://www.sofec.com/specSheet/PNG\(3\).pdf](http://www.sofec.com/specSheet/PNG(3).pdf)
- Sreedharan, A. (2016). *Design of Ampelmann Ship to CALM buoy Connection*.
- Svitzer. (2018). *Svitzer Vision RAO Calculation*.
- T.H.J. Bunnink, G. d. (2002, 06). Coupled Mooring Analyses in Large Scale Model Tests on a Deepwater CALM Buoy in Mild Wave Conditions. *The 21st International Conference on Offshore Mechanics and Arctic Engineering* (p. 12). Oslo: OMAE.
- Wiegerink, J. (2015). *Modelling of Coupled Vessel-Ampelmann systems for Workability Studies*.
- Wiegerink, J. (2015). *Modelling of Coupled Vessel-Ampelmann Systems for Workability Studies*.
- William E. Boyce, R. C. (2017). *Boyce's Elementary Differential Equations and Boundary Value Problems, Global Edition*. Wiley. From http://tutorial.math.lamar.edu/pdf/Laplace_Table.pdf

9. Appendices

9.1 Buoy configuration

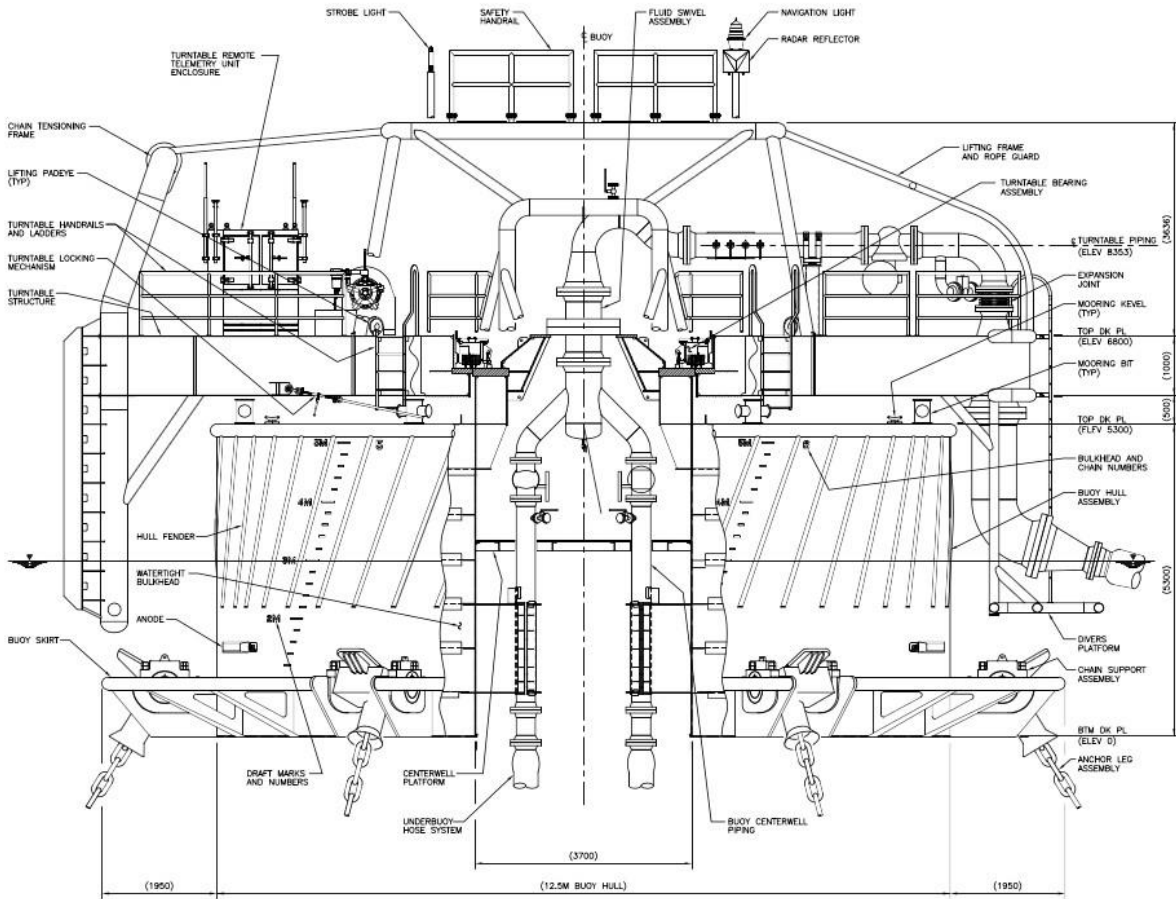


Figure 9-1 Buoy configuration.

9.2 AMOG Data

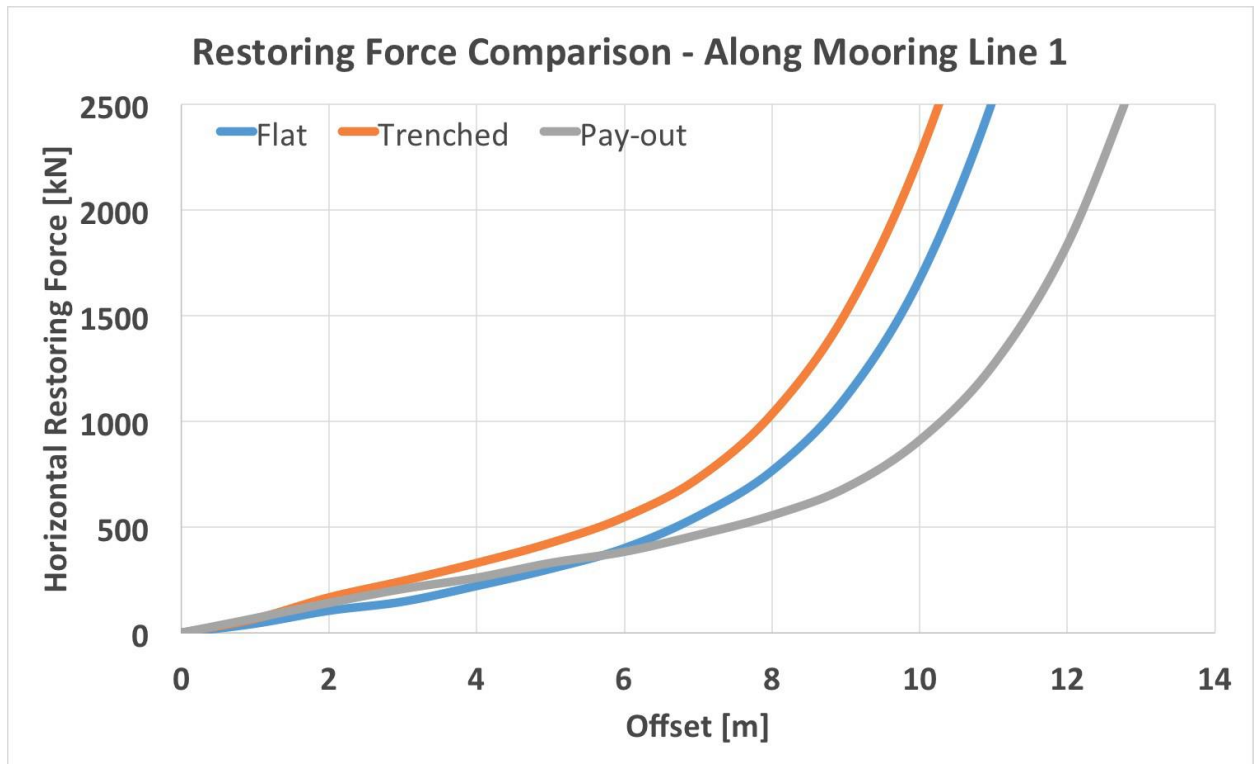


Figure 9-3 Restoring force in direction mooring line 1.

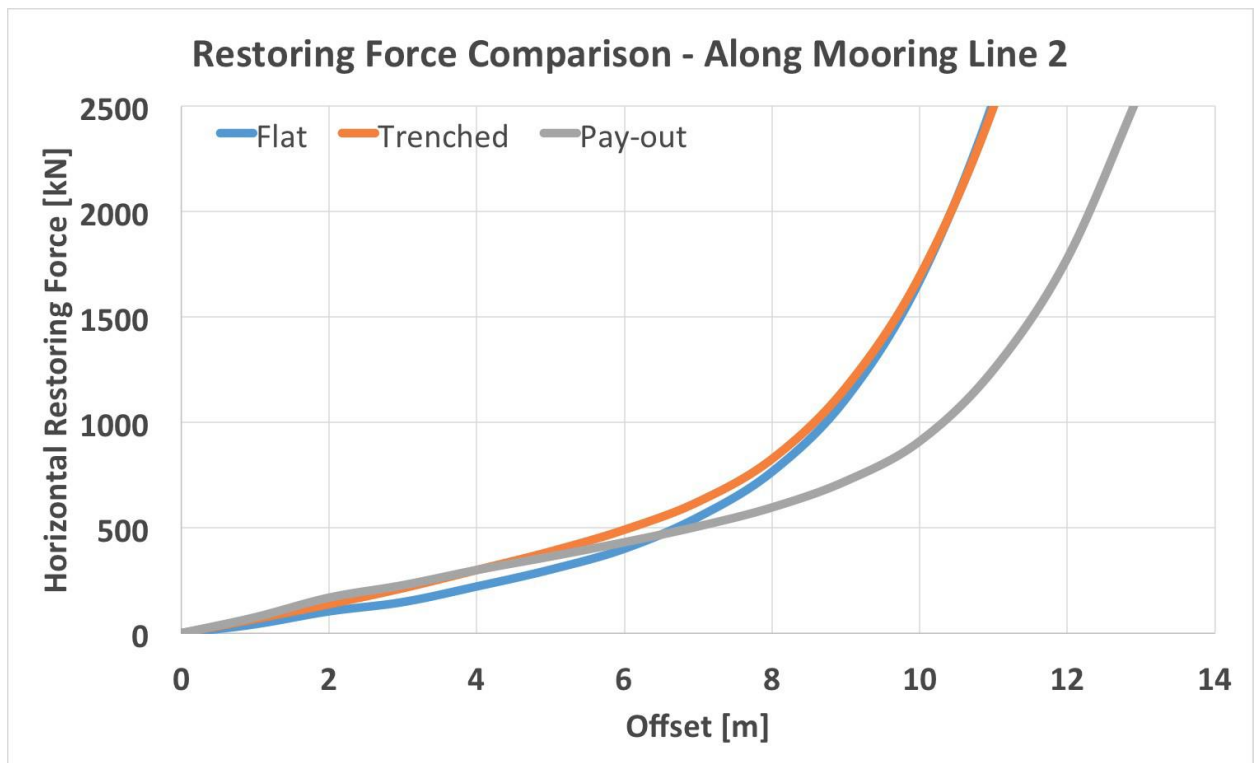


Figure 9-4 Restoring force in direction mooring line 2.

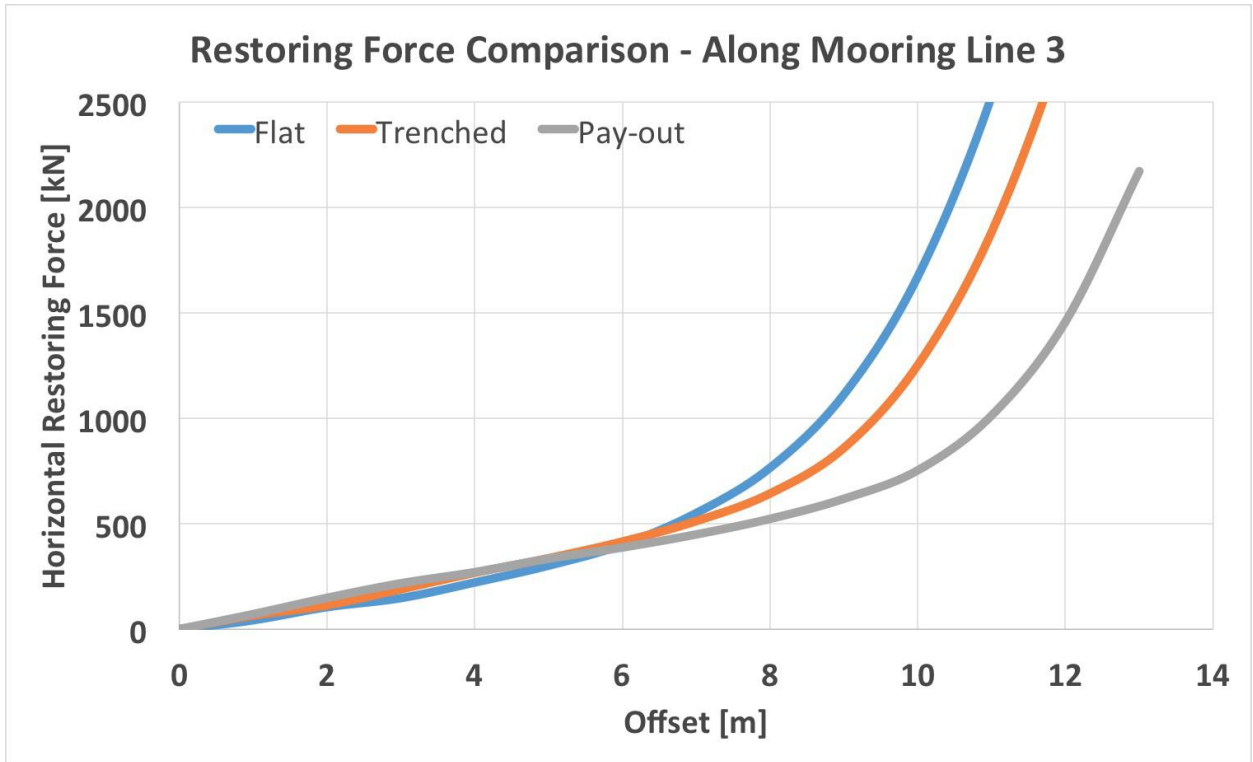


Figure 9-5 Restoring force in direction mooring line 3.

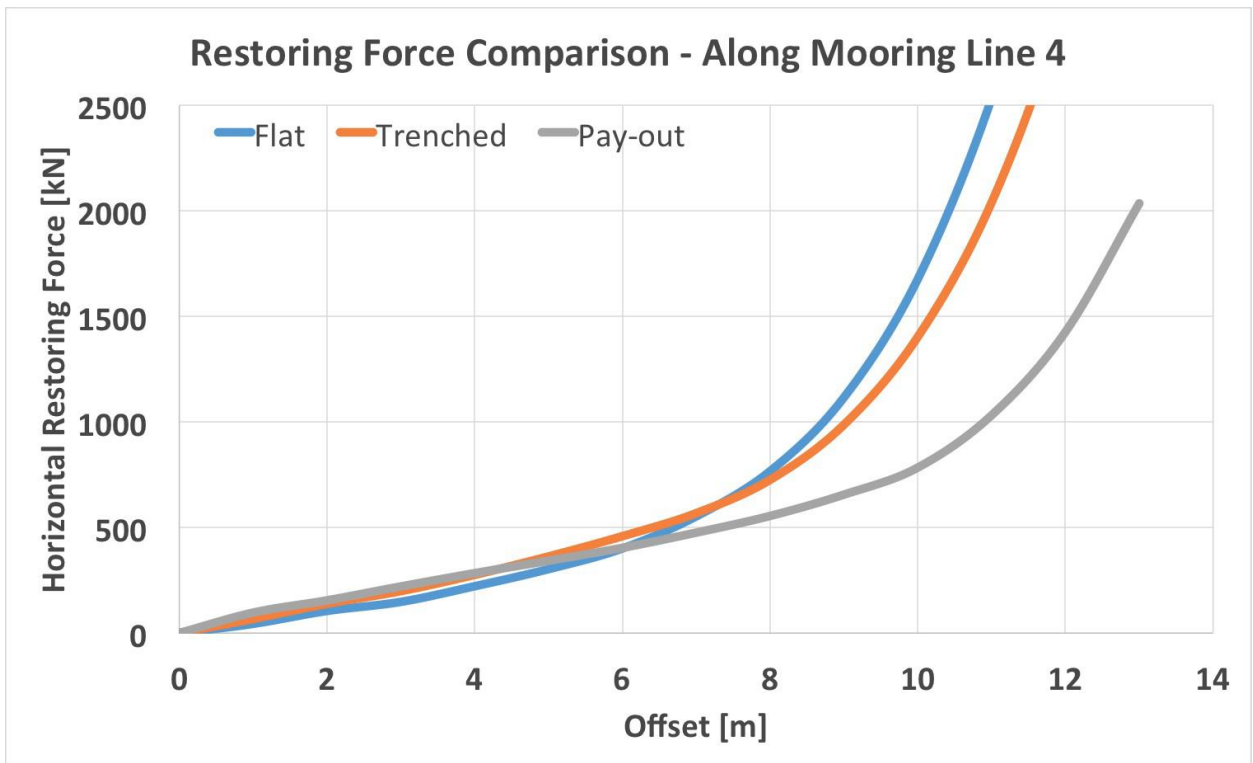


Figure 9-6 Restoring force in direction mooring line 4.

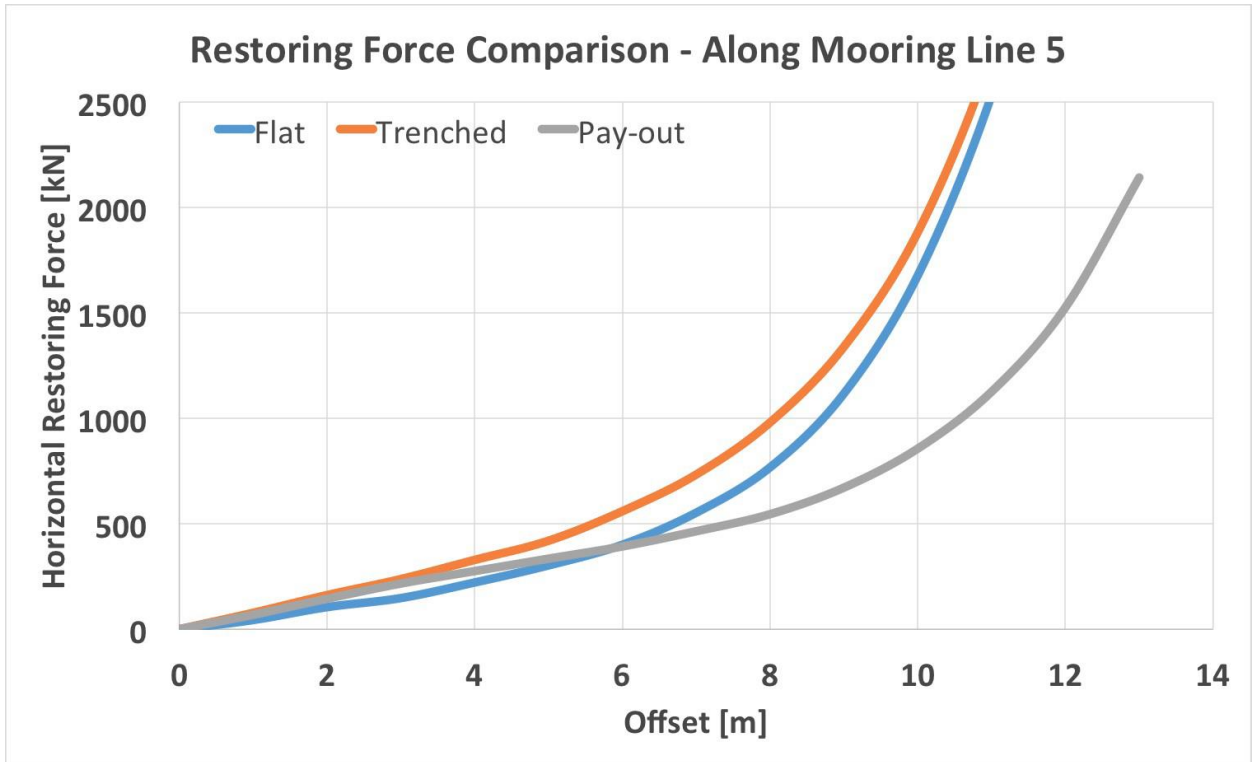


Figure 9-7 Restoring force in direction mooring line 5.

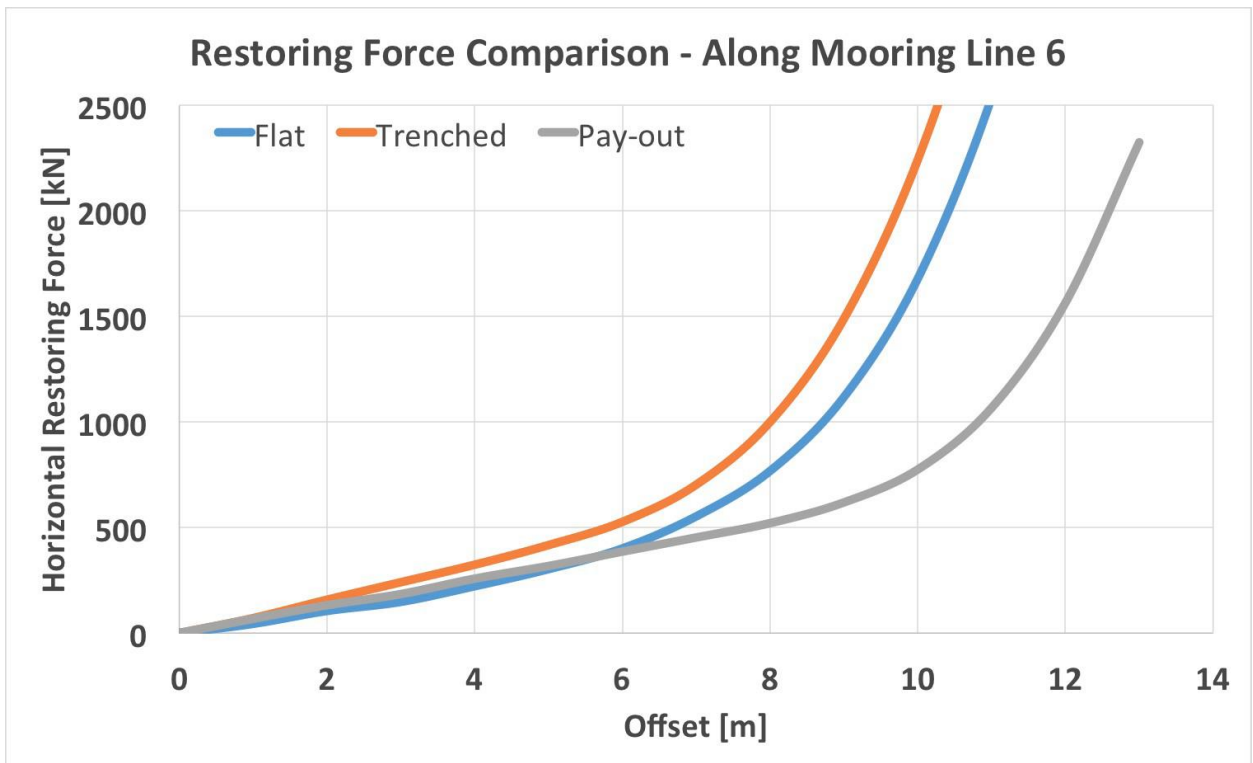


Figure 9-8 Restoring force in direction mooring line 6.

9.3 Diffraction results

Table 9-1 Diffrac data (at $\omega = 0.4$ rad/s, incoming angle = 90 deg).

	$x = 1$	$x = 2$	$x = 3$	$x = 4$	$x = 5$	$x = 6$
a_{1x}	1.435E+02	-8.795E-06	5.427E-03	-1.559E-03	3.952E+01	-2.061E-06
a_{2x}	2.475E-04	1.442E+02	-6.098E-05	-3.548E+01	-1.017E-03	-3.141E-05
a_{3x}	-2.069E-04	5.077E-04	5.788E+02	-3.937E-03	1.171E-03	2.643E-05
a_{4x}	-3.386E-04	-4.197E+01	-6.370E-04	2.058E+03	-7.415E-03	-6.957E-05
a_{5x}	4.093E+01	7.149E-04	-3.342E-02	-2.407E-03	2.064E+03	-4.061E-05
a_{6x}	-3.097E-06	-2.361E-05	4.028E-06	4.839E-06	-3.682E-06	-9.213E-07
b_{1x}	3.193E-01	1.469E-05	-9.310E-05	-5.637E-05	4.483E-01	-1.726E-06
b_{2x}	-1.264E-06	3.219E-01	8.030E-05	-4.370E-01	2.299E-04	-9.495E-07
b_{3x}	6.266E-05	4.402E-05	4.862E+01	-8.804E-04	2.136E-04	1.406E-06
b_{4x}	-4.095E-05	-4.527E-01	1.410E-04	6.145E-01	-6.308E-05	1.016E-06
b_{5x}	4.499E-01	3.701E-05	3.131E-04	-1.809E-04	6.318E-01	-5.195E-06
b_{6x}	-2.565E-09	-4.122E-08	1.106E-06	5.131E-08	-9.804E-07	-1.164E-08
F_x	6.486E-04	1.236E+02	1.084E+03	1.738E+02	3.838E-03	3.352E-05
ϕ_x	1.781E+02	8.992E+01	1.034E+00	2.699E+02	4.684E+00	3.316E+02

9.4 Offset tests aNySIM

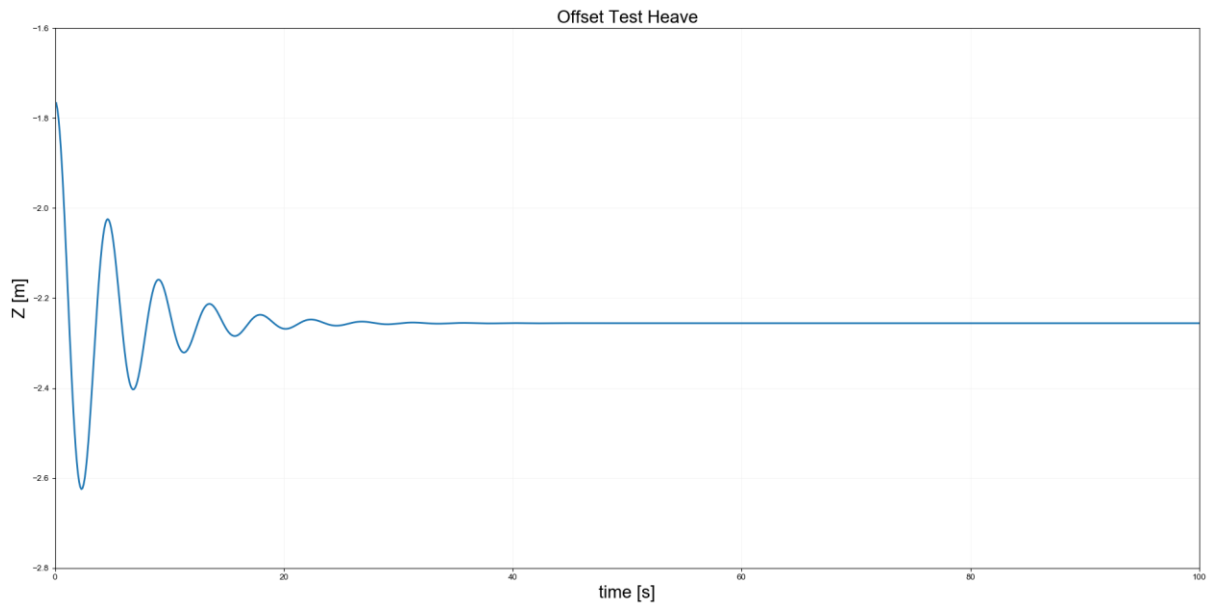


Figure 9-9 Decay test heave (+1m).

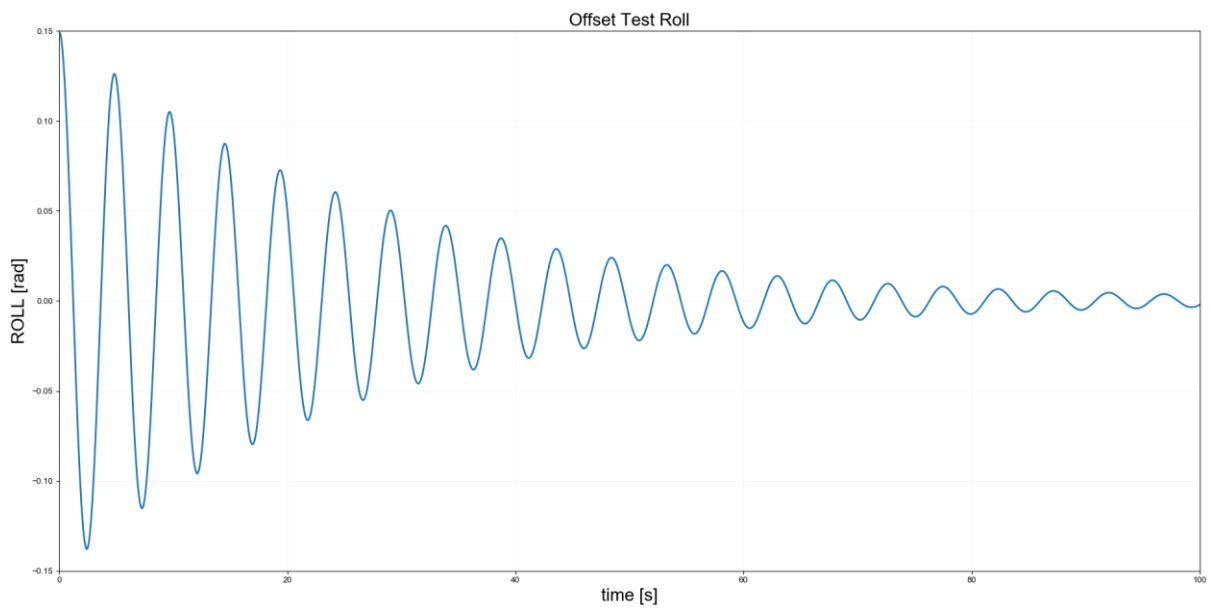


Figure 9-10 Decay test roll (+0.15rad).

9.5 Roll response case study

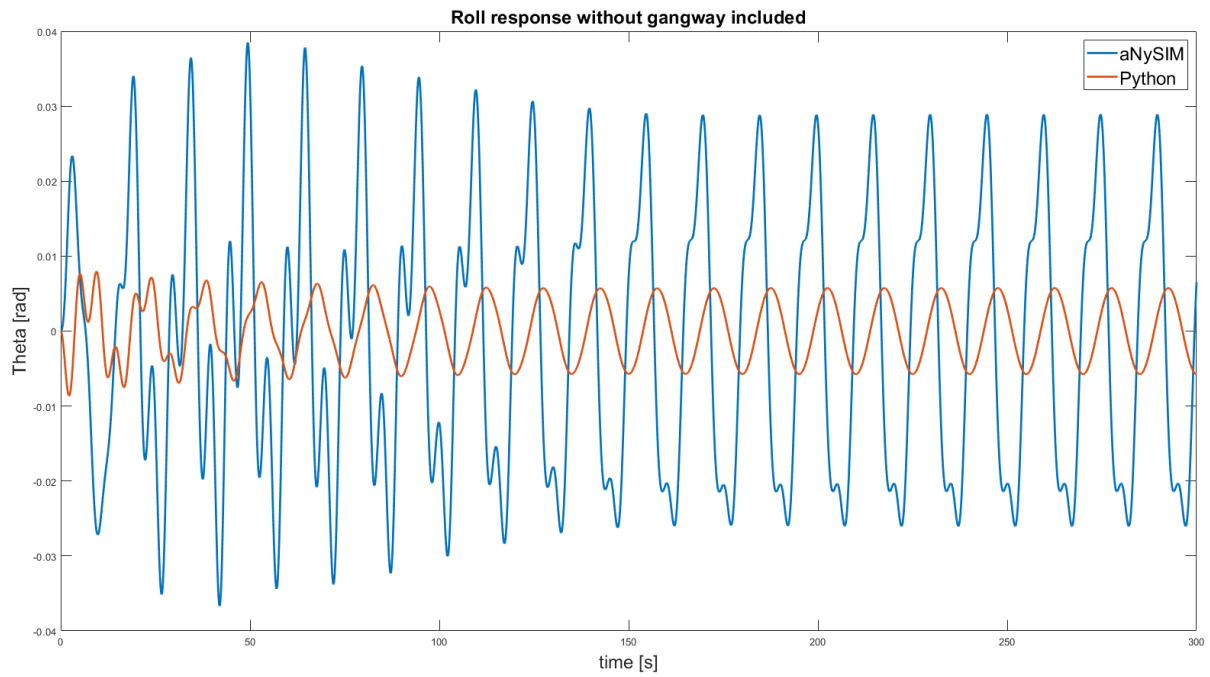


Figure 9-11 Roll response case study without dynamic interaction.

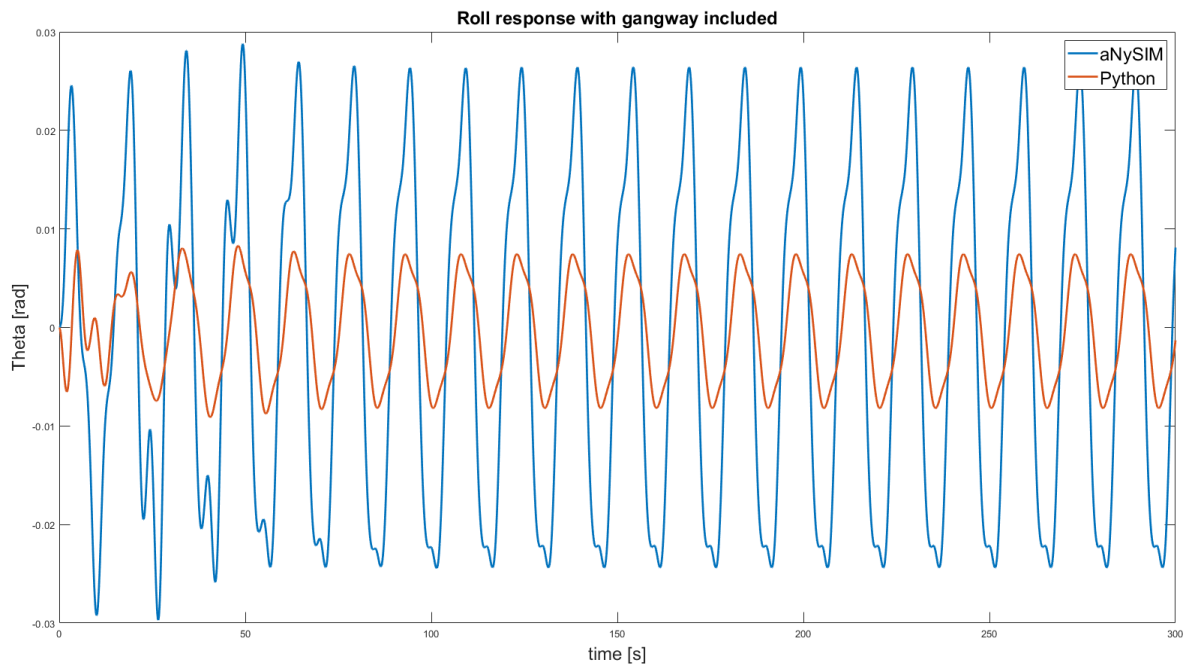


Figure 9-12 Roll response case study without dynamic interaction.

9.6 EOM analyses

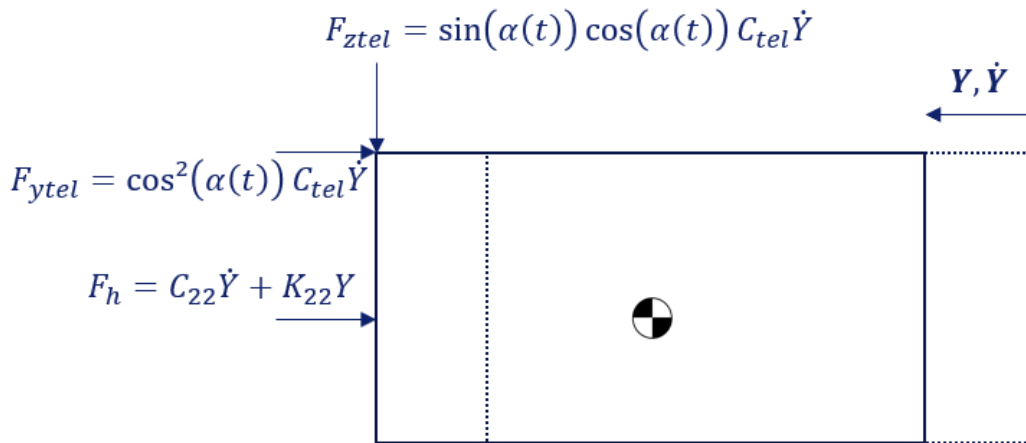


Figure 9-13 FBD telescoping force with Y-displacement.

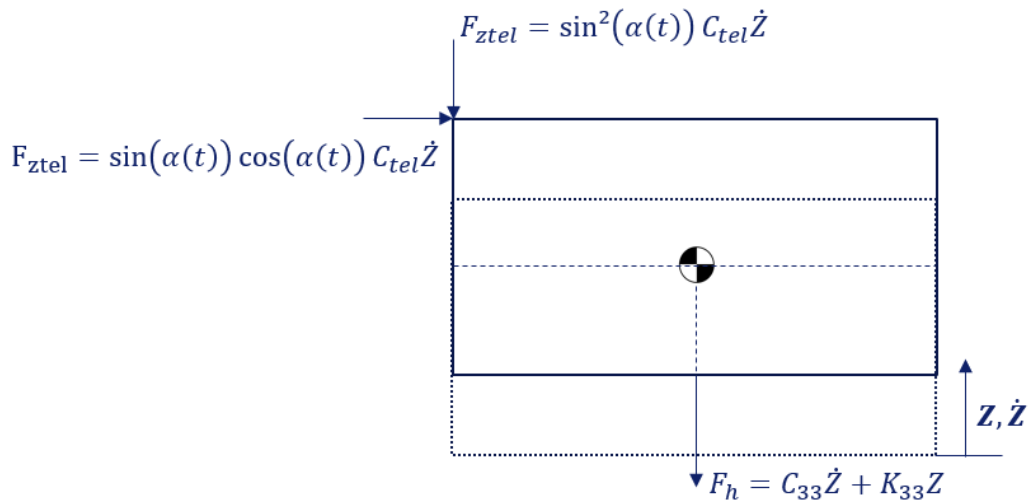
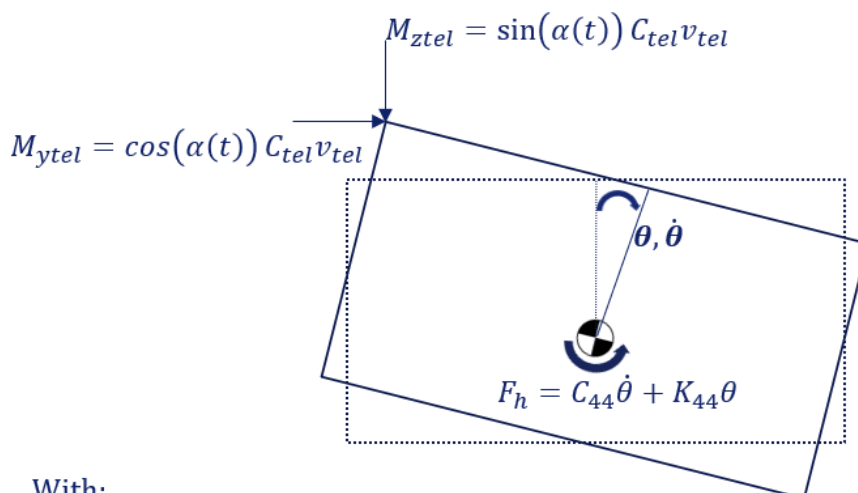


Figure 9-14 FBD telescoping force with Z-displacement.



With:

$$v_{tel} = [y_b(-\cos(\alpha(t))\theta(t) + \sin(\alpha(t))) + z_b(-\cos(\alpha(t)) - \sin(\alpha(t))\theta)]\dot{\theta}$$

Figure 9-15 FBD telescoping moment with Roll-displacement.

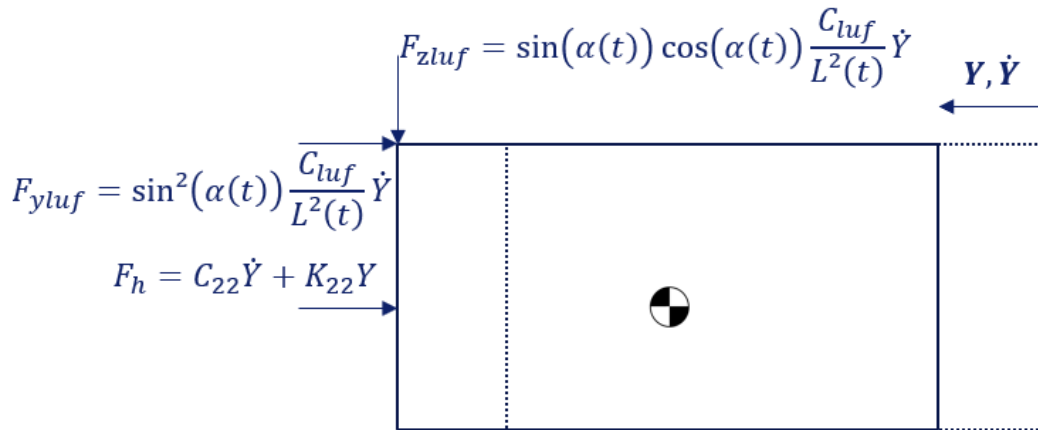


Figure 9-16 FBD luffing force with Y-displacement.

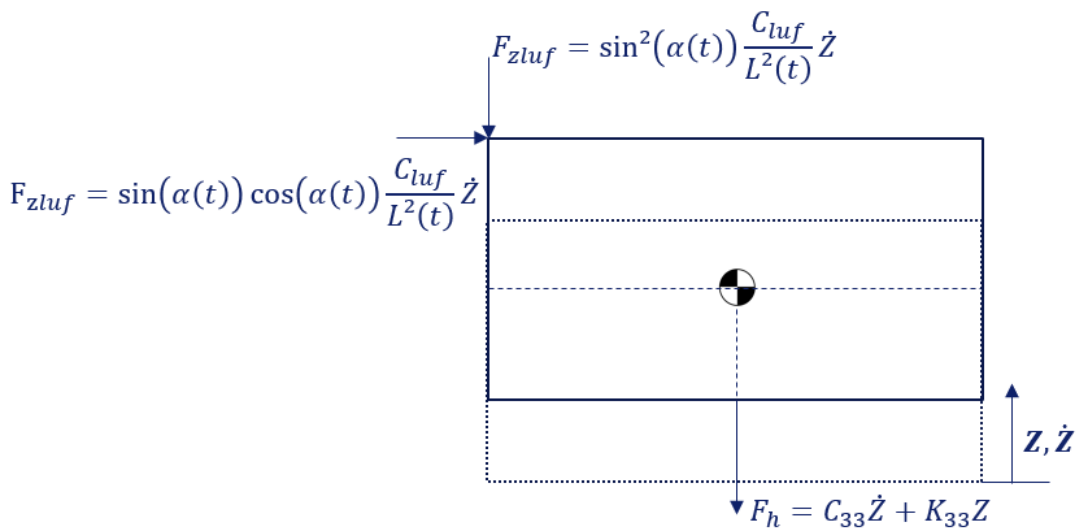
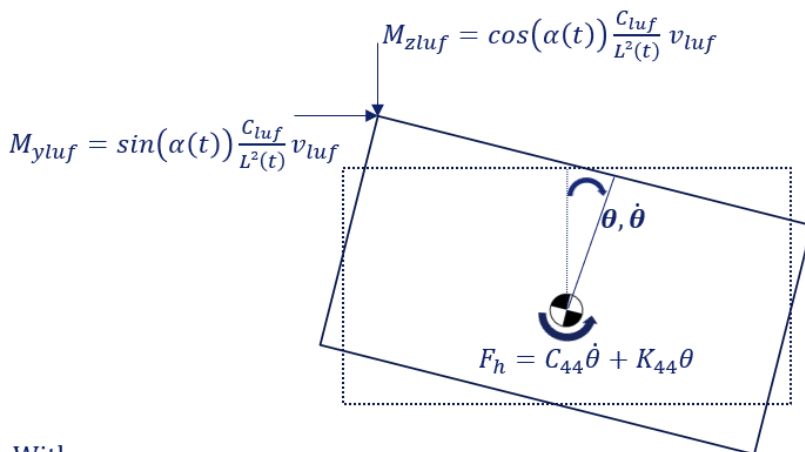


Figure 9-17 FBD luffing force with Z-displacement.



With:

$$v_{lu} = [y_{tip}(\cos(\alpha(t)) + \sin(\alpha(t))\theta(t)) + z_{tip}(-\cos(\alpha(t))\theta(t) + \sin(\alpha(t)))]\dot{\theta}(t)$$

Figure 9-18 FBD luffing moment with Roll-displacement.

9.7 ODE Solver

```
1. # -*- coding: utf-8 -*-
2. """
3. Created on Sun May 5 15:35:08 2019
4.
5. @author: mike.vanbeurden
6. """
7.
8.
9. # %% import libraries
10. import numpy as np
11. from scipy import interpolate
12. from scipy.integrate import solve_ivp
13. import plotter as pl
14. import matplotlib.pyplot as plt
15.
16. # %% Parameters
17.
18. # %% Time independent coefficients
19. m = 281600 #kg
20. a22 = 143500
21. a33 = 578800
22. a44 = 2058000
23. kxx = 4 #m
24. k22 = 50000 #N/m
25. k33 = 1270000 #N/m
26. k44 = 11017000 #Nm/rad
27. c22 = 39000 #Ns/m
28. c33 = 138890 #Ns/m
29. c44 = 427362 #Nms/rad
30. ctel = 9894.3 #Telescoping damping coefficient [Ns/m]
31. cluf = 746840 #Luffing damping coefficient [Nms/rad]
32. yb = 6.25
33. zb = 3.8 #z
34. ytd = 26
35. ztd = 7.43
36. beta = np.arctan(zb/yb); #rad
37. r = (yb**2 + zb**2)**0.5
38. ytip = (yb) # calculating ytip for this time step
39. ztip = (zb) # calculating ztip for this time step
40. L = np.sqrt((ytd-ytip)**2+(ztd-
    ztip)**2) # calculating length gangway for this time step
41. alpha = np.arctan((ztd-ztip)/(ytd-
    ytip)) # calculating alpha for this time step
42. theta = 0
43.
44. # creating K-matrix
45. K = np.array([[ k22, 0, 0],
46.               [ 0, k33 , 0],
47.               [ 0, 0 , k44]])
48.
49. # creating M-matrix
50. M = np.array([[ m+a22 , 0, 0],
51.               [ 0, m+a33 , 0],
52.               [ 0, 0 , m*(kxx)**2 + a44]])
53. # creating Ctel-matrix
54. C1 = np.array([[ c22 +(np.cos(alpha))**2 * ctel , np.sin(alpha)*np.cos(alpha)*ctel,
    yb*ctel*(((
    np.cos(alpha))**2)*theta+np.cos(alpha)*np.sin(alpha))+zb*ctel*(((np.cos(alpha))**2)
    -np.cos(alpha)*np.sin(alpha)*theta)],
55.               [ np.sin(alpha)*np.cos(alpha)*ctel, c33 +(np.sin(alpha))**2 * ctel
    , yb*ctel*(((np.sin(alpha))**2)-np.cos(alpha)*np.sin(alpha)*theta)+zb*ctel*(((
    np.sin(alpha))**2)*theta-np.cos(alpha)*np.sin(alpha)],
```

```

56.      [ yb*ctel*((( -
np.cos(alpha)**2)*theta+np.cos(alpha)*np.sin(alpha))+zb*ctel*(((np.cos(alpha)**2)
-np.cos(alpha)*np.sin(alpha)*theta), yb*ctel*(((np.sin(alpha)**2)-
np.cos(alpha)*np.sin(alpha)*theta)+zb*ctel*((( -np.sin(alpha)**2)*theta-
np.cos(alpha)*np.sin(alpha)), yb*yb*ctel*(((np.sin(alpha)**2)-
np.cos(alpha)*np.sin(alpha)*theta)+zb*zb*ctel*(((np.cos(alpha)**2)+np.cos(alpha)*n
p.sin(alpha)*theta) + zb*yb*ctel*(-2*np.cos(alpha)*np.sin(alpha)-
np.sin(alpha)*np.sin(alpha)*theta+np.cos(alpha)*np.cos(alpha)*theta)+c44]])
57. # creating M-matrix
58. C2 = np.array([[ np.sin(alpha)*np.sin(alpha)*(cluf/(L*L)) , -
np.sin(alpha)*np.cos(alpha)*(cluf/(L*L)), yb*(cluf/(L*L))*(-
np.sin(alpha)*np.cos(alpha)-
np.sin(alpha)*np.sin(alpha)*theta)+zb*(cluf/(L*L))*(np.sin(alpha)*np.cos(alpha)*the
ta- np.sin(alpha)*np.sin(alpha))],
59.      [ -
np.sin(alpha)*np.cos(alpha)*(cluf/(L*L)), np.cos(alpha)*np.cos(alpha)*(cluf/(L*L))
, yb*(cluf/(L*L))*(np.sin(alpha)*np.cos(alpha)*theta+np.cos(alpha)*np.cos(alpha))+
b*(cluf/(L*L))*(np.sin(alpha)*np.cos(alpha)-np.cos(alpha)*np.cos(alpha)*theta)],
60.      [ yb*(cluf/(L*L))*(-np.sin(alpha)*np.cos(alpha)-
np.sin(alpha)*np.sin(alpha)*theta)+zb*(cluf/(L*L))*(np.sin(alpha)*np.cos(alpha)*the
ta-
np.sin(alpha)*np.sin(alpha)), yb*(cluf/(L*L))*(np.sin(alpha)*np.cos(alpha)*theta+np
.cos(alpha)*np.cos(alpha))+zb*(cluf/(L*L))*(np.sin(alpha)*np.cos(alpha)-
np.cos(alpha)*np.cos(alpha)*theta) ,yb*yb*(cluf/(L*L))*(np.sin(alpha)*np.cos(alpha)
*theta+np.cos(alpha)*np.cos(alpha))+zb*zb*(cluf/(L*L))*(np.sin(alpha)*np.sin(alpha)
-np.sin(alpha)*np.cos(alpha)*theta)+yb*zb*(cluf/(L*L))*(-
np.cos(alpha)*np.cos(alpha)*theta+2*np.sin(alpha)*np.cos(alpha)+np.sin(alpha)*np.si
n(alpha)*theta) ]])
61.
62. C = C1 + C2
63.
64. # time span
65. t0 = 0 # [s] start time simulation
66. tend = 300 # [s] end time simulation
67. stepsize = 3000 # steps between start and end time
68. ft = np.linspace(t0, t0+tend, stepsize) # creating time matrix
69.
70. tspan = np.zeros([2]) # creating time span matrix
71. tspan[1] = t0+tend # end value of time span
72. tspan[0] = t0 # begin value of time span
73.
74. # force
75. Hz = 1/15 # define frequency of t
he force
76. Fy = 167000 * np.sin(Hz * 2 * np.pi * ft - (np.pi/2)) # defining the force
acting on the mass
77. Fz = 1633500 * np.sin(Hz * 2 * np.pi * ft) # defining the force acting on t
he mass
78. Mtheta = 56733 * np.sin(Hz * 2 * np.pi * ft - (np.pi/2)) # defining the for
ce acting on the mass
79.
80. # %% initial conditions
81.
82. # y-direction
83. y = 0 # start position
84. ydot = 0 # start velocity
85.
86. # z-direction
87. z = 0 # start position
88. zdot = 0 # start velocity
89.
90. # angle theta
91. theta = 0 # start position
92. thetadot = 0 # start velocity
93.
94. # creating vector containing initial conditions

```

```

95. ic = np.array([y, ydot, z, zdot, theta, thetadot])
96.
97. # %% ODE solver
98.
99. # function used in ode solver
100.     def ode_function(t, y, C, Fy, Fz, Mtheta, L, alpha):
101.         """defining conditions"""
102.
103.         # %% interpolating forces and moment
104.         Fy_int = interpolate.interp1d(ft, Fy, fill_value="extrapolate")
105.         Fz_int = interpolate.interp1d(ft, Fz, fill_value="extrapolate")
106.         Mtheta_int = interpolate.interp1d(ft, Mtheta, fill_value="extrapolate")
107.
108.         # taking the value of the force at this time step
109.         Fy = Fy_int(t)
110.         Fz = Fz_int(t)
111.         Mtheta = Mtheta_int(t)
112.
113.         # %% calculating legnth gangway and angle of gangway
114.         if t > 0:
115.             ytip = (y[0]+yb) + (np.cos(beta+y[4])-
116.                 np.cos(beta)) # calculating ytip for this time step
117.             ztip = (y[2]+zb) + (np.sin(beta+y[4])-
118.                 np.sin(beta)) # calculating ztip for this time step
119.             L = np.sqrt((ytd-ytip)**2+(ztd-
120.                 ztip)**2) # calculating length gangway for this time step
121.             alpha = np.arctan((ztd-ztip)/(ytd-
122.                 ytip)) # calculating alpha for this time step
123.
124.             # creating Ctel-matrix
125.             C1 = np.array([[ c22 +(np.cos(alpha))**2 * ctel , np.sin(alpha)*np.c
126.                 os(alpha)*ctel, yb*ctel*((( -
127.                 np.cos(alpha))**2)*theta+np.cos(alpha)*np.sin(alpha))+zb*ctel*(((np.cos(alpha))**2)
128.                 -np.cos(alpha)*np.sin(alpha)*theta)],
129.                 [ np.sin(alpha)*np.cos(alpha)*ctel, c33 +(np.sin(alph
130.                 a))**2 * ctel , yb*ctel*(((np.sin(alpha))**2)-
131.                 np.cos(alpha)*np.sin(alpha)*theta)+zb*ctel*((( -np.sin(alpha))**2)*theta-
132.                 np.cos(alpha)*np.sin(alpha))],
133.                 [ yb*ctel*((( -
134.                 np.cos(alpha))**2)*theta+np.cos(alpha)*np.sin(alpha))+zb*ctel*(((np.cos(alpha))**2)
135.                 -np.cos(alpha)*np.sin(alpha)*theta), yb*ctel*(((np.sin(alpha))**2)-
136.                 np.cos(alpha)*np.sin(alpha)*theta)+zb*ctel*((( -np.sin(alpha))**2)*theta-
137.                 np.cos(alpha)*np.sin(alpha)) , yb*yb*ctel*(((np.sin(alpha))**2)-
138.                 np.cos(alpha)*np.sin(alpha)*theta)+zb*z*ctel*(((np.cos(alpha))**2)+np.cos(alpha)*n
139.                 p.sin(alpha)*theta) + zb*yb*ctel*(-2*np.cos(alpha)*np.sin(alpha)-
140.                 np.sin(alpha)*np.sin(alpha)*theta+np.cos(alpha)*np.cos(alpha)*theta)+c44]])
141.
142.             # creating Cluf-matrix
143.             C2 = np.array([[ np.sin(alpha)*np.sin(alpha)*(cluf/(L*L)) , -
144.                 np.sin(alpha)*np.cos(alpha)*(cluf/(L*L)), yb*(cluf/(L*L))*(-
145.                 np.sin(alpha)*np.cos(alpha)-
146.                 np.sin(alpha)*np.sin(alpha)*theta)+zb*(cluf/(L*L))*(np.sin(alpha)*np.cos(alpha)*the
147.                 ta-np.sin(alpha)*np.sin(alpha))],
148.                 [ -
149.                 np.sin(alpha)*np.cos(alpha)*(cluf/(L*L)), np.cos(alpha)*np.cos(alpha)*(cluf/(L*L))
150.                 , yb*(cluf/(L*L))*(np.sin(alpha)*np.cos(alpha)*theta+np.cos(alpha)*np.cos(alpha))+z
151.                 b*(cluf/(L*L))*(np.sin(alpha)*np.cos(alpha)-np.cos(alpha)*np.cos(alpha)*theta)],
152.                 [ yb*(cluf/(L*L))*(-np.sin(alpha)*np.cos(alpha)-
153.                 np.sin(alpha)*np.sin(alpha)*theta)+zb*(cluf/(L*L))*(np.sin(alpha)*np.cos(alpha)*the
154.                 ta-
155.                 np.sin(alpha)*np.sin(alpha)), yb*(cluf/(L*L))*(np.sin(alpha)*np.cos(alpha)*theta+np
156.                 .cos(alpha)*np.cos(alpha))+zb*(cluf/(L*L))*(np.sin(alpha)*np.cos(alpha)-
157.                 np.cos(alpha)*np.cos(alpha)*theta) ,yb*yb*(cluf/(L*L))*(np.sin(alpha)*np.cos(alpha)
158.                 *theta+np.cos(alpha)*np.cos(alpha))+zb*z*ctel*(cluf/(L*L))*(np.sin(alpha)*np.sin(alpha)
159.                 -np.sin(alpha)*np.cos(alpha)*theta)+yb*z*ctel*(cluf/(L*L))*(-

```

```

np.cos(alpha)*np.cos(alpha)*theta+2*np.sin(alpha)*np.cos(alpha)+np.sin(alpha)*np.si
n(alpha)*theta) ]])
128.         # combining both matrices
129.         C = C1 + C2
130.
131.         #         C3 = np.array([[ c22, 0, 0],
132.         #                        [ 0, c33 , 0],
133.         #                        [ 0, 0 , c44]])
134.         #
135.
136.         #         print(C)
137.         #         print(alpha)
138.         #         L_vec = []
139.         #         alpha_vec = []
140.         #         L_vec.append(L)
141.         #         alpha_vec.append(alpha)
142.
143.         # %% creating system vector
144.         dy = np.zeros([6])
# creating output matrix dy
145.
146.         # defining state-vector
147.         dy[0] = y[1]
#
148.         dy[1] = (Fy - K[0,0]*y[0] - C[0,0]*y[1] - C[0,1]*y[3] - C[0,2]*y[5]) * (
1 / M[0,0]) #
149.         dy[2] = y[3]
#
150.         dy[3] = (Fz - K[1,1]*y[2] - C[1,0]*y[1] - C[1,1]*y[3] - C[1,2]*y[5]) * (
1 / M[1,1]) #
151.         dy[4] = y[5]
#
152.         dy[5] = (Mtheta - K[2,2]*y[4] - C[2,0]*y[1] - C[2,1]*y[3] - C[2,2]*y[5])
* (1 / M[2,2]) #
153.         return dy
154.
155.         # ODE solver
156.         sol_ode = solve_ivp(fun=lambda t, y: ode_function(t, y, C, Fy, Fz, Mtheta, L
, alpha), t_span=tspan, y0=ic, method='RK45', t_eval=ft, rtol=1e-07, atol=1e-07)
157.         # %% plotter
158.
159.         pl.plot_3(sol_ode.t, sol_ode.y[0], sol_ode.y[2], sol_ode.y[4], label1='y', l
abel2='z', label3='theta') # plotting the postion y, z and theta
160.         pl.plot_3(sol_ode.t, sol_ode.y[1], sol_ode.y[3], sol_ode.y[5], label1='ydot'
, label2='zdot', label3='thetadot') # plotting the velocity ydot, zdot and theta
dot

```

9.8 Workability study

Table 9-2 Numbering sea states.

Hs	Tz	lower	2	3	4	5	6	7	8	9
lower	upper	3	4	5	6	7	8	9	10	
0	0,25	1	5	12	22	34	48	*	-	
0,25	0,5	2	6	13	23	35	49	58	-	
0,5	0,75	3	7	14	24	36	50	59	-	
0,75	1	4	8	15	25	37	51	60	64	
1	1,25	-	9	16	26	38	52	61	65	
1,25	1,5	-	10	17	27	39	53	62	66	
1,5	1,75	-	11	18	28	40	54	63	67	
1,75	2	-	*	19	29	41	55	-	68	
2	2,25	-	-	20	30	42	56	-	-	
2,25	2,5	-	-	21	31	43	57	-	-	
2,5	2,75	-	-	-	32	44	-	-	-	
2,75	3	-	-	-	33	45	-	-	-	
3	3,25	-	-	-	*	46	-	-	-	
3,25	3,5	-	-	-	-	47	-	-	-	

Table 9-3 Results operability per parameter with dynamic interaction.

Sea State	Ftel	Lmax	Lmin	Vtel	Luffing angle	Luffing velocity	Fraction combined
1	1	1	1	1	1	1	1
2	1	1	1	1	1	1	1
3	1	1	1	1	1	1	1
4	1	1	1	1	1	1	1
5	1	1	1	1	1	1	1
6	1	1	1	1	1	1	1
7	1	1	1	1	1	1	1
8	1	1	1	1	1	1	1
9	1	1	1	1	1	1	1
10	1	1	1	1	1	0,97	0,97
11	1	1	1	1	1	0,83	0,83
12	1	1	1	1	1	1	1
13	1	1	1	1	1	1	1
14	1	1	1	1	1	1	1
15	1	1	1	1	1	1	1
16	1	1	1	1	1	0,41	0,41
17	1	1	1	1	1	0,02	0,02
18	1	1	1	1	1	0	0
19	1	1	1	1	1	0	0
20	1	1	1	1	1	0	0
21	1	1	1	1	1	0	0

22	1	1	1	1	1	1	1	1
23	1	1	1	1	1	1	1	1
24	1	1	1	1	1	1	1	1
25	1	1	1	1	1	0,88		0,88
26	1	1	1	1	1	0,17		0,17
27	1	1	1	1	1	0,01		0,01
28	1	1	1	1	1	0		0
29	1	1	1	1	1	0		0
30	1	1	1	1	1	0		0
31	1	1	1	1	1	0		0
32	0,83	0,8	0,88	0,72	0,88	0		0
33	0,71	0,68	0,57	0,54	0,76	0		0
34	1	1	1	1	1	1		1
35	1	1	1	1	1	1		1
36	1	1	1	1	1	1		1
37	1	1	1	1	1	0,89		0,89
38	1	1	1	1	1	0,29		0,29
39	1	1	1	1	1	0		0
40	1	1	1	1	1	0		0
41	1	1	1	1	1	0		0
42	1	1	1	1	1	0		0
43	0,96	0,96	1	0,89	0,97	0		0
44	0,58	0,57	0,7	0,54	0,68	0		0
45	0,5	0,44	0,45	0,4	0,54	0		0
46	0,52	0,38	0,19	0,23	0,85	0		0
47	0,23	0,21	0,12	0,09	0,25	0		0
48	1	1	1	1	1	1		1
49	1	1	1	1	1	1		1
50	1	1	1	1	1	1		1
51	1	1	1	1	1	0,97		0,97
52	1	1	1	1	1	0,7		0,7
53	1	1	1	1	1	0,07		0,07
54	1	1	1	1	1	0		0
55	1	1	0,97	0,93	1	0		0
56	0,87	0,87	0,88	0,8	0,9	0		0
57	0,78	0,78	0,84	0,77	0,85	0		0
58	1	1	1	1	1	1		1
59	1	1	1	1	1	1		1
60	1	1	1	1	1	1		1
61	1	1	1	1	1	0,83		0,83
62	1	1	1	1	1	0,28		0,28
63	1	1	1	1	1	0,01		0,01
64	1	1	1	1	1	1		1
65	1	1	1	1	1	0,91		0,91

66	1	1	1	1	1	0,52		0,52
67	1	1	1	1	1	0,11		0,11
68	1	1	1	1	1	0		0

Table 9-4 Results operability per parameter without dynamic interaction.

Sea state	Ftel	Lmax	Lmin	Vtel	Luffing angle	Luffing velocity		Fraction combined
1	1	1	1	1	1	1		1
2	1	1	1	1	1	1		1
3	1	1	1	1	1	1		1
4	1	1	1	1	1	1		1
5	1	1	1	1	1	1		1
6	1	1	1	1	1	1		1
7	1	1	1	1	1	1		1
8	1	1	1	1	1	1		1
9	1	1	1	1	1	1		1
10	1	1	1	1	1	0,97		0,97
11	0,78	0,75	1	0,69	1	0,32		0,32
12	1	1	1	1	1	1		1
13	1	1	1	1	1	1		1
14	1	1	1	1	1	1		1
15	1	1	1	1	1	1		1
16	1	1	1	1	1	0,35		0,35
17	1	1	1	1	1	0,02		0,02
18	1	1	1	1	1	0		0
19	0,38	0,38	1	0,34	0,87	0		0
20	0,64	0,64	1	0,59	0,77	0		0
21	0,44	0,41	0,78	0,37	0,62	0		0
22	1	1	1	1	1	1		1
23	1	1	1	1	1	1		1
24	1	1	1	1	1	1		1
25	1	1	1	1	1	0,86		0,86
26	1	1	1	1	1	0,16		0,16
27	1	1	1	1	1	0		0
28	1	1	1	0,99	1	0		0
29	0,79	0,79	1	0,71	0,97	0		0
30	0,64	0,64	1	0,58	0,79	0		0
31	1	1	1	0,92	1	0		0
32	0,18	0,17	0,67	0,13	0,29	0		0
33	0,23	0,24	1	0,2	0,32	0		0
34	1	1	1	1	1	1		1
35	1	1	1	1	1	1		1
36	1	1	1	1	1	1		1
37	1	1	1	1	1	0,86		0,86

38	1	1	1	1	1	0,27	0,27
39	1	1	1	1	1	0	0
40	1	1	1	1	1	0	0
41	0,61	0,61	1	0,53	0,76	0	0
42	0,48	0,49	1	0,42	0,62	0	0
43	0,67	0,66	0,89	0,6	0,7	0	0
44	0,24	0,25	0,68	0,2	0,36	0	0
45	0,24	0,24	0,47	0,21	0,24	0	0
46	0,25	0,26	1	0,2	0,24	0	0
47	0,02	0,02	0,45	0	0,03	0	0
48	1	1	1	1	1	1	1
49	1	1	1	1	1	1	1
50	1	1	1	1	1	1	1
51	1	1	1	1	1	0,97	0,97
52	1	1	1	1	1	0,63	0,63
53	1	1	1	1	1	0,04	0,04
54	0,84	0,85	1	0,76	1	0	0
55	0,59	0,59	1	0,5	0,79	0	0
56	0,71	0,72	1	0,68	0,79	0	0
57	0,51	0,51	1	0,44	0,62	0	0
58	1	1	1	1	1	1	1
59	1	1	1	1	1	1	1
60	1	1	1	1	1	1	1
61	1	1	1	1	1	0,73	0,73
62	1	1	1	1	1	0,24	0,24
63	0,83	0,82	1	0,71	0,97	0	0
64	1	1	1	1	1	1	1
65	1	1	1	1	1	0,91	0,91
66	1	1	1	1	1	0,42	0,42
67	0,94	0,94	1	0,93	1	0,02	0,02
68	0,62	0,62	1	0,52	0,82	0	0